A MEASUREMENT OF THE PROTON WEAK MAGNETIC FORM FACTOR (G_M^Z) AT Q^2=0.1 GeV^2/c^2

BY

TONY ANDREW FOREST

B.S., University of Southern Colorado, 1987
M.A., Western Michigan University, 1991

THESIS

Submitted in partial fulfillment of the requirements
for the degree of Doctor of Philosophy in Physics
in the Graduate College of the
University of Illinois at Urbana-Champaign, 1998

Urbana, Illinois

A MEASUREMENT OF THE PROTON
WEAK MAGNETIC FORM FACTOR (G_M^Z) AT Q^2=0.1 GeV^2/c^2

Tony Andrew Forest , Ph.D.
Department of Physics
University of Illinois at Urbana-Champaign, 1998
Douglas H. Beck, Advisor

The first measurement of the proton weak magnetic form factor G_M^Z has been made using parity-violating, elastic $^1H(\vec{e},e)$ scattering at a momentum transfer of Q^2= 0.1 GeV^2/c^2). A measured physics asymmetry of

$$A_{phys} \quad = \quad (-5.22 \pm 2.24 \pm 0.62) \times 10^{-6}$$

corresponds to a measured weak magnetic form factor of

$$G_M^Z(Q^2 = 0.1GeV^2/c^2) \quad = \quad 0.298 \pm 0.156 \pm 0.044 \pm 0.024 \;\; \mu_N.$$

The first uncertainty is statistical, the second is systematic contributions from the measurement and the third uncertainty is the contribution from the uncertainty in theoretical calculations of weak radiative corrections. The strange quark contribution to the proton magnetic form factor (G_M^s) has been determined from the weak magnetic form factor. After applying model dependent radiative corrections, the value determined is

$$G_M^s(Q^2 = 0.1GeV^2/c^2) \quad = \quad 0.49 \pm 0.62 \pm 0.17 \pm 0.10 \;\; \mu_N.$$

The measured value of G_M^s does not differentiate from zero. It is anticipated that the planned supplemental increase in the data set will decrease the uncertainty by a factor of two and improve the experimental precision of G_M^s.

Acknowledgements

Several people deserve admonishment for their efforts during the course of the work contained in this thesis. I am grateful for meeting Douglas Howard Beck, who I was able to explore my interest in the still incompletely described proton with. I was fortunate to have collaborated with other leaders in the experiment, namely Bob McKeown and Betsy Beise who I extend my thanks to. The barrage of PostDocs, Mark Pitt, Wolfgang Korsch, Fraser Duncan, and Steve Wells also deserve a special thanks for the hard work they put into the experiment. In particular I would like to extend many thanks to Neven Simicevic for making the physics he taught me entertaining as well as enlightening and Dahn Nilsson for the detector infrastructure he established and the introduction to Blues music.

I have also met a number of peers which deserve kudos. Bart Terburg and Chris Bochna should be thanked for many entertaining hours and for spending 2 years away in Virginia so the three of us could actually accomplish something. Bryon "BAMBAM" Mueller requires special credit for being the point man at BATES. Without his efforts the experiment may still be waiting for beam.

Two people remain which also deserve my thanks. First, Vijay Pandharipande, who included my wife Jun and I on a number of social outings that made a real difference in our time spent in Illinois. I must also thank my wife Jun for providing a motivating environment to finish this work.

This material is based on work supported by the National Science Foundation under Grants 89-21146, 92-57057, 93-10871, and 94-20787.

Contents

List of Tables

List of Figures

Chapter 1

Introduction

The proton is conventionally thought of as a composite particle containing three point-like constituents called quarks, more specifically, two up (u) quarks and one down (d) quark. Deep-inelastic electron-proton scattering has been one of the most direct methods used to detect the substructure within the proton. As the electron energy and the momentum transfer increases towards the deep-inelastic region, this substructure is first indicated by resonant excited states, the first of which is identified as the $\Delta(1232)$ with the remaining two composed of an admixture involving several states (see Figure 1.1). As the energy and momentum transfer increase further, continuum excitation occurs indicating a contribution due to "quasi-elastic" scattering from the quark constituents.

In addition to the three primary "valence" quark constituents, several experiments[1] have shown that the proton also contains a sea of quark and anti-quark pairs; studying these $q\bar{q}$ pairs has become the focus of current interest. Though it is often difficult to distinguish the $u\bar{u}$ and $d\bar{d}$ contribution from those of the valence quarks, the $s\bar{s}$ (pure sea) contribution can be detected. The CDHS[2] collaboration has measured the fraction of the proton momentum carried by the s and $\bar{s}$ quarks to be $(2.6 \pm 0.6)\%$. The CCFR [3] collaboration reports a measured strange quark content of the nucleon as being $(9.9 \pm 1.1)\%$ of the non-strange quark content and an appreciable probability for finding s and $\bar{s}$ at low momentum (see Figure 1.2). There have been recent disagreements between theory and experiment regarding the role of strange quarks

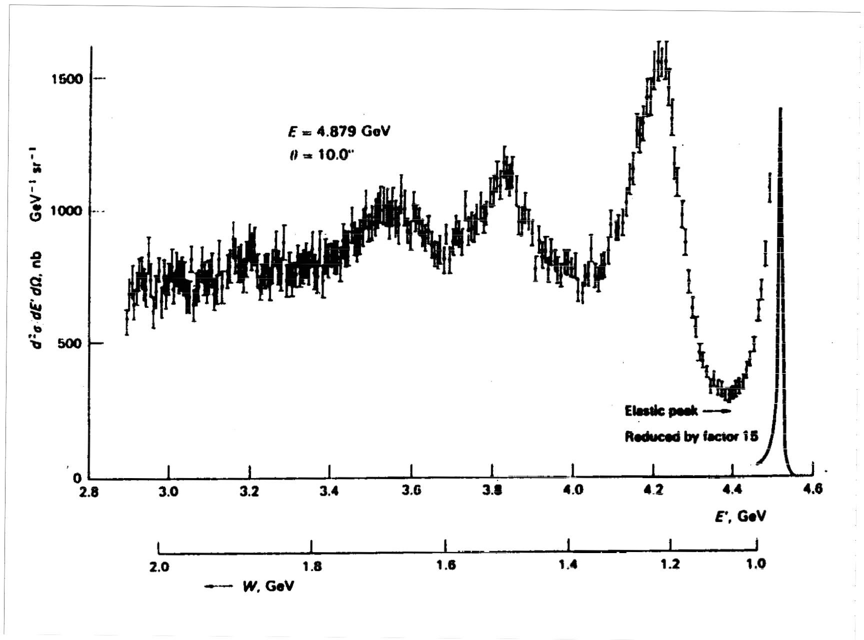

Figure 1.1: Resonances seen in electron scattering from protons using an incident electron of energy 4.879 GeV scattered at an angle of 10 degrees [6]. W represents the energy of the hadronic state after the collision.

for both the Ellis-Jaffe sum rule[4] and the πN sigma term $(\Sigma_{\pi N})$[5]. These ambiguities are among the motivations for measuring the strange quark contribution to other observable quantites of the proton.

Electron scattering has been used to establish the most fundamental properties of the nucleon (a neutron or a proton), i.e., the electric (G_E) and magnetic (G_M) form factors. These measure the charge and current densities of the nucleon as a function of momentum transfer. The form factors are Fourier transforms of the charge and magnetic moment when boosted to a frame in which the outgoing proton momentum is equal and opposite to its incident momentum[6]. These form factors are a measure of the vector quark currents in the nucleon $\langle N \mid \bar{q}\gamma_\mu q \mid N\rangle$. Related matrix elements are $\langle N|\bar{q}q|N\rangle$, determined by the πN sigma term using πN scattering, and $\langle N|\bar{q}\gamma_\mu\gamma_5 q|N\rangle$, as determined by the Ellis-Jaffe sum rule using deep-inelastic scattering. These quantities are briefly described below.

The pion-nucleon sigma term $(\Sigma_{\pi N})$ has been a source of discrepancy between

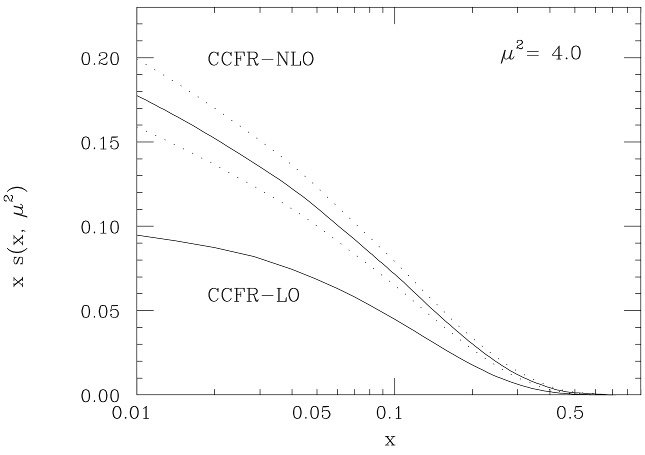

Figure 1.2: The probability distribution function of strange quarks as a function of momentum fraction [3]. The two lines represent leading-order (LO) and next-to-leading-order (NLO) QCD fits to the structure function data. The dotted lines represent $\pm$ 1 σ uncertainty in the distribution.

theory and experiment since its first measurement. When strange quarks are omitted from the calculation, theory predicts a value of $\sim$ 25 MeV[7] for $\Sigma_{\pi N}$. By extrapolating low energy πN scattering data to the corresponding unphysical point, the sigma term has been "measured" to be 64 $\pm$ 8 MeV[8].

The disagreement above may indicate the limitations of both experiment and theory. One explanation ascribes the difference to a strange quark contribution. The $\Sigma_{\pi N}$ term takes on a predicted value of 65 MeV when a strange to non-strange quark matrix element ratio ($\frac{2\langle N|\bar{s}s|N\rangle}{\langle N|\bar{u}u+\bar{d}d|N\rangle}$) within the nucleon of 0.65 $\pm$ 0.08[9] is assumed. A more direct indication of the effect strange quarks have on the low energy nucleon properties is called for.

Sum rules have been used to simplify the physical interpretations of structure functions through integration. The momentum sum rule is an example of integrating the structure function of a particle to express the physical property that the momentum fraction of its constituents must add to unity. A disagreement between theory and experiment currently exists in the case of the Ellis-Jaffe sum rule[10]. This sum rule integrates the spin dependent structure function of the nucleon. Theory predicts a value of 0.186 ± 0.02[10] for the proton sum rule while the experimental world average is reported to be $0.136 \pm 0.11 \pm 0.011$[11] where the last quoted error is from experimental systematics. This places experiment about two standard deviations below the Ellis-Jaffe sum rule. One simple explanation is that the source of disagreement between theory and experiment is due to a contribution from polarized $s\bar{s}$ quarks. However, while the experimental extraction of the sum rule would ideally involve measuring the entire momentum fraction spectrum ($0 \leq x \leq 1$), current measurements encompass the region $0.01 \leq x \leq 0.7$. The experimental result has been shown to be sensitive to the functional form chosen for the extrapolation[12].

The above experimental results created a "spin crisis" for the nucleon indicating that the u, d, and s quarks account for only (31 ± 7)% of the nucleon spin[13]. The contribution of the strange quark spin to the spin of the nucleon may be extracted using the results of the Ellis-Jaffe sum rule measurements together with information from baryon β decay. The strange sea appears to be negatively polarized with respect to the nucleon at (-10 ± 3)%[13]. While it remains to be seen if these conclusions will stand, it is again clear that further related measurements should be undertaken.

The "SAMPLE" experiment probes the structure of the proton using the weakly interacting Z boson exchanged between a polarized electron and an unpolarized proton at a momentum transfer of $Q^2 = 0.1$ (GeV/c)^2. Since both a photon and Z boson can be exchanged in this reaction, parity-violating properties of the weak interaction are used to determine the effects of the Z boson exchange. The parity-violating asymmetry is used to extract, for the first time, the strange quark contribution (G_M^s) to the proton magnetic form factor (G_M) and thereby provide information on the role of sea quarks at low energies.

Chapter 2

Theory

The formalism for treating electromagnetic interactions can be extended to a description of electroweak interactions. By constructing the relevant currents for the case of electromagnetic elastic electron scattering from the underlying interaction, a cross-section can be formulated and used to extract nucleon observables. The charge and magnetic form factors of the proton G_E^p and G_M^p are the observables which have been measured and are shown in Figure 2.2. In an analogous fashion, individual quark currents for electroweak elastic scattering can be used to describe the quark flavor contribution to the above form factors under the assumption of iso-spin symmetry (see Section 2.3). Unfortunately, weak radiative processes influence the extraction of this information and must be accounted for. Once radiative corrections are made to the weak form factor (G^Z), the contribution of strange quarks to the proton magnetic moment can be extracted.

2.1 Electromagnetic Elastic Electron Nucleon Scattering

The current of an electron interacting with an electromagnetic field in an elastic scattering process involving a nucleon, of mass M, may be written as:

$$j_\mu(x) \quad = \quad Q\overline{u}(k', s')\gamma_\mu u(k, s)e^{i(k'-k)\cdot x} \tag{2.1}$$

where Q is the electron charge and $u(k, s)$ is the Dirac spinor, in the "standard" representation, of an electron with initial (final) helicity s (s') and momentum $k(k')$.

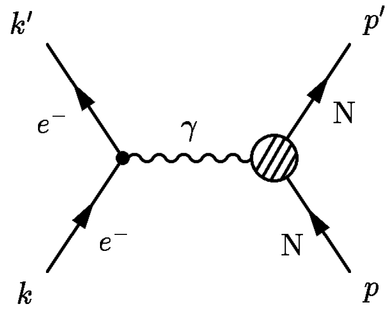

Figure 2.1: Elastic electron-nucleon scattering.

Since the nucleon is not a point particle like the electron, its current is written in terms of two independent form factors known as the Dirac form factor $F_1(q^2)$ and the Pauli form factor $F_2(q^2)$:

$$J_\mu = Q\overline{u}(p',S')[F_1(q^2)\gamma_\mu + iF_2(q^2)\sigma_{\mu\nu}(p'-p)^\nu]u(p,S)e^{i(p'-p)\cdot x} \tag{2.2}$$

Using the Gordon decomposition identity[6] this current may also be written as

$$\begin{aligned} J_\mu &= Q\overline{u}(p',S')[G_M(q^2)\gamma_\mu - F_2(p+p')_\mu]u(p,S)e^{i(p'-p)\cdot x} && (2.3) \\ &= Q\overline{u}(p',S')\left[G_M(q^2)\gamma_\mu - \frac{G_M(q^2)-G_E(q^2)}{1-\frac{q^2}{4M^2}}(p+p')_\mu\right]u(p,S)e^{i(p'-p)\cdot x} && (2.4) \end{aligned}$$

where

$$\begin{aligned} G_M(q^2) &= F_1(q^2) + F_2(q^2) && (2.5) \\ G_E(q^2) &= F_1(q^2) - \frac{q^2}{4M^2}F_2(q^2). && (2.6) \end{aligned}$$

Here q^2 is the momentum transfer squared given by $q^2 = (p'-p)^2 = (k-k')^2 \equiv -Q^2 < 0$. In the Breit frame where $\vec{p}\,' = -\vec{p}$ the Sachs form factors $G_E(q^2 = -4p^2)$ and $G_M(q^2 = -4p^2)$ are the Fourier transforms of the nucleon charge and magnetic moment distributions respectively.

The amplitude for this scattering process is written as

$$\mathcal{M}^\gamma = -i\frac{e^2}{q^2}\overline{u}(k',s')\gamma^\mu u(k,s)$$

$$\times \quad \overline{u}(p', S') \left[G_M(q^2)\gamma_\mu - \frac{G_M(q^2) - G_E(q^2)}{1 - \frac{q^2}{4M^2}}(p+p')_\mu \right] u(p, S) \qquad (2.7)$$

The Rosenbluth equation [14] is derived from the above amplitude squared and may be written as

$$\left(\frac{d\sigma}{d\Omega}\right)_{\text{lab}} = \left(\frac{d\sigma}{d\Omega}\right)_{\text{Mott}} \left[\frac{(G_E^N)^2 + \tau (G_M^N)^2}{1+\tau} + 2\tau (G_M^N)^2 \tan^2(\theta/2) \right], \qquad (2.8)$$

where τ represents $Q^2/4M^2$, Q is the four-momentum transfer and the Mott cross section is given by

$$\left(\frac{d\sigma}{d\Omega}\right)_{\text{Mott}} = \frac{\alpha^2}{4E^2 \sin^4(\theta/2)} \frac{\cos^2(\theta/2)}{1 + \frac{2E}{M}\sin^2(\theta/2)}. \qquad (2.9)$$

Here E is the incident electron energy and θ is the angle of the scattered electron. The form factors measured for the neutron and proton are shown in Figure 2.2 along with the dipole form (see Equations 2.10 - 2.12) used to fit the data.

$$G_{E,M}^p(Dipole) = \frac{G_{E,M}^p(Q^2 = 0)}{(1 + \frac{Q^2}{M_v^2})^2} \qquad (2.10)$$

$$G_M^n(Dipole) = \frac{G_M^n(Q^2 = 0)}{(1 + \frac{Q^2}{M_v^2})^2} \qquad (2.11)$$

$$G_E^n(Dipole) = \frac{Q^2}{4M_p^2(1 + \frac{Q^2}{M_v^2})^2} \qquad (2.12)$$

A fit to the neutron magnetic form factor (G_M^n) data in Figure 2.2 below Q^2 of 1.0 GeV^2/c^2 results in a value of M_v = 0.848 $\pm$ .001 GeV with a goodness of fit χ^2/ν = 0.68. This value is comparable with the standard value of 0.843 GeV [15].

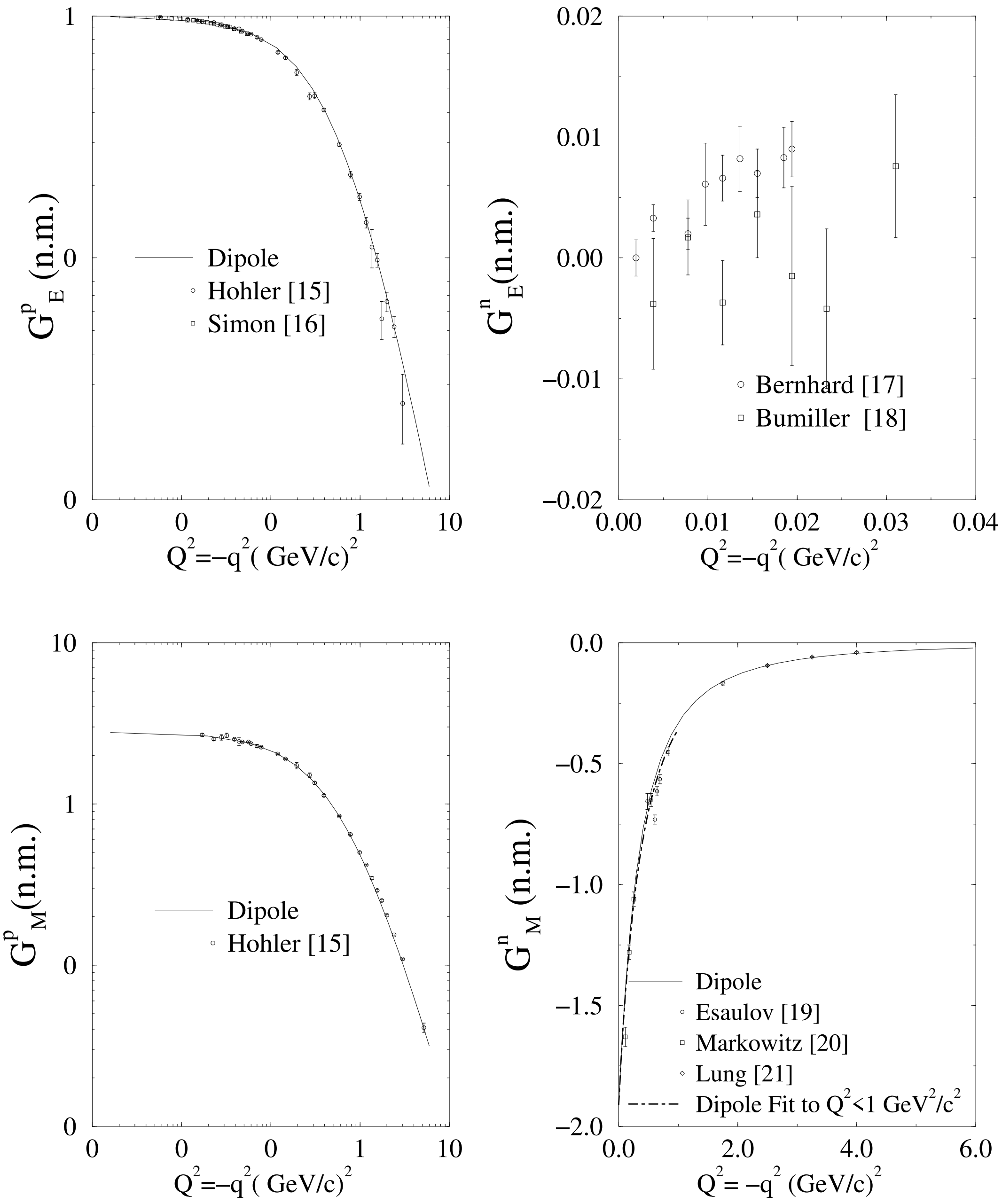

Figure 2.2: Nucleon Electric and Magnetic Form Factors. Reference [15] contains tables of data from several referenced sources.

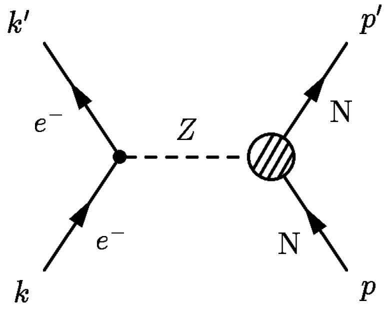

Figure 2.3: Elastic electron-nucleon scattering mediated by a Z^0 boson.

2.2 Weak Neutral Current Elastic Scattering

The "standard model" of electroweak interactions, using the nomenclature of Reference [6], describes the neutral electromagnetic current j_μ^{em} as

$$j_\mu = e j_\mu^{em} \tag{2.13}$$

$$= e(J_\mu^3 + \frac{1}{2} j_\mu^Y) \tag{2.14}$$

and relates the weak neutral current J_μ^{NC} to the weak iso-spin current $\vec{J}$ as

$$J_\mu^{NC} \equiv J_\mu^3 - \sin^2\theta_W j_\mu^{em}. \tag{2.15}$$

The weak hypercharge Y and the weak iso-spin T quantum numbers are given in Table 2.1. The Weinberg mixing angle θ_W is measured to be $\sin^2\theta_W = 0.2315 \pm .0004$ [22]. The weak hypercharge current is defined as $j_\mu^Y = \bar{u}\gamma_\mu Y u$ and the third component of the weak iso-spin current is $J_\mu^3 = \bar{u}\gamma_\mu \frac{1-\gamma^5}{2}\hat{T}^3 u = \bar{\chi}_L \gamma_\mu \hat{T}^3 \chi_L$. The spinor χ_L represents a two dimensional weak iso-doublet of Dirac spinors in the form $\begin{pmatrix} \nu_e \\ e^- \end{pmatrix}_L$ for electron currents and $\begin{pmatrix} u \\ d \end{pmatrix}_L$, $\begin{pmatrix} c \\ s \end{pmatrix}_L$, and $\begin{pmatrix} t \\ b \end{pmatrix}_L$, for quark currents where the quark abbreviation has been used to denote the Dirac spinor u for that particle.

The above currents may be grouped into electromagnetic, vector and axial-vector

Particle	T	T^3	Y	Q_i
e_L^-	1/2	-1/2	-1	-1
e_R^-	0	0	-2	-1
$(u,c,t)_L$	1/2	1/2	1/3	2/3
$(u,c,t)_R$	0	0	4/3	2/3
$(d,s,b)_L$	1/2	-1/2	1/3	-1/3
$(d,s,b)_R$	0	0	-2/3	-1/3

Table 2.1: Particle charge Q_i, weak iso-spin T and hypercharge Y quantum numbers

quark currents operators written as

$$\hat{J}^{em}_{\mu,i} \equiv Q_i \bar{u}_i \gamma_\mu u_i \tag{2.16}$$

$$\hat{J}^{NC}_{\mu,i} \equiv \bar{u}_i (\frac{T^3_i}{2} - Q_i \sin^2\theta_W) \gamma_\mu u_i \tag{2.17}$$

$$\hat{J}^{NC}_{A,i} \equiv \bar{u}_i \frac{-T^3_i}{2} \gamma_\mu \gamma^5 u_i \tag{2.18}$$

respectively for quarks of flavor i and charge Q_i. The current of the nucleon may then be written in terms of these quark current operators as;

$$J^{em}_\mu \equiv \langle N | \sum_i \hat{J}^{em}_{\mu,i} | N \rangle \tag{2.19}$$

$$J^{NC}_\mu \equiv \langle N | \sum_i \hat{J}^{NC}_{\mu,i} | N \rangle \tag{2.20}$$

$$J^{NC}_A \equiv \langle N | \sum_i \hat{J}^{NC}_{A,i} | N \rangle \tag{2.21}$$

where the sum is over all quark flavors $(i = u, d, c, s, t, b)$.

In this framework, a description of the nucleon quark current operators may be written in analogy to Equation 2.4 as [23]

$$J^{em}_{\mu,i} \equiv Q_i \overline{u}_i(p', S') \left[G^i_M(q^2)\gamma_\mu - \frac{G^i_M(q^2) - G^i_E(q^2)}{1 - \frac{q^2}{4M^2}} (p+p')_\mu \right] u_i(p,S) \tag{2.22}$$

$$\begin{aligned} J^{NC}_{\mu,i} \equiv\ & \overline{u}_i(p', S')(\frac{T^3_i}{2} - Q_i \sin^2\theta_W) \\ & \left[G^i_M(q^2)\gamma_\mu - \frac{G^i_M(q^2) - G^i_E(q^2)}{1 - \frac{q^2}{4M^2}} (p+p')_\mu \right] u_i(p,S) \end{aligned} \tag{2.23}$$

$$J^{NC}_{A,i} \equiv \bar{u}_i(p', S')\frac{-T^3_i}{2}G^i_1(q^2)\gamma_\mu\gamma^5 u_i(p,S) \tag{2.24}$$

The component of the nucleon spinor with initial momentum p and helicity S that describes quarks of flavor i is represented as $u_i(p,S)$. The form factor $G^i_1(q^2)$ is the axial-vector form factor.

2.3 Extracting quark form factors

Analogous to the representation of the nucleon current in Equation 2.19, the quark-nucleon form factors $G^i(q^2)$ may be cast in terms of the nucleon form factors in Equation 2.5 and Equation 2.6 [23].

$$G^\gamma_{E,M} \equiv G^{em}_{E,M} = \sum_i Q_i G^i_{E,M} \tag{2.25}$$

$$G^Z_{E,M} \equiv G^{NC}_{E,M} = \sum_i (\frac{T^3_i}{2} - Q_i \sin^2\theta_W) G^i_{E,M} \tag{2.26}$$

$$G^Z_A = \sum_i -\frac{T^3_i}{2} G^i_1 \tag{2.27}$$

The electric $G^\gamma_E(q^2)$ and magnetic $G^\gamma_M(q^2)$ form factors for the proton and the magnetic $G^\gamma_M(q^2)$ form factor for the neutron are well known while the neutron electric form factor is less constrained by experiment (see Figure 2.2). The form factor G^Z_M is unconstrained by experiment. By truncating the sum to the strange quark mass and assuming the distribution of $u(\bar{u})$ quarks in the proton is identical to the $d(\bar{d})$ quark distribution in the neutron (iso-spin symmetry), a system of three magnetic form factor equations may be written containing the three unknown quark-nucleon form factors G^i_M and one unknown nucleon form factor G^Z_M[23].

$$G^{\gamma,p}_M = \frac{2}{3}G^u_M - \frac{1}{3}G^d_M - \frac{1}{3}G^s_M \tag{2.28}$$

$$G^{\gamma,n}_M = -\frac{1}{3}G^u_M + \frac{2}{3}G^d_M - \frac{1}{3}G^s_M \tag{2.29}$$

$$\begin{aligned} G^{Z,p}_M = {} & (\frac{T^3_u}{2} - Q_u \sin^2\theta_W)G^u_M + (\frac{T^3_d}{2} - Q_d \sin^2\theta_W)G^d_M \\ & + (\frac{T^3_s}{2} - Q_s \sin^2\theta_W)G^s_M \end{aligned} \tag{2.30}$$

where G_M^i is the contribution of quarks and anti-quarks of flavor i to the proton from factor. The quark-nucleon form factors G_M^i can be constrained once the nucleon form factor G_M^Z is experimentally determined. The above system of equations will have a unique solution for G_M^s which is given below as

$$G_M^s = (1 - 4\sin^2\theta_W)G_M^{\gamma,p} - G_M^{\gamma,n} - 4G_M^{Z,p} \tag{2.31}$$

Electron scattering can occur, in the one-boson-exchange limit, with the exchange of either a photon or neutral Z-boson(Z^0). The scattering amplitude for the exchange of a Z^0 boson in elastic electron-proton scattering may be written (cf. Equation 2.7) as

$$\begin{aligned} \mathcal{M}^Z &= -i\frac{G_F}{2}\bar{u}(k', s')\gamma^\mu(T_e^3 - 2Q_e\sin^2\theta_W + T_e^3\gamma_5)u(k, s) \\ & \bar{u}(p', S')\left[J_\mu^{NC} + J_A^{NC}\right]u(p, S) \end{aligned} \tag{2.32}$$

The form factor G_M^Z is contained in the current J_μ^{NC} in a manner analogous to equation 2.24 where the quark-nucleon form factors $G_{E,M}^i$ are replaced with $G_{E,M}^Z$ respectively. G_F denotes the Fermi coupling constant.

Parity violation is one way to extract information about the weak electric (G_E^Z), magnetic (G_M^Z) and axial form factors (G_A^Z).[1] An asymmetry is defined as the difference in the cross-section from right and left handed incident electrons divided by the sum:

$$A_{ep} \equiv \frac{\sigma_+ - \sigma_-}{\sigma_+ + \sigma_-} \tag{2.33}$$

$$= \frac{\left|\mathcal{M}^\gamma + \mathcal{M}^Z\right|_R^2 - \left|\mathcal{M}^\gamma + \mathcal{M}^Z\right|_L^2}{\left|\mathcal{M}^\gamma + \mathcal{M}^Z\right|_R^2 + \left|\mathcal{M}^\gamma + \mathcal{M}^Z\right|_L^2} \tag{2.34}$$

$$= \frac{-G_F Q^2}{4\sqrt{2}\pi\alpha}\left[\frac{\epsilon\, G_E^{\gamma,p}G_E^{Z,p} + \tau G_M^{\gamma,p}G_M^{Z,p} - \zeta G_M^{\gamma,p}G_A^{Z,p}}{\epsilon\,(G_E^{\gamma,p})^2 + \tau(G_M^{\gamma,p})^2}\right] [25] \tag{2.35}$$

where

$$\frac{1}{\epsilon} = 1 + 2(1+\tau)\tan^2(\theta/2), \tag{2.36}$$

$$\zeta = \frac{1}{2}\left[1 - 4\sin^2(\theta_W)\right]\sqrt{(1-\epsilon^2)\tau(1+\tau)}. \tag{2.37}$$

[1]Neutrino scattering may also be used[24].

Taking $\sin^2(\theta_W) \sim 1/4$ and using the fact that at large θ (small ϵ) the magnetic terms dominate, the asymmetry may be written as

$$A_{ep} \simeq \frac{-G_F Q^2}{\sqrt{2}\pi\alpha} \frac{G_M^Z}{G_M^p}. \tag{2.38}$$

In this limit the weak magnetic form factor $G_M^{Z,p}$ may be extracted and used in Equation 2.29 to complete the system of equations therein and extract contributions of each quark-antiquark distribution to the three nucleon form factors. Using a mean scattering angle of 148° and a mean Q^2=0.10 (GeV/c)^2, the asymmetry in Equation 2.35 may be written, without the above approximations, as:

$$A_{ep} = -14.34 \times 10^{-6} G_M^{Z,p} \left[1 + 0.477\frac{G_E^{Z,p}}{G_M^{Z,p}} - 0.222\frac{G_A^{Z,p}}{G_M^{Z,p}}\right]. \tag{2.39}$$

Equation 23 in Reference [26] evaluates the electric and magnetic terms at q^2=0 as

$$\frac{G_E^{Z,p}}{G_M^{Z,p}} = \frac{1 - 4\sin^2\theta_W}{(1 - 4\sin^2\theta_W)\mu_p - \mu_n} \tag{2.40}$$

$$\frac{G_A^{Z,p}}{G_M^{Z,p}} = \frac{g_A}{\frac{\sqrt{4\pi\alpha}}{\sin\theta_W \cos\theta_W} \times [(1 - 4\sin^2\theta_W)\mu_p - \mu_n]} \tag{2.41}$$

inserting these expressions into equation 2.39 gives

$$A_{ep} = -14.34 \times 10^{-6} G_M^{Z,p} [1 + .196 - .183] \tag{2.42}$$

Weak radiative processes need to be accounted for in order to extract information on the form factor G_M^Z.

2.4 Weak Radiative Corrections

Weak radiative corrections [27, 28] are applied to the weak form factors in equation 2.39. At these low energy scales ($|Q^2| < 1$ GeV^2/c^2), strong interaction effects are not sufficiently small to allow perturbative treatments. Additionally, the small factor $(1 - 4\sin^2\theta_W)$ appearing in the tree-level amplitudes (Equations 2.29, 2.40 and

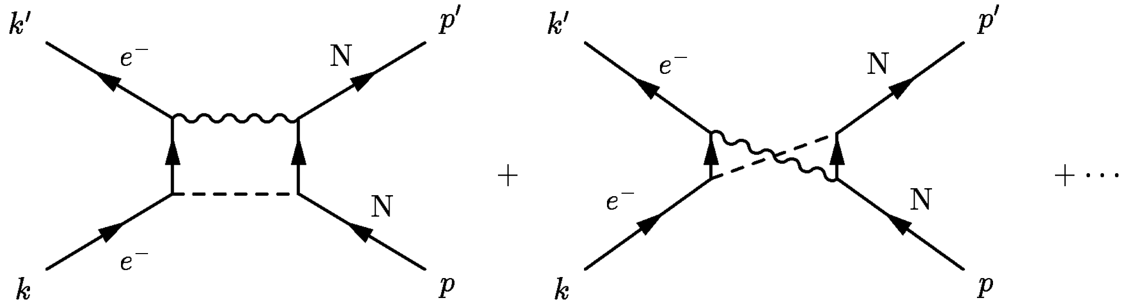

Figure 2.4: Dispersive class "A" radiative correction

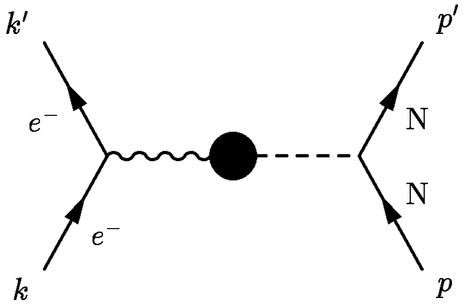

Figure 2.5: A class "A" radiative correction from a photon fluctuating to a Z-boson

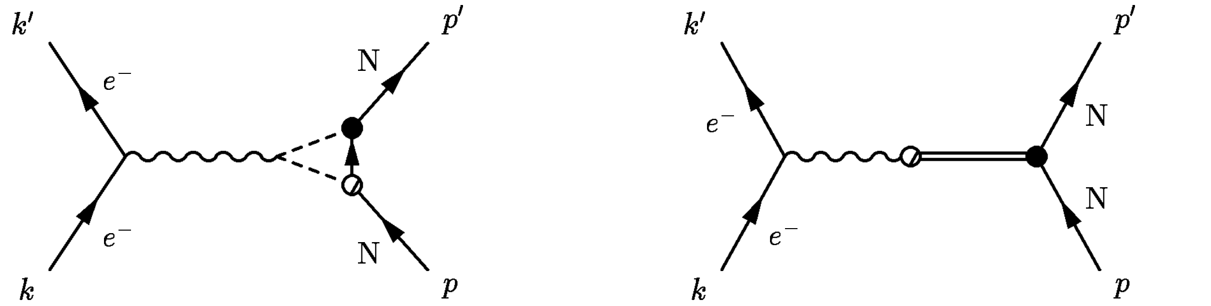

Figure 2.6: Axial "meson cloud" class B radiative corrections. Solid circles at the vertex represents a parity-violating meson-nucleon coupling. Open circles represent parity conserving meson-nucleon couplings.

2.41) may not be carried by the contributions from higher order processes. The calculation of these radiative corrections is model dependent and introduces an intrinsic theoretical uncertainty.

Contributions from four different leading second order corrections are discussed in Reference [27] and grouped into two classifications (A & B). A class "A" correction refers to "one-quark" interactions between a vector boson and the nucleon. A "dispersive" class "A" correction represents multiple boson exchange involving elementary fermions as depicted in Figure 2.4. The other "one-quark" interaction treats an exchanged boson of one type fluctuating to a boson of a different type before interacting (see Figure 2.5). Class "B" corrections are the result of weak interactions with bound hadronic quarks. Axial "meson cloud" corrections, shown in Figure 2.6, are a particular sub-class of "many-quark" contributions which have been estimated in Reference [27].

The results of the above correction calculations are applied in Reference [29] by recasting the weak current operator in equation 2.20 in terms of the electro-magnetic current operator of equation 2.19

$$\hat{J}^{NC}_{\mu} \equiv \sum_i \hat{J}^{NC}_{\mu,i} \equiv \xi_V^{T=1} \hat{J}^{em}_{\mu}(T=1) + \sqrt{3}\xi_V^{T=0} \hat{J}^{em}_{\mu}(T=0) + \xi_V^{(0)} \hat{V}^s_{\mu}. \quad (2.43)$$

where

$$\begin{aligned} \hat{J}^{em}_{\mu}(T=1) &\equiv \frac{1}{2}(\bar{u}\gamma_\mu u - \bar{d}\gamma_\mu d) & (2.44) \\ \hat{J}^{em}_{\mu}(T=0) &\equiv \frac{1}{6}(\bar{u}\gamma_\mu u + \bar{d}\gamma_\mu d \bar{s}\gamma_\mu s) & (2.45) \\ \hat{V}^s_{\mu} &\equiv \bar{s}\gamma_\mu s & (2.46) \end{aligned}$$

The weak axial current in equation 2.21 is written using the Gell-Mann matrices (λ^i) as

$$\hat{J}^{NC}_{A} \equiv \sum_i \hat{J}^{NC}_{A,i} \equiv \xi_A^{T=1} \bar{q}\lambda^3\gamma_\mu\gamma^5 q + \xi_A^{T=0} \bar{q}\lambda^8\gamma_\mu\gamma^5 q + \xi_A^{(0)} \bar{s}\lambda^3\gamma_\mu\gamma^5 s \quad (2.47)$$

The correction parameters denoted by the variable ξ are given in Table 2.2. Table 2.3 lists the theoretical calculations of the radiative correction terms R appearing in

Table 2.2 as well as the ratios R_V^p and R_V^n to be used in Equation 2.50 where

$$R_V^p \equiv \frac{1}{1-4\sin^2\theta_W}[(1-2\sin^2\theta_W)R_V^{(T=1)} - 2\sin^2\theta_W R_V^{(T=0)}] \tag{2.48}$$

$$R_V^n \equiv (1-2\sin^2\theta_W)R_V^{(T=1)} + 2\sin^2\theta_W R_V^{(T=0)}. \tag{2.49}$$

Coupling	definition	tree	HOP
$\xi_V^{T=1}$	$g_V^u - g_V^d$	$2(1-2\sin^2\theta_W)$	$2(1-2\sin^2\theta_W)[1+R_V^{T=1}]$
$\xi_V^{T=0}$	$\sqrt{3}(g_V^u + g_V^d)$	$-4\sqrt{3}\sin^2\theta_W$	$-4\sqrt{3}\sin^2\theta_W)[1+R_V^{T=0}]$
$\xi_V^{(0)}$	$g_V^u + g_V^d + g_V^s$	-1	$-[1+R_V^{(0)}]$
$\xi_A^{T=1}$	$g_A^u - g_A^d$	-2	$-2[1+R_A^{T=1}]$
$\xi_A^{T=0}$	$\sqrt{3}(g_A^u + g_A^d)$	0	$\sqrt{3}R_A^{T=0}$
$\xi_A^{(0)}$	$g_A^u + g_A^d + g_A^s$	1	$[1+R_A^{(0)}]$

Table 2.2: Vector and axial-vector SU(3) couplings in the standard model. The symbol g represents individual quark coupling coefficients. The coupling ξ are evaluated in the last two columns first at tree level and then using higher order processes (HOP) like those in Figures 2.4 - 2.6. The radiative correction term is denoted as R in each coupling and represents the ratio of the parity non-conserving amplitude generating electro-weak corrections to the tree level amplitude $\frac{A^{rad}}{A^{tree}}$. The values of these radiative correction terms appear in Table 2.3.

Correction	Scheme	one-quark	multi-quark	total
R_V^p	MS	-0.054 ± 0.033		-0.054 ± 0.033
R_V^n	MS	-0.0143 ± 0.0004		-0.0143 ± 0.0004
$R_V^{T=1}$	MS	-0.017 ± 0.002		-0.017 ± 0.002
$R_V^{T=0}$	MS	-0.0113		-0.0113 ± .0113
$R_V^{(0)}$				$10^{-4} \pm 10^{-4}$
$R_A^{T=1}$	OSR	-0.47	0.13 ± 0.20	-0.34 ± 0.20
$R_A^{T=0}$	OSR	-0.25	-0.11 ± 0.13	-0.36 ± 0.13
$R_A^{(0)}$				$10^{-2} \pm 10^{-2}$

Table 2.3: Radiative correction coefficients [28].

2.5 Extracting the strange quark contribution

The contribution of strange quarks to the proton magnetic form factor G_M^s is calculated from the measured asymmetry by recasting the weak magnetic form factors in terms of electro-magnetic form factors and the respective radiative correction. Using the currents in 2.24 the corrected neutral weak magnetic form factor for the proton becomes

$$\begin{aligned} 4G_M^{Z,p}(q^2) &= (1-4\sin^2\theta_W)[1+R_V^p]G_M^{\gamma,p}(q^2) \\ &\quad -[1+R_V^n]G_M^{\gamma,n}(q^2)-[1+R_V^{(0)}]G_M^s(q^2)[29] \end{aligned} \tag{2.50}$$

The neutral weak electric form factor $G_E^{Z,p}$ is identical to the above equation with the exception that electric form factors G_E are substituted for G_M. The weak axial form factor, within the same framework is

$$G_A^{Z,p}(q^2) = -\frac{1}{2}[1+R_A^{T=1}]G_A(q^2)+\frac{\sqrt{3}}{2}R_A^{T=0}G_A^{(8)}(q^2)+\frac{1}{2}G_A^s(q^2) \tag{2.51}$$

Substituting these expressions into equation 2.39 yields

$$A_{ep} = -14.34\times 10^{-6}\left[G_M^{Z,p}+0.477G_E^{Z,p}-0.22G_A^{Z,p}\right] \tag{2.52}$$

$$\begin{aligned} &= -3.585\times 10^{-6} \\ &\quad \Big[[(1-4\sin^2\theta_W)[1+R_V^p]G_M^{\gamma,p}(q^2)-[1+R_V^n]G_M^{\gamma,n}(q^2)-[1+R_V^{(0)}]G_M^s(q^2) \\ &\quad +0.477((1-4\sin^2\theta_W)[1+R_V^p]G_E^{\gamma,p}(q^2)-[1+R_V^n]G_E^{\gamma,n}(q^2)-[1+R_V^{(0)}]G_E^s(q^2))] \\ &\quad -0.444\left(-[1+R_A^{T=1}]G_A(q^2)+\sqrt{3}R_A^{T=0}G_A^{(8)}(q^2)+G_A^s(q^2)\right)\Big] \end{aligned} \tag{2.53}$$

The form factor values in Table 2.4, the radiative correction coefficients in Table 2.3, and the weak angle value $\sin^2(\theta_W)$ of 0.2315 ± 0.0004 are used in equation 2.53 resulting in

$$A_{ep} = [(-6.99\pm 0.23)+3.59G_M^s]\times 10^{-6} \tag{2.54}$$

The uncertainty in the constant ($\pm$ 0.23) is dominated by the uncertainty in the magnetic form factor of the neutron. Using the dipole fit and the uncertainty in the magnetic form factor of the neutron shown in Table 2.4, the uncertainty in the leading constant would be $\pm$ 0.11.

Form Factor	Q^2=0.1 GeV^2/c^2
$G_E^{\gamma,p}$	0.767 $\pm$ 0.015[15]
$G_M^{\gamma,p}$	2.142 $\pm$ 0.043 μ_N[15]
$G_E^{\gamma,n}$	0.04 $\pm$ 0.02[15]
$G_M^{\gamma,n}$	-1.472 $\pm$ 0.029 μ_N[15]
G_E^s	0$\pm$ 0.05[4]
G_A^s	-0.18 $\pm$ 0.04[30]
G_A	1.052 $\pm$0.002 [31]
$G_A^{(8)}$	0.169 $\pm$ .006[29]

Table 2.4: A table of the values used for the form factors in equation 2.53. An average scattering angle of 148.15 degrees and a Q^2 of 0.1007 (GeV/c)^2 (assuming the mean beam energy from only ionization loses was 194 MeV) were used. The electric and magnetic proton form factor have been evolved from their $Q^2 = 0$ value to the value of 0.1007 (GeV/c)^2 using the Equation 2.10 and Equation 2.11 where $M_v = 0.843$ GeV. The neutron magnetic form factor is evolved using a dipole fit to the measurements in Figure 2.2 which yielded $M_v = 0.848$ GeV. The Axial form factors have been evolved from their $Q^2 = 0$ values of $G_A(Q^2 = 0)$=1.2601 $\pm$ 0.002 and $G_A^{(8)}(Q^2 = 0)$=0.202 by the dipole formula $(\frac{1}{1+\frac{|Q^2|}{M_A^2}})^2$ where $M_A = 1.032 \pm 0.036$ GeV [32].

Chapter 3

Experimental Apparatus

The SAMPLE experiment was performed at the MIT-Bates Linear Accelerator Center. Photoemission from a GaAs based cathode provides a source of electrons polarized to 35% or higher. The incident polarized light is generated in 15μs pulses at 600 Hz and in phase with the 60 Hz Power line. The resulting electron pulses are injected into a linac and accelerated to 200 MeV. An average beam current of 40 μA (4mA peak) is incident on a 40 cm long liquid hydrogen target located in the North Experimental Hall. A system of 10 Čerenkov counters covering a solid angle of $\sim$1.5 (sr) is used to detect the electrons scattered at backward angles from the liquid hydrogen target. The position, angle, energy, and current of the incident electron beam are monitored during the experiment. The beam polarization is determined using a Møller polarimeter.

3.1 The Polarized Electron Source and Accelerator

A block diagram of the source, spin transport from the source , the accelerator, and the beam switch yard, is shown in Figure 3.1. Electrons are photo-emitted from a GaAs crystal in a SLAC-PEGGYII style diode gun [33] using a Ti:Sapphire laser that is optically pumped by a continuous wave (cw) argon laser. A 60 keV SLAC-style Wien filter, located between the electron gun and acceleration column, is used to rotate the electron spin correcting for the g-2 spin precession the electron will experience when traversing bending magnets to the experimental area. The linac, a series of RF cavities operating at 2.856 GHz, accelerates the electrons to 200 MeV before entering an energy compression system. The polarization of the electrons is measured by a Møller polarimeter positioned after the last steering magnet used to transport electrons to the liquid hydrogen target.

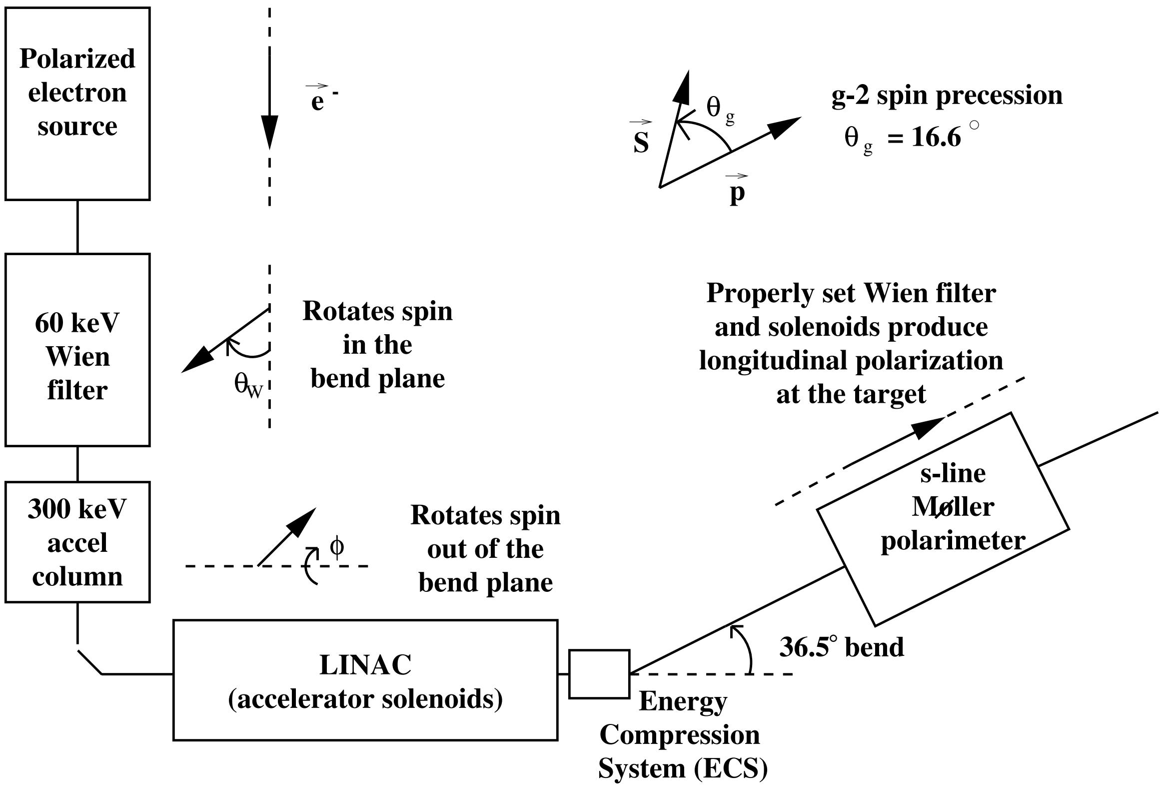

Figure 3.1: Spin rotation to the North Hall experiment area.

The optical elements used to generate polarized light are shown in Figure 3.2. The continuous wave (cw) argon laser, used to pump the Ti:Sapphire laser, has maximum output power of 30 W. A mechanical shutter is used to chop the beam with the accelerator pulse structure in order to reduce the average power of the Ti:Sapphire laser. This prevents thermal lensing problems that cause the Ti:Sappire laser output to be unstable when the pump power exceeds 16 W. The chopped pulse from the argon laser optimizes the Ti::Sapphire output to 9 Watts. A Conoptics LassII [34] feedback system reduces the Ti::Sapphire output power fluctuations from 3-6% to 0.5-1%. A shutter Pockel's cell further chops the Ti:Sapphire 700-900 nm infra-red output to a $30\mu s$ pulse. A remotely controlled half wave plate is used by accelerator operators to maintain the electron current as the GaAs quantum efficiency slowly decreases. A different half wave plate ("slow helicity reversal") is used by experimenters to check for systematic effects (see Section 5.1) by changing the electron helicity definition in a mechanical fashion over the course of the experiment. The laser helicity is controlled by a Pockel's cell whose fast and slow axes can be rotated through 90^o by changing the voltage on the cell from +2500 volts to -2500 volts using a fast solid state switch. This cell thereby produces right or left circularly polarized light which can be switched at the 600 Hz repetition rate of the accelerator.

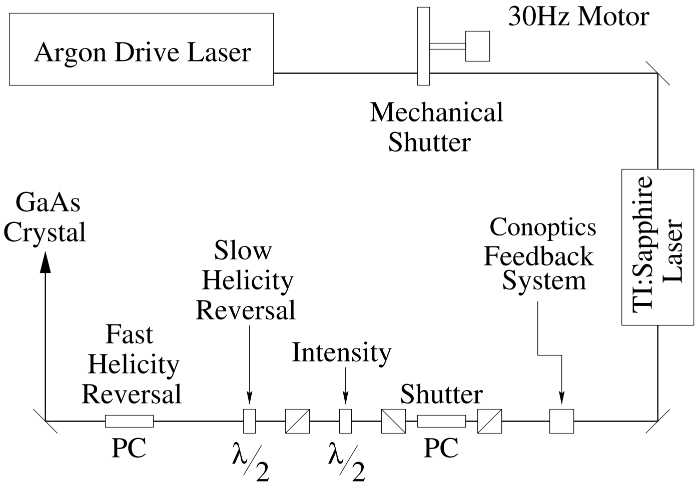

Figure 3.2: Polarized Source Laser Optics layout

Polarized electrons are created from the GaAs crystal in three basic steps. First, the electrons are optically pumped to the conduction band and have a spin determined by the magnetic substate in the transition induced by the incident circularly polarized light from the Ti::Sapphire laser. The resulting polarized conduction electrons diffuse to the crystal surface and as a result suffer some depolarization. Some of the electrons then escape into the vacuum on the final step. The escape of electrons depends strongly on the surface of the crystal which has a thin layer of Cesium to reduce the crystal work function. The theoretical maximum electron polarization for the first stage of the process is 50% due to the different transition strengths (3:1) between the magnetic substates of the valence and conduction band. The depolarization effects in step two make it difficult to obtain polarizations of 50%.

Electrons leaving the GaAs crystal are accelerated to 60 keV in the electron gun. The electrons then pass through a Wien filter to correct for the g-2 spin precession of 16.6° the electrons experience when traversing the series of bending magnets enroute to the LH_2 target. The Wien filter, located between the 60 keV and 300 keV acceleration sections, consists of electrostatic plates and a magnetic dipole producing crossed electric and magnetic fields perpendicular to the electron velocity. The Wien filter is designed to rotate the spin of the electron using the magnetic dipole yet maintain the electron trajectory. The electrostatic plates generate an electric field of sufficient field strength to zero the net Lorentz force on the electron. In this case, the spin vector will precess about the magnetic field according to

$$\frac{d\mathbf{s}}{dt} = \frac{e}{mc}\mathbf{s} \times \mathbf{B}\left[\frac{\mathbf{g}}{\mathbf{2}}(\mathbf{1}+\beta^2) - \mathbf{2}(\mathbf{1}-\frac{\mathbf{1}}{\gamma})\right] \text{[35]} \tag{3.1}$$

and, under the assumption of a perfect Wien filter of length L, the electrons spin will be rotated by

$$\theta = \frac{L}{c\beta}\frac{eB}{mc}\left[\frac{g}{2}(1+\beta^2) - 2\right] = \frac{E(V/cm)L}{5.1 \times 10^5 \beta^2}\left[\frac{g}{2}(1+\beta^2) - 2\right] \text{[33]}. \tag{3.2}$$

The Wien filter is calibrated using the Møller polarimeter (see Section 3.2).

A linac and an energy compression system are the final elements used to deliver polarized electrons to the experimental hall. The linac is composed of a series of RF cavities driven at 2.856 GHz. For the SAMPLE experiment, the electrons are accelerated to 200 MeV. The accelerated electrons leave the linac and pass through an energy compression system (ECS) which compresses the energy spread of each pulse to about .03% from the nominal 0.3%.

3.2 The Møller Polarimeter

A Møller polarimeter[36] is used to measure the incident electron polarization upstream of the LH_2 target. A schematic of the apparatus is shown in Figure 3.3. The spin dependent cross section for Møller scattering is known exactly from quantum electrodynamics. The asymmetry, for longitudinally polarized incident and target electrons ("zz") , is:

$$A_{zz} = \frac{-\sin^2(\theta_{CM})\,[7+\cos^2(\theta_{CM})]}{[3+\cos^2(\theta_{CM})]^2}[37], \tag{3.3}$$

where θ_{CM} is the center of mass scattering angle. Experimentally, the above asymmetry is diluted by the fractional polarization of the target and incident electrons. The amount of dilution is used to determine the incident electron polarization (P_b) by measuring the asymmetry (A_{meas}), and the polarization of the Møller target (P_t).

$$P_b = \frac{A_{meas}(1+B/S)}{A_{zz}P_t\cos(\theta_t)}. \tag{3.4}$$

In practice measurements are taken at the maximum asymmetry value of $A_{zz} \sim -7/9$ corresponding to a center of mass angle of 90^o. The measured asymmetry is corrected by a signal to background ratio (S/B) of 5 to 1. The target inside the polarimeter is a 13 μm foil made from Supermendur (49% Fe, 49% Co, and 2% V by weight [38]) which saturates in applied magnetic fields of $\sim$ 50 Gauss and was capable of absorbing up to .8 mA average current without any indication of beam heating effects on the measured polarization. A pair of Helmholtz coils around this target saturate the foil and produce target polarizations (P_t) of (8.0 ± 0.1)%[36] (a pickup coil measured the target magnetization M which is used to determine the target polarization using $P_t = \frac{M(1-\frac{1}{g})}{n\mu_B(1-\frac{1}{g_e})}$ where μ_B is the Bohr magneton, n the electron number density, and g is the ratio of M to the angular momentum). Due to significant spin-dependent scattering of the incident electrons by the target foils, it is necessary to suspend data collection for the SAMPLE experiment in order to measure the incident electron polarization. The high cross section of Møller scattering, fortunately, permits a polarization measurement to the 5% level in 15 minutes. The extent of a transverse component to the electron polarization, a small effect on the experiment (see Section 5.4), can also be measured.

Figure 3.4 shows measurements of the incident electron polarization at several stages of the GaAs crystal quantum efficiency. Whereas the polarization changes

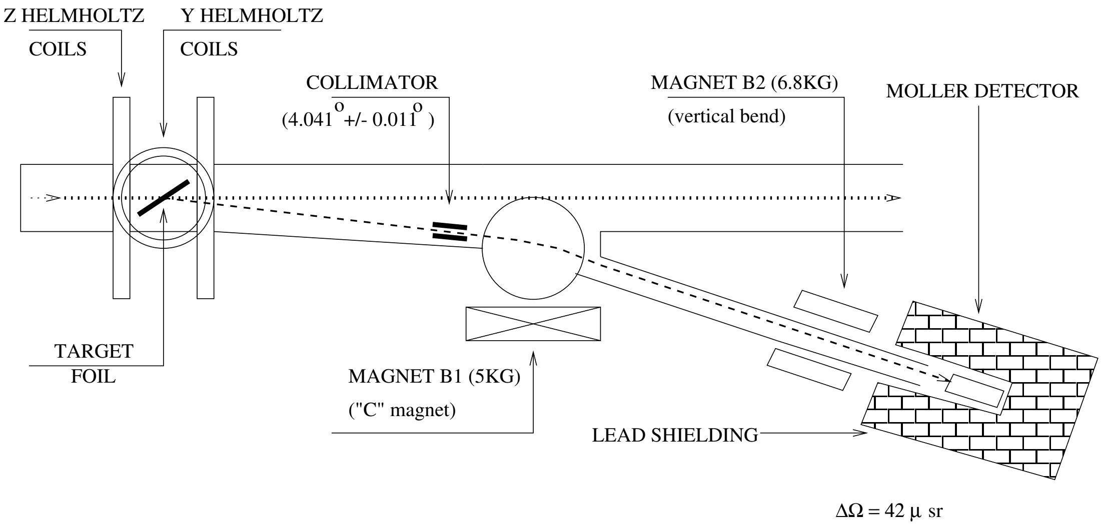

Figure 3.3: The Møller apparatus

relatively rapidly with crystal quantum efficiency, the SAMPLE experiment takes most of its data at the 1% quantum efficiency level. The crystal lifetime at this quantum efficiency is sufficiently long that polarization measurements are done about once per day in order to monitor for any changes in the electron polarization. Analysis of the Møller data is shown in section 6.4.1.

3.2.1 Optimizing Longitudinal Polarization

To insure that the electrons are longitudinally polarized when they reach the target, a Wien filter at the polarized source is used to correct for the $g-2$ spin precession experienced by the electrons as they traverse the bending magnets transporting the electrons to the experimental hall (see Figure 3.1). The Møller apparatus can polarize the target electrons either parallel or perpendicular to the incident electron momentum. Since the target magnetization is constrained to lie in the plane of the Supermendur foil, the longitudinal target polarization is accomplished by saturating the target with the target plane aligned parallel to the incident electron momentum and the longitudinal holding field generated by the Z-Helmholtz coils (see Figure 3.3) before rotating the target foil to the desired angle. Longitudinal incident electron polarization is optimized using a calibrated Wien filter and the accelerator solenoids.

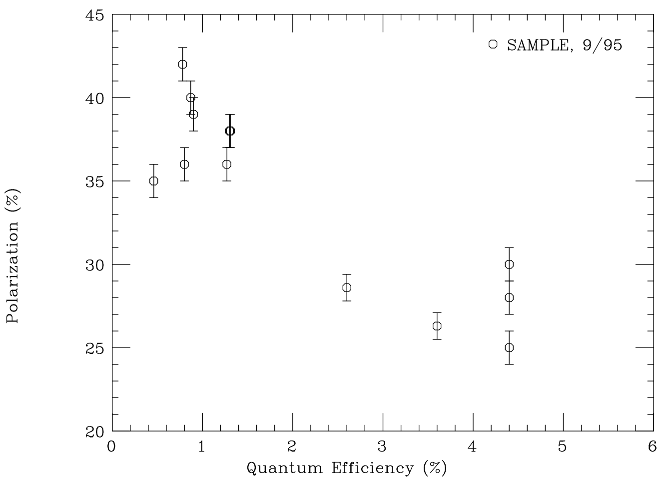

Figure 3.4: Electron polarization observed for different GaAs crystal quantum efficiencies. Data is taken around the 1% Q.E. level. The long lifetime of the source and limited polarization fluctuations at this quantum efficiency level allow limiting polarization measurements to once per day.

The Møller analyzing power for target electrons polarized in the plane of the target foil may be written as [39]:

$$\begin{aligned} A_{zz} &= \tfrac{-P_b P_t}{9(1+B/S)} \quad [(7\cos(\theta_t)\sin(\theta_g) - \sin(\theta_t)\cos(\theta_g))\sin(\theta_W)\cos(\phi) - \\ &\qquad (7\cos(\theta_t)\cos(\theta_g) - \sin(\theta_t)\sin(\theta_g))\cos(\theta_W)]. \end{aligned} \tag{3.5}$$

The angle made by the target with respect to the incident electron helicity is denoted as θ_t. The g-2 spin precession angle is denoted as $\theta_g = 16.6^o$ and the Wien precession angle by θ_W. The out of plane spin precession angle (ϕ) term can be ignored for the case where $\tan(\theta_t) = 7\tan(\theta_g)$. The objective is to adjust the target angle (θ_t) and the Wien precession angle (θ_W) such that one of the two terms in equation 3.5 is maximally sensitive to either the Wien angle or the out of plane spin precession angle ϕ.

The longitudinal polarization is established in two steps. First, the Wien filter voltage is calibrated. This is accomplished by first setting the target angle such that $\tan(\theta_t) = 7\tan(\theta_g)$. The Møller asymmetry is measured as a function of the

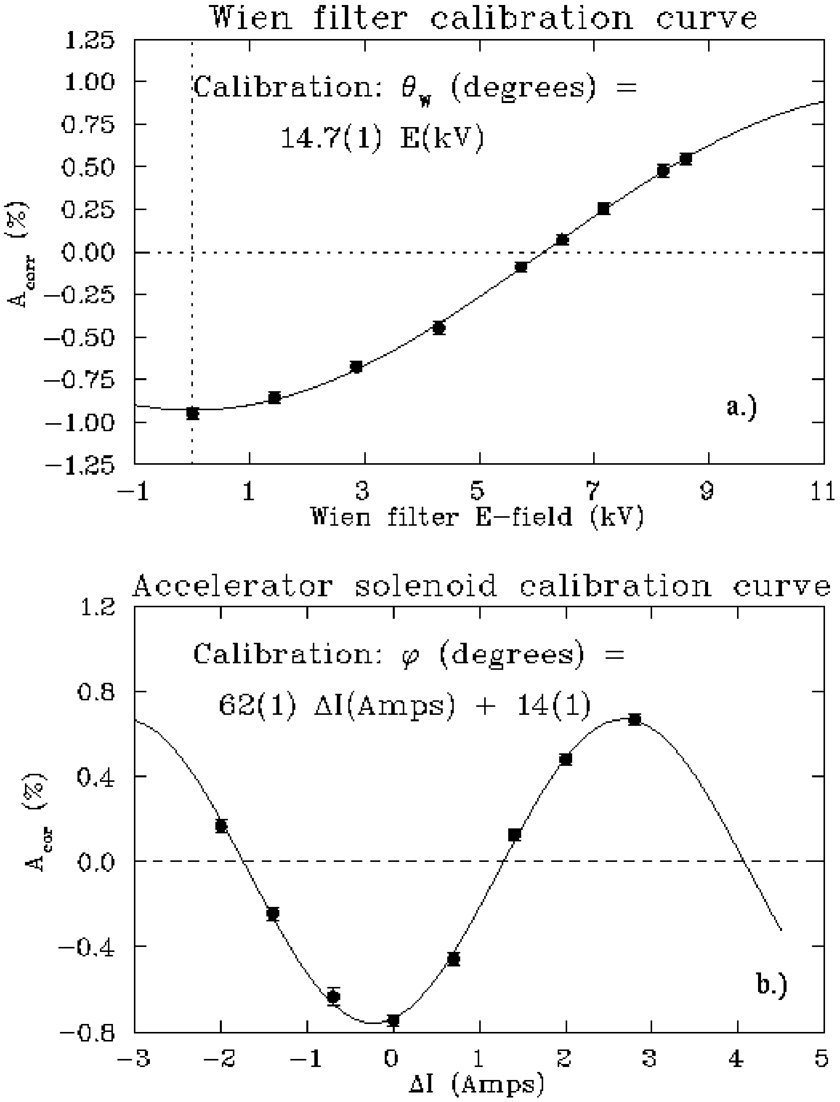

Figure 3.5: a.)Wien filter calibration with the Møller target polarized using longitudinal coils. b.)Polarization sensitivity to accelerator steering solenoids which manipulate the out of plane spin precession angle ϕ.

Wien filter voltage (θ_W). A calibration of the Wien filter voltage as a function of the Levchuck corrected[40] Møller asymmetry (A_{Cor}) is shown in Figure 3.5a. Second, the ϕ angle is zeroed to align the polarization in the accelerator to the switch yard bend plane. This is accomplished by setting the now calibrated Wien filter to $\theta_W = 90^o$

minimizing the second term in the above equation. The first term is maximized by setting the target angle θ_t to -25.6^o. The asymmetry as a function of the solenoid current difference from the nominal settings is measured (see Figure 3.5b) and the solenoid current is changed to minimize the asymmetry. The spin precession angles are set within $\pm 5^o$ for the out of plane angle (ϕ) and $\pm 1^o$ for the Wien angle (θ_W) using the above calibrations. The contribution of the ϕ error is diluted by the prefactor in Equation 3.5. As a result, the angular precision above will constrain the spin to within 2^o of longitudinal at the LH_2 target.

3.3 Incident Electron Monitors

The adjustable electron beam characteristics were established with the aid of a number of monitoring devices. In addition to the standard BeO targets (which scintillate and provide a direct picture of the incident electrons), several wire scanners were placed at strategic locations along the path to the experimental hall to monitor the beam location and profile. Wire scanners are devices which step a thin aluminum wire through the beam path. A current is generated in the wires from the secondary electron emission caused by the incident electrons. Horizontal and vertical profiles of the incident electrons are measured along the path of the beam to develop a spot size at the target which is large enough to prevent LH_2 boiling (>9 mm^2:σ_x & $\sigma_y >$ 3mm) and small enough to minimize background in the SAMPLE detector.

Several devices monitor the properties of the incident electrons and are recorded on a event by event basis in the data stream. During the experiment there were at most eight position monitors (APM24X, APM24Y, MOLX, MOLY, NH1X, NH1Y, NH2X, NH2Y), two energy sensitive monitors (DEX,ECSX), four position and energy sensitive monitors (FPM1X, FPM1Y, FPM2X, FPM2Y), seven current monitors (AT5, MT1, PTOR1, ST5, STS6, TTG1, TTG2), and four halo monitors (HALO, SHALO, MOLDET, TUBE11). The incident electron position monitors are calibrated using Helmholtz coils to deflect the incident electrons. The energy monitors are calibrated using the known "beam loading" (reduction of acceleration due to increased power absorption by the higher beam current) of the accelerator. The current monitors are calibrated using a known variable current source.

Coil Name		Distance (m)	to BPM		deflection (mrad/amp)
	NH1X	NH1Y	NH2X	NH2Y	
SSS1X (H)	6.6	6.7	10.6	10.7	0.90
SSS1Y (V)	7.8	8.0	11.8	11.9	0.85
SSS2X (H)	2.76	2.85	6.7	6.8	0.70
SSS2Y (V)	3.32	3.42	7.3	7.4	0.70

Table 3.1: The distance from each steering coil to each beam position monitor(BPM) were measured to 2%. The angular deflection a 200 MeV electron will experience when traversing each steering coil in the North Hall experimental area is shown in the last column.

SLAC style beam position monitors (BPMs)[41] are used to monitor the position of the incident electrons. The monitors measure the amplitude of the radio frequency signal induced in the cavity by the incident electrons. The signal is mixed with the accelerator drive frequency (2.856 GHz) and the resulting signal is optimized by adjusting the phase of the drive. The cavity signal is proportional to the incident electron pulse charge and position from the center of the cavity. The incident electron angle is measured using the position difference from a pair of monitors that are a known distance apart (see Table 3.1). Four steering coils (SSS1H, SSS1V, SSS2H, SSS2V), located upstream of the position monitors, can be used to deflect the incident electrons by a known amount for a given coil current (see Table 3.1). The BPMs are calibrated by stepping through a limited coil current range (see Figure 3.6). The output signal polarity depends on the relative phase between the incident electrons and the drive radio frequency and was monitored using the steering coils.

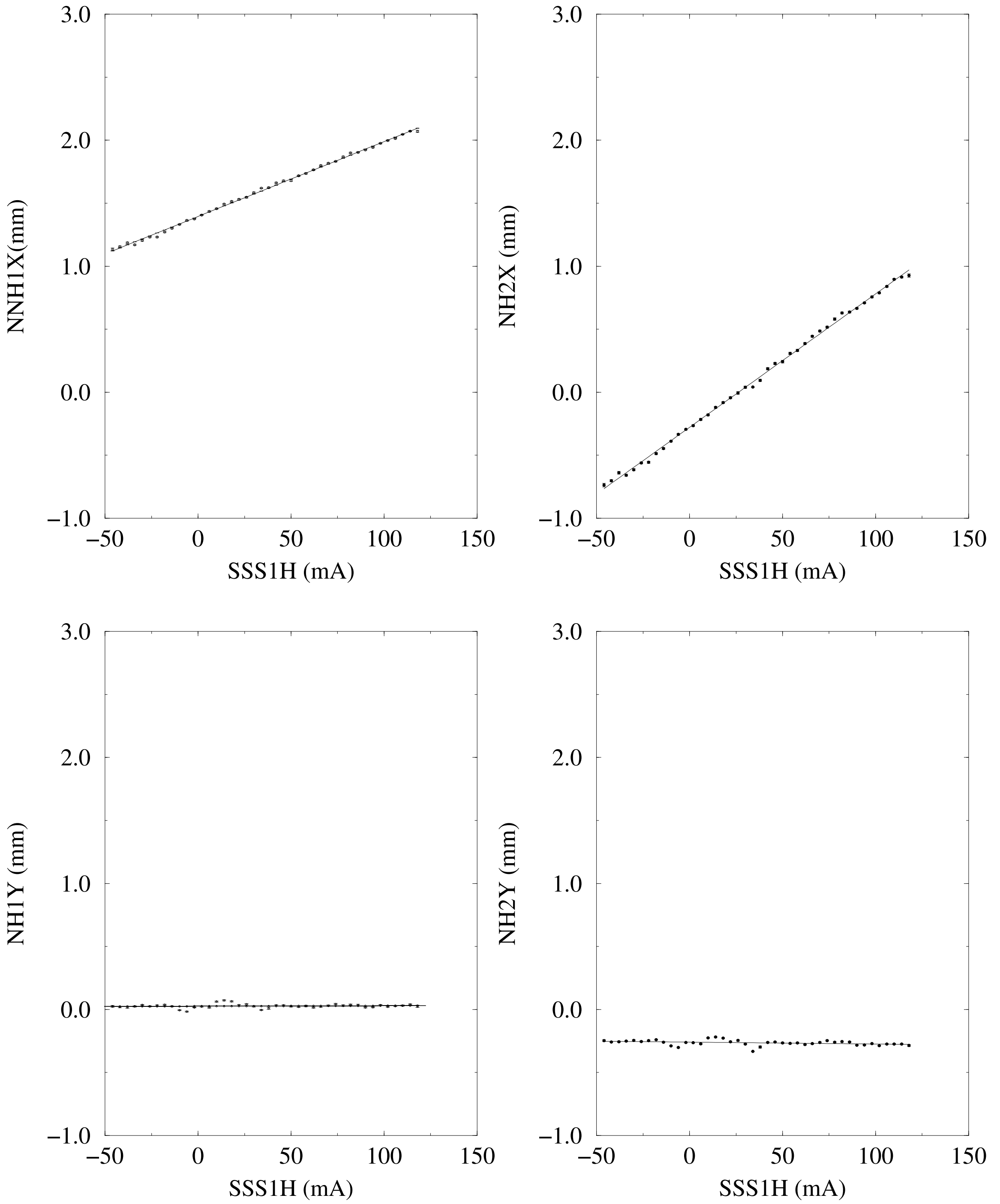

Figure 3.6: Beam position monitor response for different horizontal coil current settings.

Beam position monitors, located in an area of known energy dispersion (analogous to dispersion of light by a prism), are used to monitor the beam energy by measuring the beam position. The energy sensitive position monitor ECSX is calibrated to reproduce the previously measured beam loading of 2.3 MeV/mA. (Because there is significant 60 Hz noise, care must be taken when extracting the energy calibration coefficients to use pulse pairs (in general having different incident electron currents) separated by 1/60 th of a second.)A typical result is shown in Figure 3.7. The monitor DEX can be calibrated with the above technique as well. In principle, FPM1 and FPM2 can be used to establish the incident electron trajectory into monitor DEX in order to distinguish the position shift from the mean energy. This capability was not used in the present analysis.

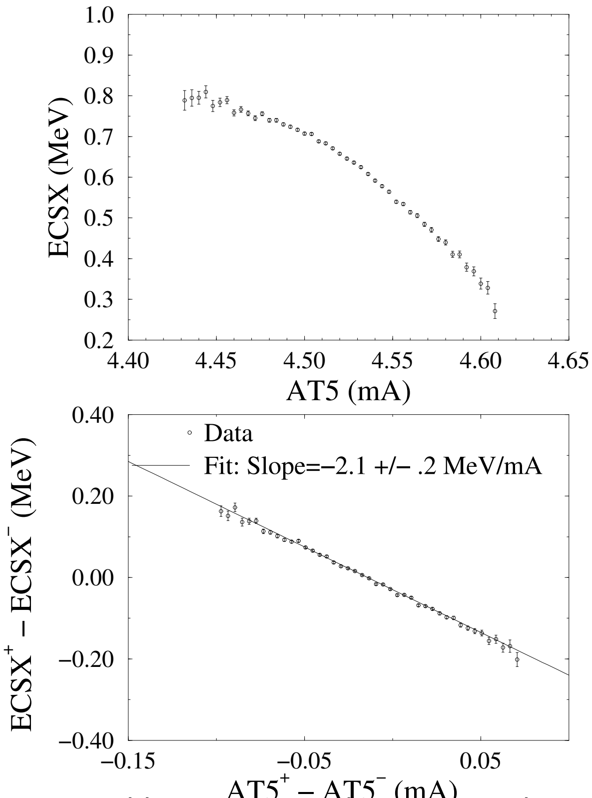

Figure 3.7: Energy monitor calibration using dispersion. The graphs illustrate how 60 Hz noise may be removed. The curved response of the ECS centroid relative to the centroid of the current measured at AT5 becomes linear when the difference between two ECSX centroids that are separated by 60 Hz is compared to the analogous difference in the current measured at AT5.

The current is measured using a transformer. The incident electrons induce a changing magnetic flux within a toroid of high permeability metal ("μ-metal") through which incident electrons pass. The changing flux induces a current in a load which is amplified. An additional wire is wrapped around the toroid to allow for calibration. The toroid is calibrated to an absolute uncertainty of about 0.1%.

Monitor Name	Property	Calibration Coeff.	Resolution
PTOR1	Current		
AT5	Current	576 chan/nC	~0.1%
MT1	Current	601 chan/nC	~0.1%
ST5	Current	855 chan/nC	~0.1%
STS6	Current	582 chan/nC	~0.1%
TTG1	Current	623 chan/nC	~0.1%
TTG2	Current	582 chan/nC	~0.1%
APM24X	Position		
APM24Y	Position		
MOLX	Position	838 chan/mm	
MOLY	Position	868 chan/mm	
NH1X	Position	132 chan/mm	~10 μm
NH1Y	Position	132 chan/mm	~10 μm
NH2X	Position	150 chan/mm	~10 μm
NH2Y	Position	200 chan/mm	~10 μm
ECSX	Energy	6 chan/keV	
FPM1X	Energy & Pos.	586 chan/mm	
FPM1Y	Energy & Pos.	350 chan/mm	
FPM2X	Energy & Pos.	543 chan/mm	
FPM2Y	Energy & Pos.	579 chan/mm	
DEX	Energy		

Table 3.2: Monitor calibration and resolution.

Halo monitors, typically small scintillators attached to a phototube, were located in two areas. SHALO and HALO are two halo monitors positioned after the last BPM in the North Hall and attached symmetrically around the beam pipe near a collimator. TUBE11 is a photomultiplier tube inside a lead shielding case similar to the typical SAMPLE detector but located outside the detector and used during the 1996 data set only. The halo monitors were operated at a fixed high voltage and provide a relative measure of the background.

Table 3.2 lists monitors in the data set along with the incident electron property measured, the average calibration coefficient, and the monitor resolution if known.

3.4 The Liquid Hydrogen Target

The polarized electrons are backscattered by a liquid hydrogen target. The closed loop system is shown in Figure 3.8. The pump in Figure 3.8 is a vaneaxial fan immersed in the liquid hydrogen and driven by a $\frac{1}{2}$ horse power motor mounted outside the liquid. The pump circulates approximately 25 liters of liquid hydrogen through a counterflow heat exchanger where the hydrogen is cooled by 15^{o}K helium gas. A rotary screw compressor delivers the helium gas at approximately 230 psig to the 750 W Process Systems International [42] model 1620-S refrigeration system. The temperature and pressure are monitored at several locations within the target. The power deposited by the 40 μA incident electron current is 500 W. The heater shown in Figure 3.8 is used to maintain this heat load on the target when the electron beam is off. As shown in Figure 3.9, the target remains 2K sub-cooled under both low and high heat loads. The incident electrons strike the target cell located at the bottom of the target loop and extending out of the drawing so that it is parallel to the incident electron velocity.

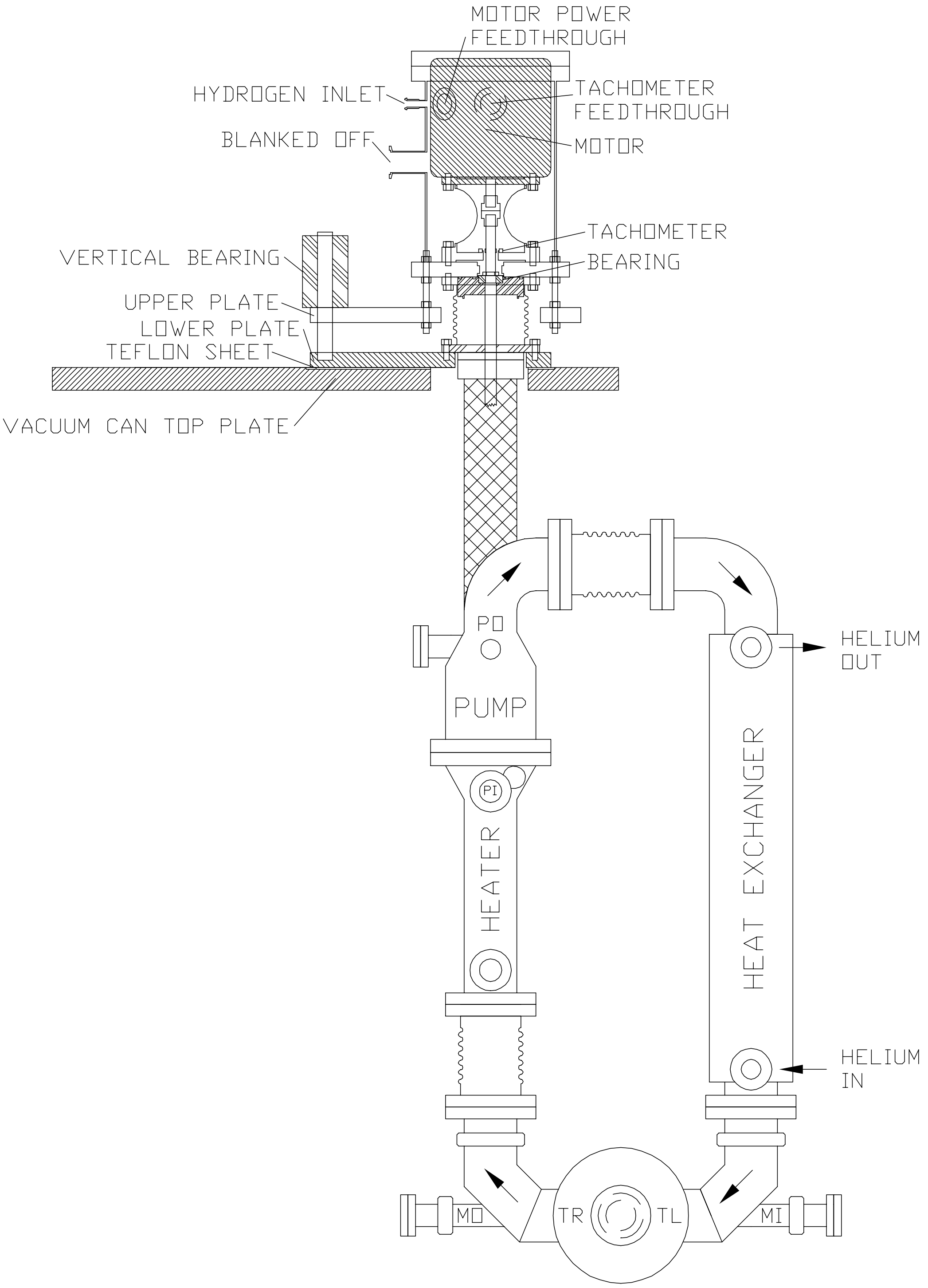

Figure 3.8: The hydrogen target loop. The target cell is located at the bottom of the target loop and extends out of the drawing. Temperature sensors on the left and right of the target are labeled "TL" and "TR" respectively. Pressure sensors at the pump input (PI) and output (PO) are used to measure the pump head pressure. The manifold input and output pressure monitors are labeled "MO" and "MI" respectively. The target position can be adjusted horizontally and vertically by means of the teflon plate and the vertical bearing, respectively.

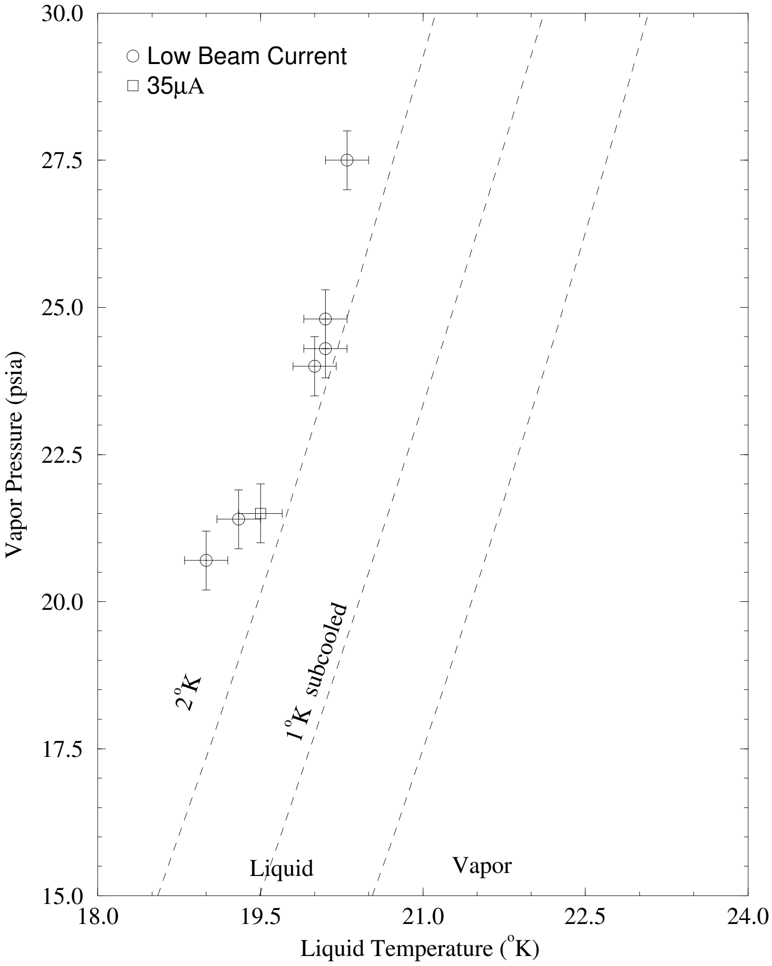

Figure 3.9: Performance of the liquid hydrogen target for two different incident electron currents

The target cell is shown in Figure 3.10. Hydrogen flows through a central cylinder tapered from 6 cm to a diameter of 3 cm near the entrance window to maintain a high flow rate. The liquid hydrogen reaches longitudinal flow rates of about 2.5 m/sec and is directed anti-parallel to the incident electron velocity[43]. Holes in the inner cylinder add a transverse component to the LH_2 flow and help the target carry away the heat generated by the incident electrons. The liquid returns along the outside of the central cylinder to the manifold where the liquid exits the target. The inner and outer tubes are 0.13 mm and 0.38 mm thick respectively. A helium backing cell, at a pressure slightly in excess of the LH_2 target pressure, is used to support the target

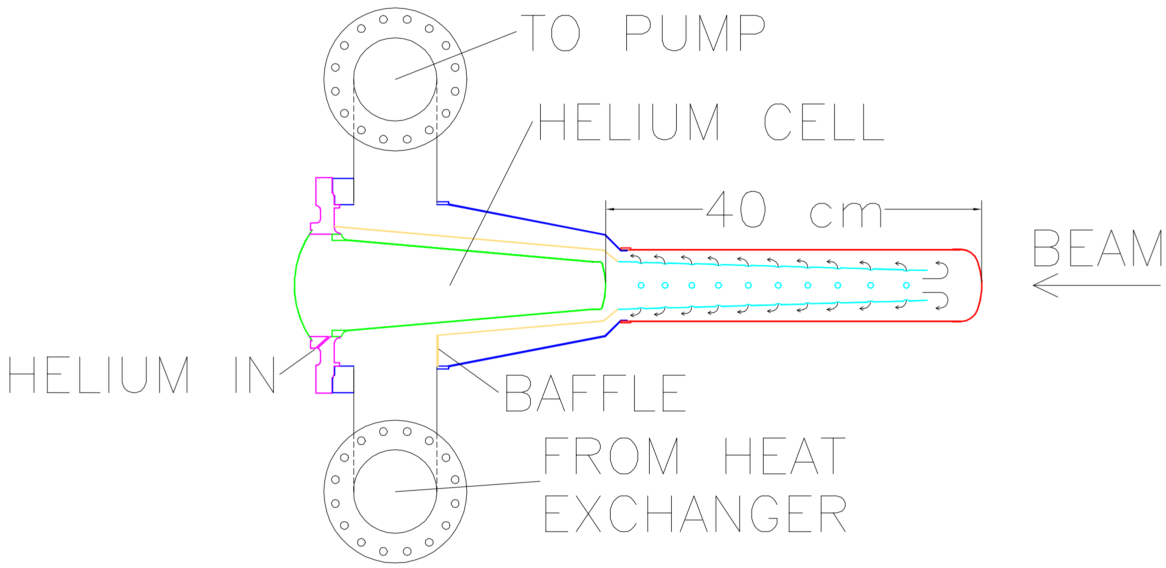

Figure 3.10: The Hydrogen Target Cell

exit window such that the exit and entrance windows have the same curvature and therefore a constant target length, to first order, independent of the incident electron position on the target entrance window. The thickness of this helium gas is negligible compared to that of the liquid hydrogen target. The target cell is enclosed in an aluminum scattering chamber 3 mm thick in the geometrical form of a cylinder 50 cm in diameter with a hemispherical end cap (see Figure 3.12).

3.5 Detector

The three fundamental detector elements (target cell, mirror and Čerenkov detector pair) are shown in Figure 3.11a. For clarity, only six of the approximately 3,000 electrons that backscatter with each incident pulse are shown in Figure 3.11a. Each backscattered electron generates Čerenkov radiation in a conical pattern with an approximate half angle of 1.3 degrees which produces a circular image on the detector mirror that is about 1 in. in radius. As shown in Figure 3.11a the Čerenkov radiation is reflected onto the face of the photomultiplier tube. Figure 3.11b shows the light yield measured by the photomultiplier when an LED, focusing a one inch diameter circular image on the mirror, is used to scan the mirror surface. Figure 3.11c is the image observed on the face of the PMT when a 40cm long fluorescent light was placed at the locatation of the target.

A symmetric system of 10 ellipsoidal mirrors (see Figure 3.12) is placed in front of the target such that the center of each mirror occupies one of the positions in Table 3.3. The equation describing the surface of each mirror is shown in Table 3.4. The ellipsoidal mirror shape is chosen to focus the radiation produced along the target length (Z-axis) on the face of the PMT. A mold is machined using standard CNC milling techniques to accept a 62.6 cm square glass which will be slowly heated until it conforms to the contour of the mold given by the mirror equation in Table 3.4.

Each PMT (described in Appendix A) is housed in a 10 cm thick lead cylinder to reduce the line-of-sight background from the target. Contributions to the detector signal are investigated by closing shutters on the face of each lead cylinder and placing covers over each mirror to cut off the Čerenkov signal (see Chapter 4). The Čerenkov detector and target cell are enclosed by a light-tight and gas-tight aluminum shell to facilitate the use of different Čerenkov gases and improve the signal if necessary (not implemented for this data set).

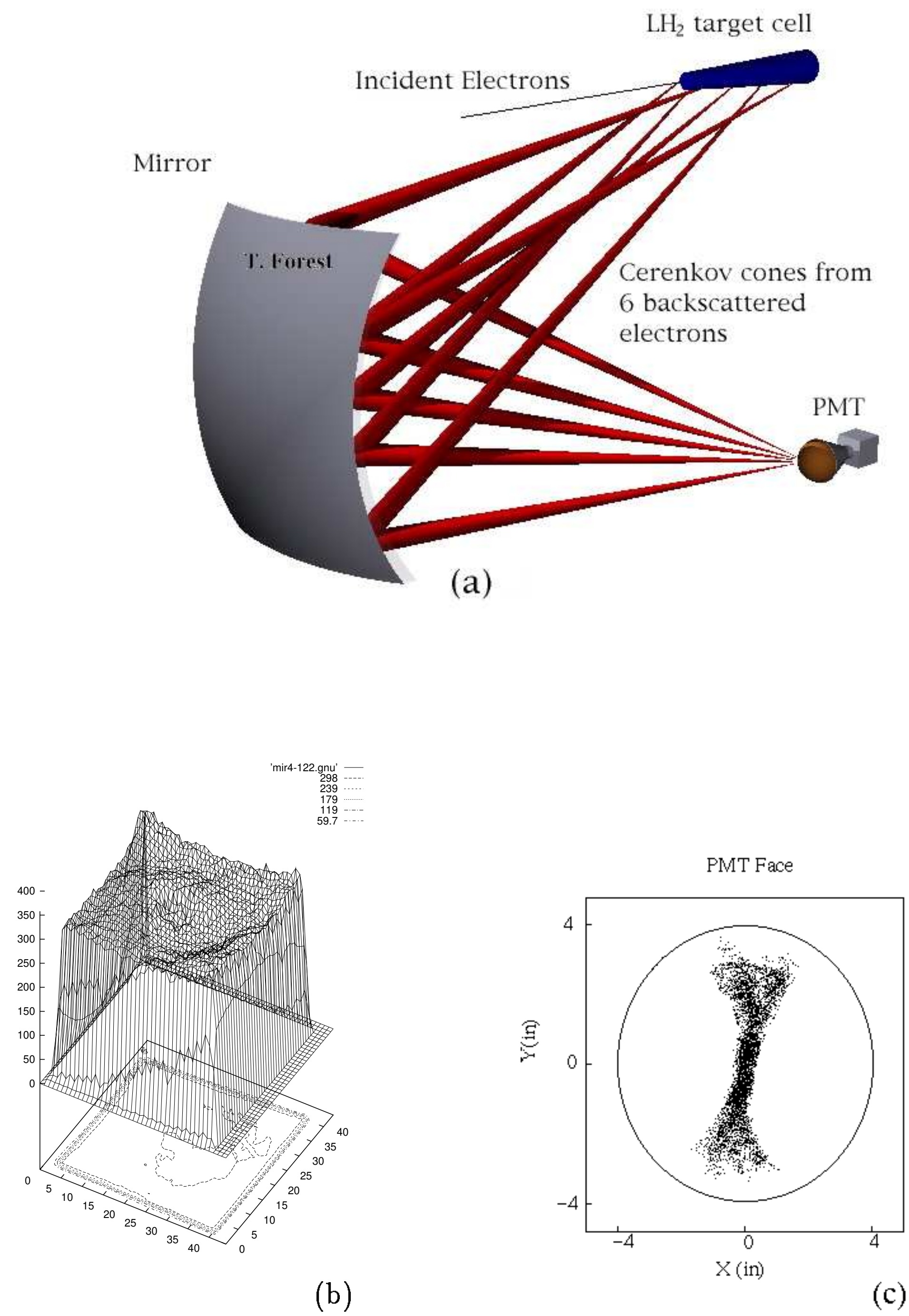

Figure 3.11: Primary elements of the SAMPLE detector. Figure (a) shows the LH$_2$ target, the detector mirror and its associated photomultiplier pair along with the Čerenkov cone for six backscattered electrons. Figure (b) is mirror reflectance measured by the photomultiplier tube when the mirror surface is scanned with a light emitting diode (LED) focussed to an image size one inch in radius on the mirror surface (positions are measured in radians and have been multiplied by 100). Figure (c) is the expected image seen on the face of the eight inch photomultiplier tube (the image was confirmed using a 40 cm long fluorescent lamp in place of the target.).

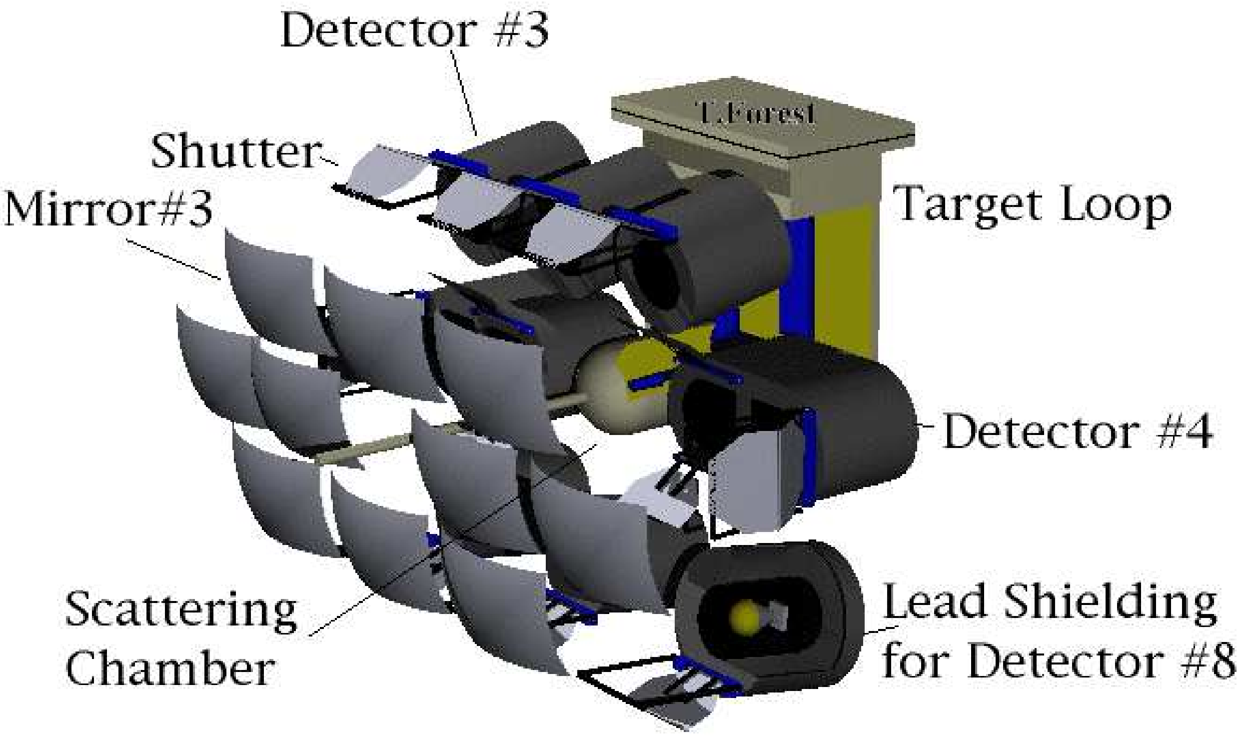

Figure 3.12: The SAMPLE detector. Artificial cutouts have been made of a detector shielding cylinder, the scattering chamber and the target loop containment vessel as a visual aide

Several addition shielding elements were included in the experimental setup to minimize the background. A 60 cm thick iron-loaded concrete ("heavy concrete") wall was erected 3 meters in front of the detector and centered about the incident electron path. The beam line was also covered with lead at several locations. Outside the detector, a lead wall (see Figure 3.13) was placed between the concrete wall and the detector. The beam pipe flange and collar located at the upstream detector wall was encased with 2×4×8 inch lead bricks in a symmetric fashion. Inside the detector the beam pipe was wrapped with 20 mm of lead and tapered to prevent blocking Čerenkov light en route to the mirror array from the target. Lead shielding, 2mm thick, was also placed symmetrically around the scattering chamber to attenuate X-rays being generated from Compton scattering of bremsstrahlung photons off the atomic electrons in the target. A 1 mm lead curtain was installed against the downstream detector wall behind the scattering chamber in June 1996. This blanket decreased the background without decreasing the light yield. With the exception of the lead blanket, the apparatus shielding was unchanged during production data-taking (since Sept. 1995). As a result of these shielding elements the scintillation yield was reduced by an order of magnitude and now contributes less than 30% to the Čerenkov signal.

Detector	θ (Degrees)	ϕ (Degrees)	Distance (cm)	L_{rad} (cm)	$\Delta\Omega$ (sr)
1	145.9	135.8	171.6	128.8	.133
2	154.0	90.0	151.7	104.6	.170
3	145.9	44.2	171.6	128.8	.133
4	138.4	180.0	182.1	144.3	.118
5	160.5	180.0	153.0	103.2	.167
6	160.5	0.0	153.0	103.2	.167
7	138.4	0.0	182.1	144.3	.118
8	145.9	224.2	171.6	128.8	.133
9	154.0	270.0	151.7	104.6	.170
10	145.9	315.8	171.6	128.8	.133

Table 3.3: Mirror positions from the center of the LH_2 target using a coordinate system with the Z-axis pointing along the incident electron momentum. The mirrors are 62.6 cm square. L_{rad} represents the actual radiator length which differs from the column "Distance" due to a scattering chamber surrounding the target.

Detector	α_0	α_1	α_2	α_3	α_4
1,10	-1.3284	0.90776	0.19199	0.90009	-0.18491
2,9	-0.42834	0.90212	0.0000	1.0000	0.0000
3,8	-1.9670	0.90776	-0.19199	0.90009	0.18491
4,7	-1.5503	1.0000	0.0000	0.84120	-0.25997
5,6	-0.024956	1.0000	0.0000	0.89028	-0.042197
	α_5	α_6	α_7	α_8	α_9
1,10	0.91444	$\pm$0.17767	$\mp$1.4355	$\pm$1.4940	-208.41
2,9	0.94940	0.14075	-1.2432	0.0000	-220.02
3,8	0.91444	$\pm$0.17767	$\mp$1.7468	$\mp$1.8179	-208.48
4,7	0.89360	0.0000	0.0000	2.2839	-215.59
5,6	0.99594	0.0000	0.0000	0.29811	-269.24

Table 3.4: Surface equation coefficients α_i defining each detector mirror. The mirror equation is $\alpha_0 + \alpha_1 x^2 + \alpha_2 xy + \alpha_3 y^2 + \alpha_4 yz + \alpha_5 z^2 + \alpha_6 xz + \alpha_7 x + \alpha_8 y + \alpha_9 z$. The $\pm$ and $\mp$ signs in columns α_6, α_7, and α_8 indicate a sign change with the upper sign being associated with the lower detector number in the detector pair.

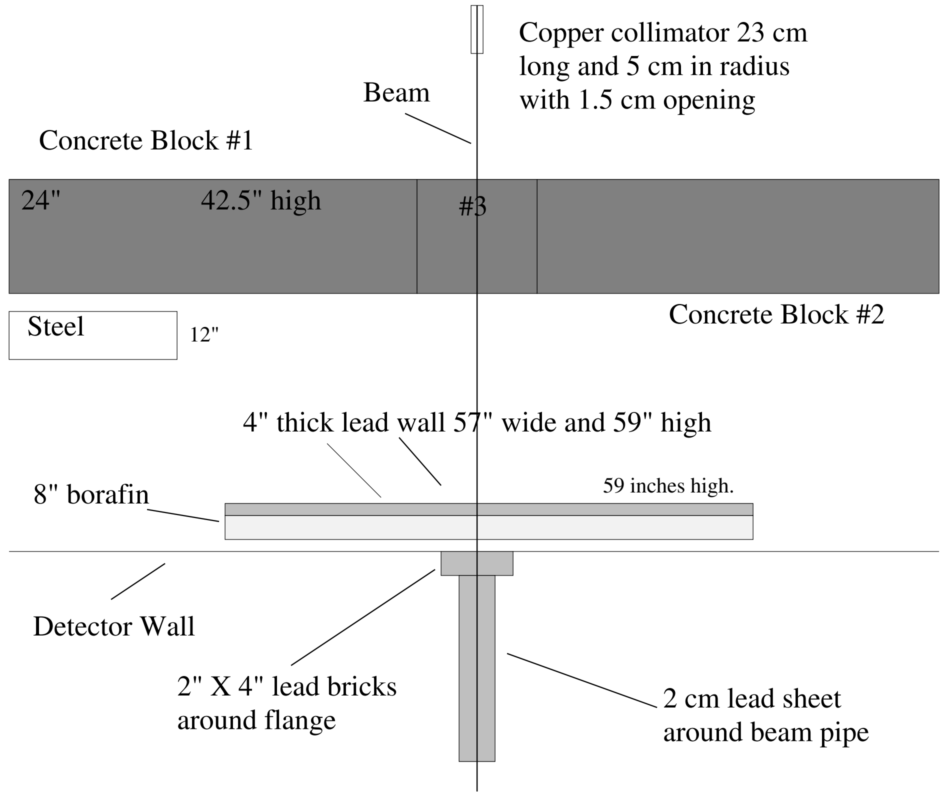

Figure 3.13: Shielding elements for the SAMPLE detector.

3.6 Experimental Timing

The polarized source generates electron pulses at a rate of 600 Hz which are line-locked to the 60 Hz power line. The same 600 Hz signal is used to trigger the klystrons which provide r.f. power to the accelerator (see Figure 3.14). This "Master Trigger" is the start of all timing in the experiment. One feature of such a line-locked trigger is to minimize the influence of 60 Hz noise on the asymmetry measurement - implemented as follows. The helicities of 10 consecutive pulses are generated randomly at the polarized source for 10 "timeslots" (an example is shown in Figure 3.14). The next 10 pulses will contain the helicity complement of this initial pattern and facilitate the calculation of 10 separate pulse pair asymmetries, one for each timeslot. Subsequently a new random set of 10 helicities is chosen and the cycle repeats. The pulse pair asymmetries are weight averaged at the end of each 30 minute running interval ($\sim 5 \times 10^5$ pulse pairs). The data acquisition timing is similar to that used in the ^{12}C parity experiment[44] with the most important exception being that the integrate gate is at 28.57 μsec instead of 22.0μsec (see Figure 3.15). This integration width was chosen to minimize the influence of $\sim$70 kHz noise found on the signal lines. The origin of this noise could not be determined and the noise could not be completely eliminated from the signal.

3.7 Data Acquisition

The "Master Trigger" signals a microprogrammable branch driver (MBD) to begin processing predefined events which transfer the data from a CAMAC standard electronics to a μVAX computer (see Figure 3.15). Due to the high event rate, the detector signals (see Table 3.5) are integrated before being received by the μVAX based data acquisition system. Experimental conditions are monitored in real time by analyzing a small percentage of the events using the "Q" data acquisition system developed for the Los Alamos Meson Physics Facility. A similar system in place at the polarized source is responsible for generating the helicity and pedestal events (see

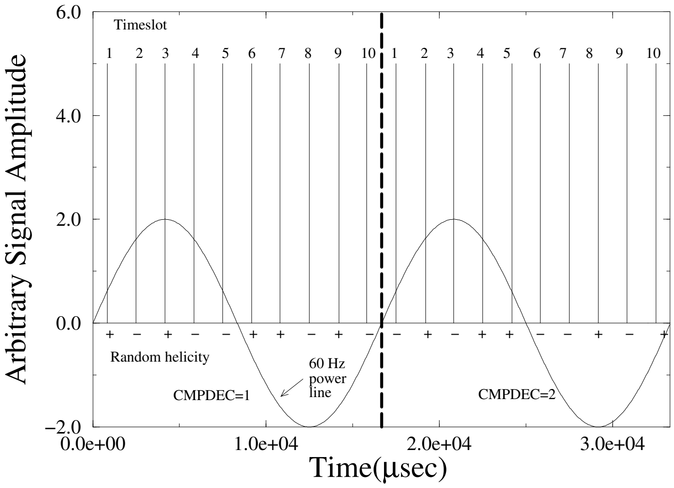

Figure 3.14: Timeslots and helicity information generated at the polarized source.

section 5.1).

To minimize the non-linearity effects of the ADC (see section 5.6) used to convert the integrated mirror and beam current signals, a random DC level is added using a binary sequencer (see Figure 3.15) to the integrator outputs using a "sum/diff" amplifier module. In order to remove this random DAC noise in software, it is necessary to experimentally calibrate the 16 bit ADC response to the injected DAC noise. This "DAC event" (event #7) is the event which performs the calibration task. After this calibration is done with the incident electron beam off, the electron beam is turned on and the second event type (event #6) begins to collect data for the asymmetry measurement. The electronics drift is at a sufficiently low level to permits limiting the calibration to once per day. Table 3.5 lists the 75 words in the data stream for event #6 which are sorted with respect to helicity for calculating asymmetries.

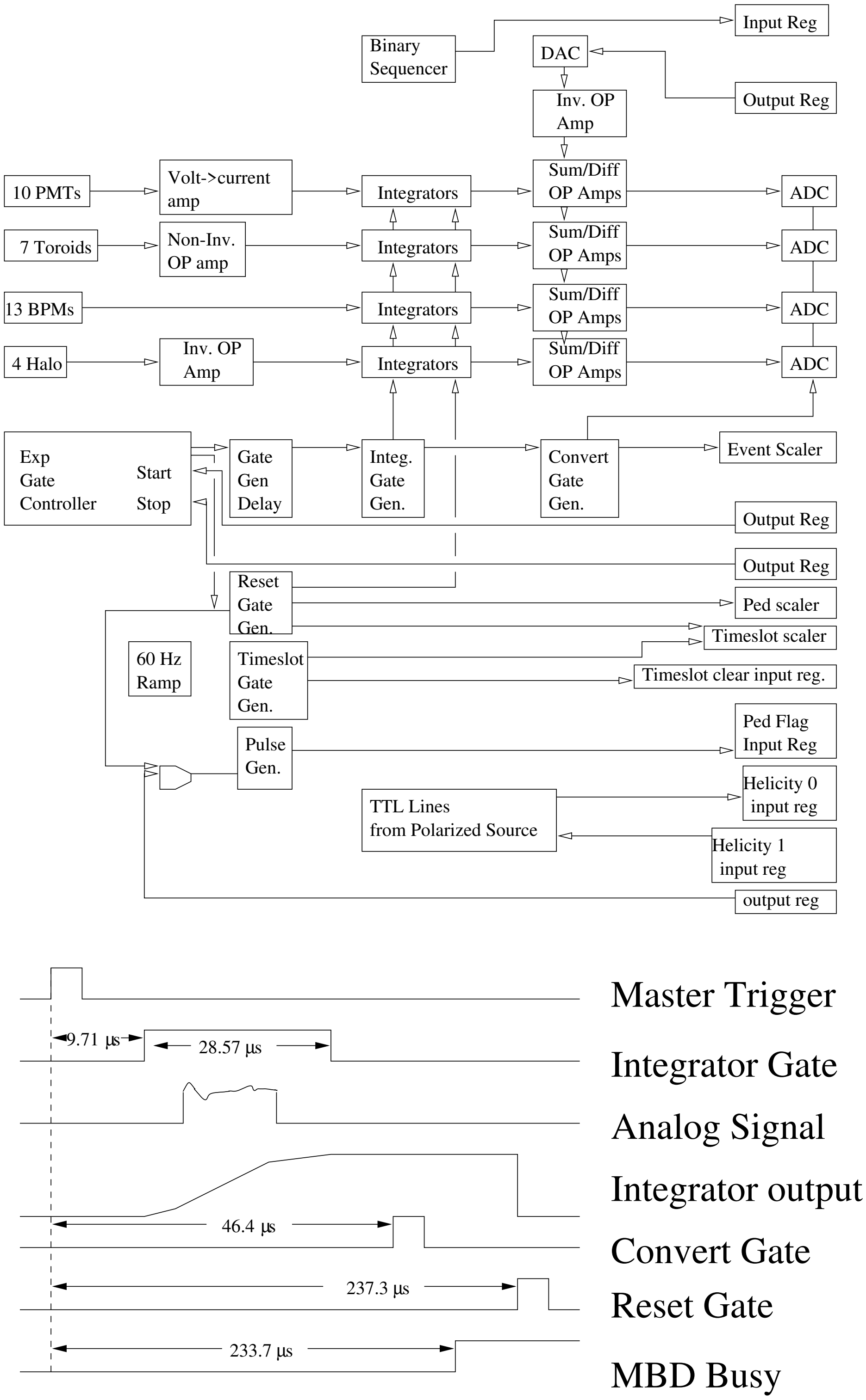

Figure 3.15: Data acquisition timing.

Word Number	Variable	Description
1	TYPFLG	=1 if pedestal event, =0 if data
2	IPLUSINPR	Helicity Bit, =1 if positive, =0 if negative
3	IMINUSINPR	Anti-helicity word, =1 if negative, =0 if positive
4	CMPDEC	=2 if new word, =1 if comp word
5	SCA60	60 Hz timeslot counter (1-10)
6	TMOUTFLG	=1 if ADCs failed to convert
7-46	IADC	40 ADC words
47	IDACOPR	DAC noise this event
48	IWRDAC	DAC noise next event
49-50	EVSCA	Mod pulse number (24 bit word)
51-52	EVSCT	Event Trigger number (24 bit word)
53-60	TGTDATA	Target information
61-73	COIL	13 Steering coil settings
74-75	ENERGYWORD	Fast Phase shifter setting (24 bits)

Table 3.5: The data stream for the SAMPLE main data event #6 used to calculate pulse pair asymmetries.

Chapter 4

Detector Signal Analysis

Although parity violation is directly observed, interpreting the physics of the measurement requires determining the contribution of elastically scattered electrons to the signal being measured. Standard data events measure all visible light in the detector that is associated with the incident electron pulse but are unable to determine if that light was generated by an elastically scattered electron or some other process. By acquiring data using low incident electron peak currents of $\sim 1\mu A$, individual electron events can be counted with traditional pulse counting techniques and the contributions to the signal being measured in the detector during high current data acquisition can be quantified. In the pulse counting mode the Čerenkov detector is supplemented with a pair of NaI detectors (energy calorimetry) and a scintillator paddle (charged particle detection). The scintillator paddle was placed in front of the NaI detectors or centered behind a mirror to facilitate a coincidence measurement. The response of the detector, in pulse counting mode, was modeled using a Monte-Carlo simulation based on GEANT[45].

4.1 The Pulse Counting Apparatus

The incident electron beam is generated by operating the polarized source such that the shutter Pockel's cell (see Figure 3.2) is nominally closed for nine of the 10 pulses within the 60 Hz cycle (see Fig. 3.14). The Pockel's cell is open 1/10th of the time, with the laser at reduced power, to generate a sufficient current (a "tracer bullet") to enable the accelerator operators to maintain the beam. The remaining nine pulses have a peak beam current of $\sim 5\mu$A that can be adjusted by slightly rotating one of the linear polarizers in the shutter Pockel's cell to generate a leakage laser beam. The event rate from this "leakage current" is $\sim$ 2-4 events/pulse.

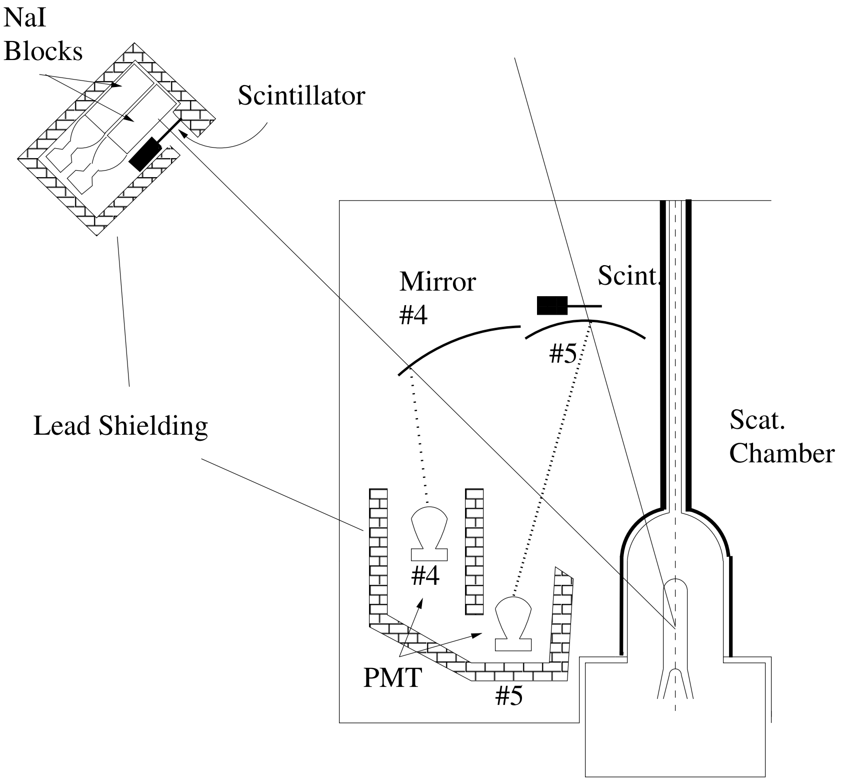

Figure 4.1: Orientation of the detectors in the pulse counting setup. The backscattered electrons pass through mirrors used to focus Čerenkov light onto photomultiplier tubes. Only detectors #4 and # 5 are shown for simplicity. Electrons which pass through the focusing mirror for detector #4 will hit a 4" x 6" x 1mm scintillator paddle and then pass through two 6"x 6" x 11" NaI crystal blocks.

4.1.1 Detectors and Electronics

The pulse counting apparatus for two different operational modes is shown in Figure 4.1. In the first operational mode, Čerenkov detector # 4, located at a scattering angle of 138 degrees, is used together with a scintillator paddle, for detecting charged particles, and a pair of NaI energy calorimeters. The scintillator and NaI crystals are oriented with respect to the Čerenkov detector to observe the charged particles that pass through the lower beam right side of the detector focusing mirror and through the black photographer's cloth which is used as the door to the light tight detector. The second pulse counting operational mode positions only the scintillator behind each mirror used for three other Čerenkov detectors (#1, #2, & #5 shown in Figure 3.12). The apparatus for detector #5 is shown in Figure 4.1.

An independent data acquisition system was used to record data from the SAMPLE detector and the supplementary detectors during low incident current operation. Figure 4.2 is a schematic of the electronics used in the pulse counting apparatus. Coincidence events are defined using the Čerenkov detector, the scintillator and in some cases the NaI detector. All recorded events are required to be within 50 μs of the "leakage current" timeslots and are rejected if they occur within the "tracer bullet" timeslot. To allow for a more flexible off line analysis, five different event triggers were defined to record the pulse counting data. One event type (P) defines pedestal events which are triggered randomly within the $\sim$ 50 μs timing window by an external oscillator such that pedestals occur once every second in the data stream. A second event type (C) defines events having a Čerenkov signal which passes a 50 mV discriminator threshold. These events are prescaled by a factor of 256. Two coincidence event types are also defined. The first coincidence event type (SC) is defined by having the scintillator discriminator fire within 100 ns after a Čerenkov event. The second coincidence event (SNnC) requires a scintillator and NaI event without a Čerenkov event. The fifth event type (NnSnC) records NaI signals when there is neither a scintillator nor a Čerenkov event present. In order to normalize the data to the incident electron flux, a BIC integrator measures the total charge passing through the LH_2 target during an entire run using one of the toroids in the North Hall beamline.

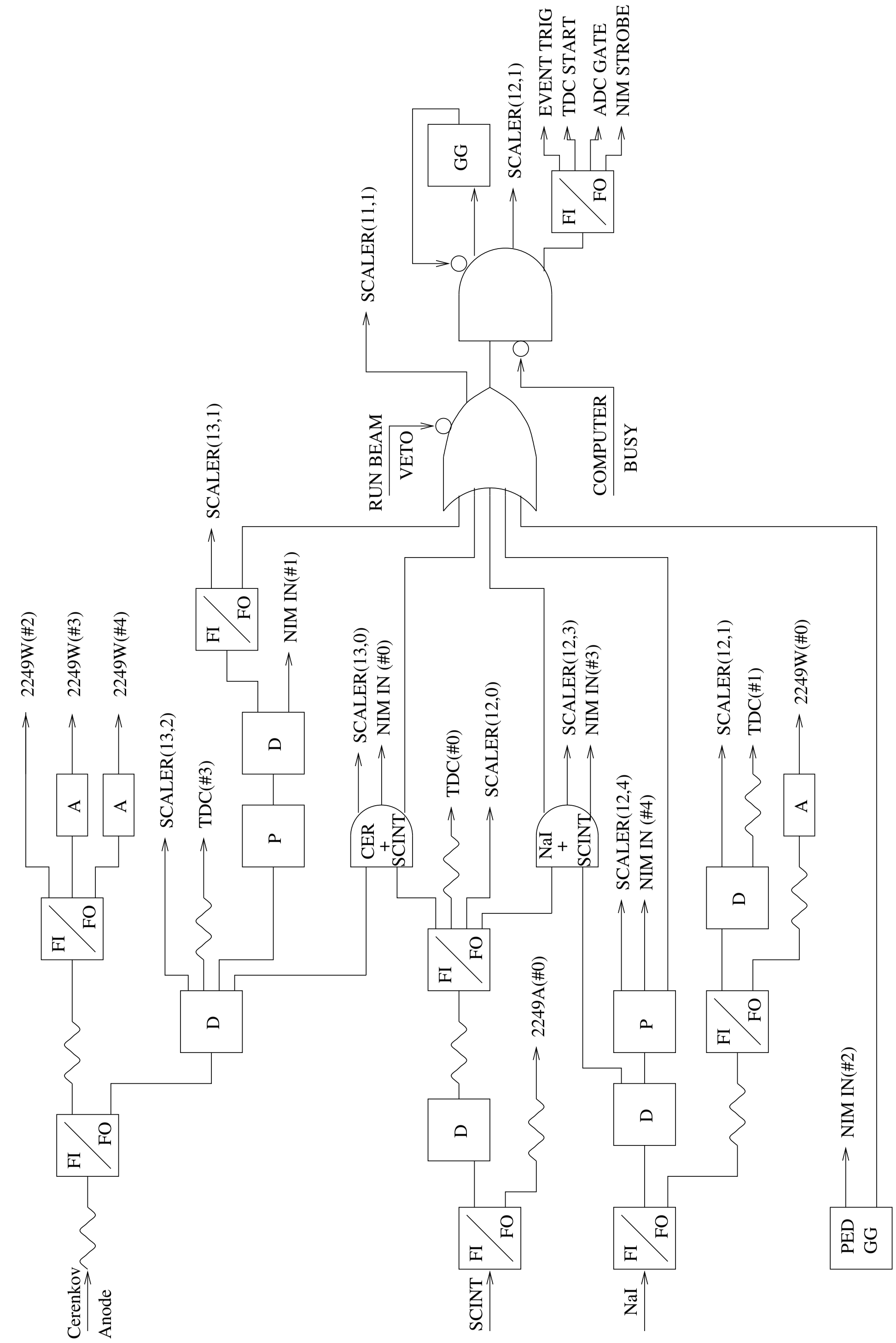

Figure 4.2: Wiring diagram for the pulse counting apparatus. A fan in/fan out module is denoted as "FI/FO", a discriminator as "D", an amplifier as "A", a prescaler as "P", and a gate generator as "GG". The gate generator located at the "computer busy AND" outputs a $50\mu s$ pulse to veto events once an event has been seen in a given beam pulse to prevent further events from accumulating.

4.1.2 Čerenkov Detector Calibration in Pulse Counting Mode

The Čerenkov detectors were calibrated using a light emitting diode (LED) and the pulse counting electronics. The high voltage setting used in pulse counting , higher than for normal running, makes it possible to see single photo-electron (PE) events. The single photo-electron peak is established by increasing the LED output until a shoulder appears, indicative of a double photo-electron event (see Figure 4.3). Table 4.1 lists the gain for the Čerenkov detectors. The gain measured for detector #4 is used to calculate the cross section in Section 4.6.2.

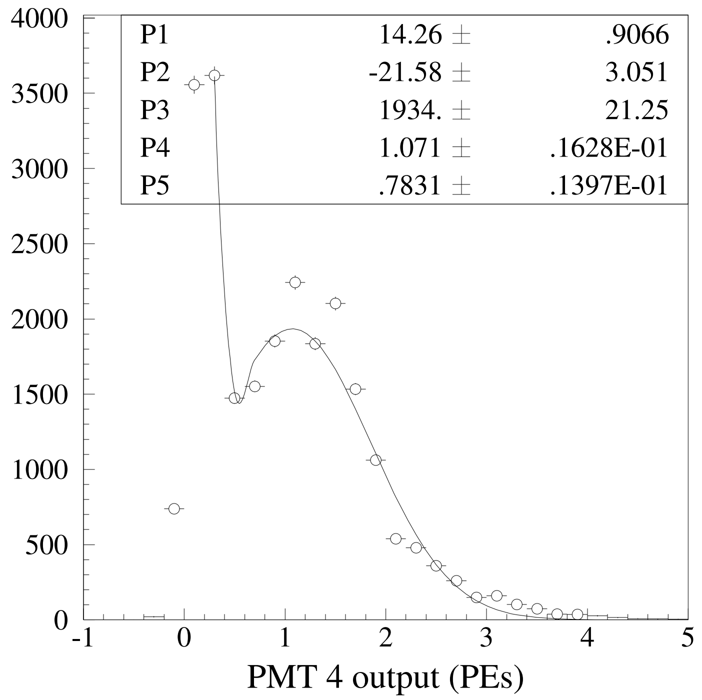

Figure 4.3: Calibrated photo-electron (PE) spectrum for detector #4 using LEDs and the pulse counting electronics. The pedestal is shown centered about 0 PEs and the single PE peak is present along with a 2 PE shoulder. Fitting the spectrum to an Exponential plus a Gaussian shows the single PE peak at 1.07 ± 0.02 PEs.

Detector	High Voltage (Volts)	Conversion Coeff. (Chan/PE)
1	1462	17.22
2	1375	22.20
4	1350	18.75
5	1378	23.50
6	1358	22.31
9	1362	24.60

Table 4.1: The conversion coefficients for each Čerenkov detector are listed for the high voltage settings used while taking pulse counting data

4.1.3 NaI Energy Calibration

The NaI detectors are calibrated using 200 MeV electrons and cosmic rays. First, both NaI detectors were placed directly in the path of the low current 200 MeV electrons generated by the accelerator. Figure 4.4 shows the un-normalized ADC spectrum having a mean of 1741 channels (1415 from NaI #1 and 326 from NaI #2). Repeating the measurement with the electronics to the NaI detectors swapped results in an un-normalized spectrum with a mean of 1672 channels (1363 from NaI #1 and 309 from NaI #2). A GEANT simulation of the NaI blocks predicts that 186 MeV will be deposited under such conditions. The gain in each NaI detector was determined, using the above two data sets, to be 9.5 channels per MeV for NaI #1 and 8.9 channels per MeV for NaI #2 . Unfortunately, this method absorbs any gain differences between the two electronics channels used to record the output of the NaI detectors. Ideally the two electronics channels would be identical. To determine the energy sensitivity of both detectors as a system, at least one additional energy setting would be needed.

Second, cosmic rays are used to extend the above calibration. However, the low flux requires extended running times. The large energy range of cosmic rays further complicates matters. Figure 4.5a shows the energy deposited in the NaI detector as a function of incident muon energy using a GEANT simulation. The first data point

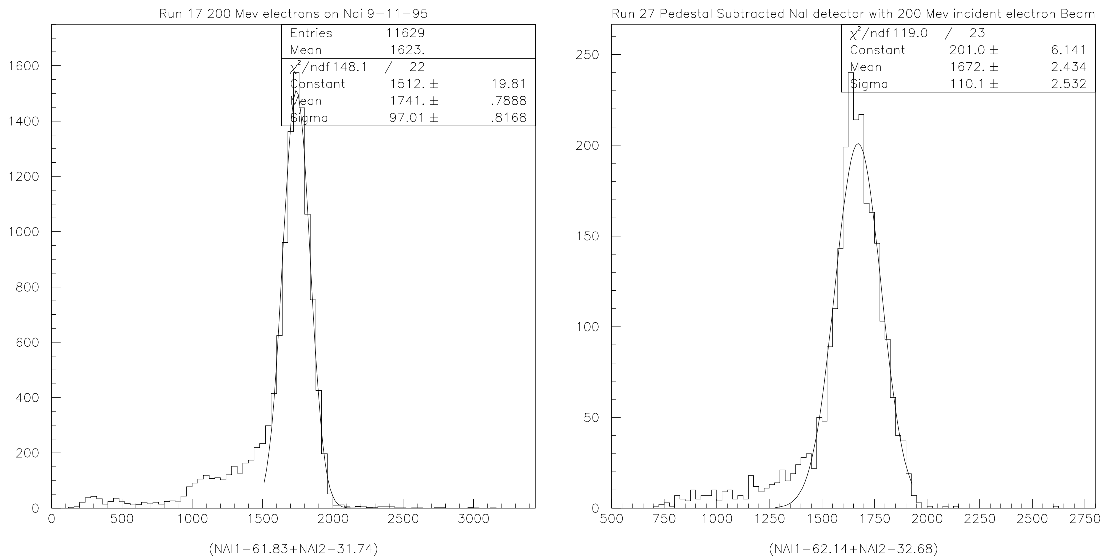

Figure 4.4: Raw energy histogram of the 200 MeV electron beam (pedestal subtracted).

corresponds to the maximum cosmic ray flux[46]. The cosmic ray flux decreases as the energy increases beyond that point. After an initial decrease, the energy deposited in the NaI detector by the cosmic muons increases. This is the result of combining a decreasing muon incident flux with the increasing muon energy. Weighting the cosmic ray energy by the flux results in an average muon energy of 0.783 GeV. The average muon energy, when combined with a parabolic fit to the GEANT prediction in Figure 4.5a [1], predicts an average deposited energy of 80.84 MeV in each NaI block. A linear fit of the calibration coefficients from both data sets, which contains (0,0) as a data point, results in a normalization coefficient of 9.75 ± 0.93 (ADC channels/MeV) for the NaI spectrum.

4.2 Elastic ^{1}H(e,e) Scattering Simulation

A simulation of the experiment was done in two stages. First, a distribution of backscattered electron energies and positions within the target was generated (repre-

[1] Figure 10.11 on page 1256 of Reference [22] shows qualitatively similar results using Hydrogen and Iron

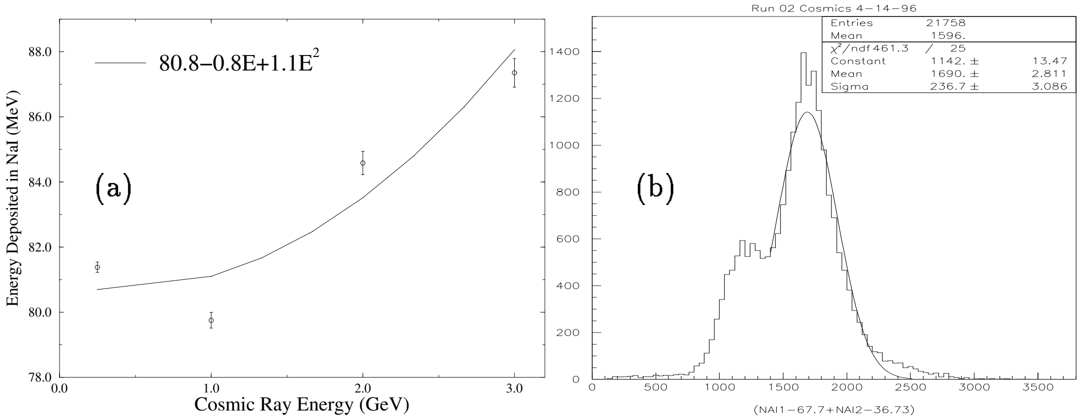

Figure 4.5: Cosmic ray energy spectrum. a.) spectrum represents specific cosmic ray energies as they would appear in the NaI energy spectrum based on a simulation. The line drawn is a fit to the data and has the form : Dep. Energy = 80.8 - 0.80 $\times$(Cosmic Energy) + 1.10$\times$(Cosmic Energy)^2. b.) spectrum is the data taken using cosmic rays of all energies.

Date	Run #	Dep E(MeV)	Chan.	Chan./MeV	Source
4/14/96	2	161.70	1689.6 ± 2.81	10.45	Cosmic Rays
9/11/95	17	186	1740.8 ± .79	9.34	200 MeV beam
			Calibration Fit	9.75 ± 0.93	

Table 4.2: Total energy deposited into NaI using cosmic rays and the Bates electron source.

sentative of the energy the electron beam loses when traversing the LH_2 target). Next, these electrons were propagated from the target, through the scattering chamber, and chosen such that the photons generated by those backscattered electrons would reflect off of mirror #4 and be focused onto PMT detector #4 (see Figure 4.1). Each backscattered electron was followed, during this second stage, as it passed through mirror #4, exited the detector, and entered the scintillator and NaI detectors shown in Figure 4.1. The results of this second stage are then weighted by the elastic electron proton scattering cross-section to be representative of the interaction.

The backscattered electrons are generated by an incident electron flux which loses energy as it passes through the extended (40cm) liquid hydrogen target. The processes considered in calculating this loss of energy were Bremsstrahlung, ionization, multiple scattering, delta ray production, synchrotron radiation, and positron annihilation. A description of those processes and the calculations used may be found in Reference[45]. The resulting energy distribution from a simulation of these processes is shown in Figure 4.6 along with the distribution of the electron position along the target. The energy profile of the incident electrons changes from a delta function like distribution having a maximum value of 200 MeV to a distribution with a tail that extends well below 40 MeV. The initial linear fall off from the 200 MeV peak is due to the target length. The rise in the spectrum below 60 MeV is due to a combination of the increasing elastic cross section and the increasing probability of energy loss before scattering.

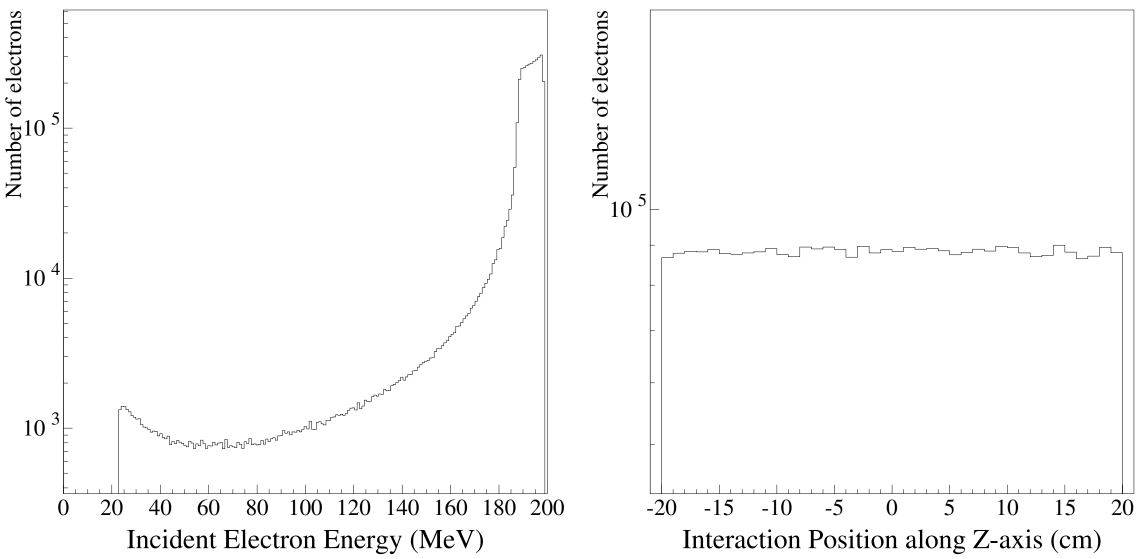

Figure 4.6: Energy and spatial distribution of incident and secondary electrons in the target. The energy spectrum has been weighted by the cross section of the reaction responsible for the energy loss and is for electron energies above the 24 MeV Čerenkov threshold.

The second stage of the simulation selects incident electron energies and positions randomly from the distributions in Figure 4.6. The simulation then follows elastic backscattered electrons, along with any photons, positrons, or secondary electrons generated by those electrons, to the scintillator and NaI energy calorimeter. The simulation categorizes the energy deposited by particle type: e^+, e^-, γ. A NaI detector resolution of 7.5% was used to broaden the simulated elastic peak to match the data. The NaI calibration is rescaled to 9.5 Chan/MeV so that the elastic peak of the data and the simulation overlap (this change is well within the calibration error).

4.3 Elastic Energy Spectrum

The simulation and data, taken in pulse counting mode, are used to extract information on the detector signal contributions to the observed energy and spectrum. Shielding used around the scattering chamber to attenuated X-rays generated within the target influences both spectra. A measurement of the elastically backscattered electron energy with and without this shielding element shows the extent of the electron energy attenuation from this lead shielding.

During the commissioning phase of the SAMPLE experiment, several shielding elements were put in place to minimize the background observed when the detector shutters are closed. The light yield (shutter open - shutter closed) signal was observed during this phase to ensure that it was not comprised by the added shielding. Of the shielding elements added in this manner, one was shown to influence the interpretation of the pulse counting data but have little influence on the data taken during integration mode. This particular shielding element consisted of a 2mm thick sheet of lead wrapped around the scattering chamber to reduce scintillation light that is thought to be generated by X-rays.

Bremsstrahlung radiation is produced in the target by the incident electron beam. The resulting bremsstrahlung photons, after Compton scattering at backward angles from the atomic electrons within the target, will have energies in the X-ray range (1-100 keV). Adding lead around the scattering chamber attenuates these X-rays and reduces the probability that they will scatter and generate scintillation light within the detector. This shielding element reduces the scintillation light by an order of magnitude such that the contribution of scintillation light to the Čerenkov signal is less than 30% (see Table 4.6).

Figure 4.7a is the energy spectrum observed in detector #4 (diamonds) along with the results of the simulation (line) with the scattering chamber shielding in place. Aside from the excess in the simulation at energies below 40 MeV, neither the data nor the simulation show an elastic peak due to the attenuation of the electron energy by the 2mm lead shielding around the scattering chamber. An elastic peak is observed in both the data and the simulation when the lead shielding around the scattering chamber is removed (see Figure 4.7b).

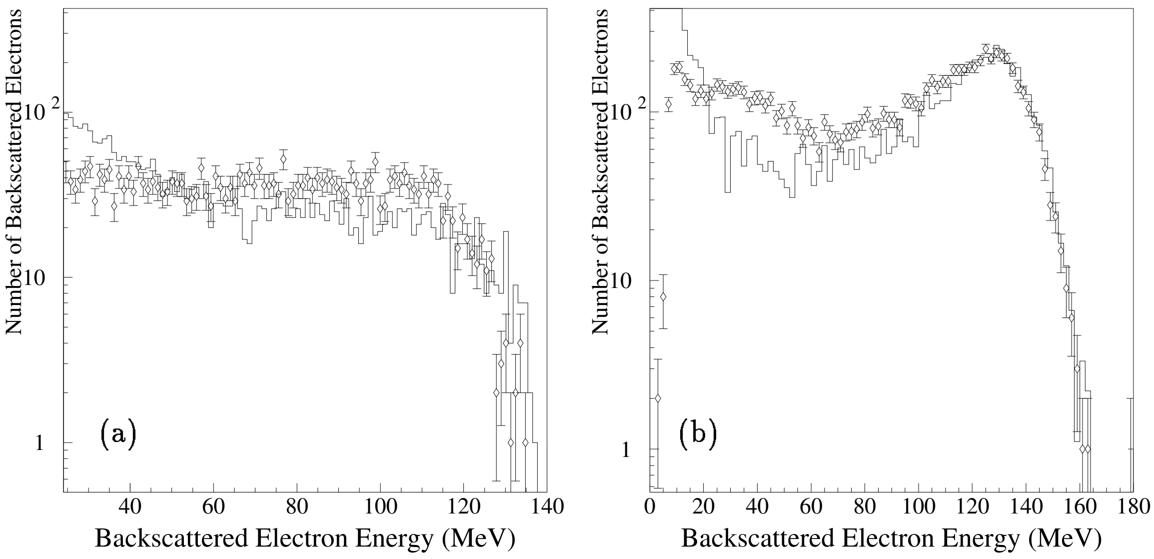

Figure 4.7: Energy spectrum, in pulse counting mode, of an electron elastically scattered from a proton at an angle of 140 degrees. a.) the spectrum with 2mm of lead around the scattering chamber. b.) the spectrum without the 2mm lead shielding. The data is denoted using diamonds and the simulation with lines.

4.4 Čerenkov Spectrum

The shift in the Čerenkov spectrum caused by this shielding element does not appreciable influence the detected signal. Figure 4.8a is the Čerenkov spectrum from the simulation with the lead shielding on the scattering chamber. Figure 4.8b is the Čerenkov spectrum which results after the lead is removed from the scattering chamber. The backscattered electron energy attenuation due to the scattering chamber shielding has a modest influence on the Čerenkov spectrum changing it from a mean of 29.20 to 26.78 photons generated per backscattered electron. This 8% shift in the integrated Čerenkov spectrum was not noticed due to fluctuations in the accelerator tune which can cause background levels to change by at least 8%. For an asymmetry measurement, this 8% shift is an acceptable alternative to the order of magnitude increase in scintillation light which would result without the scattering chamber lead shielding.

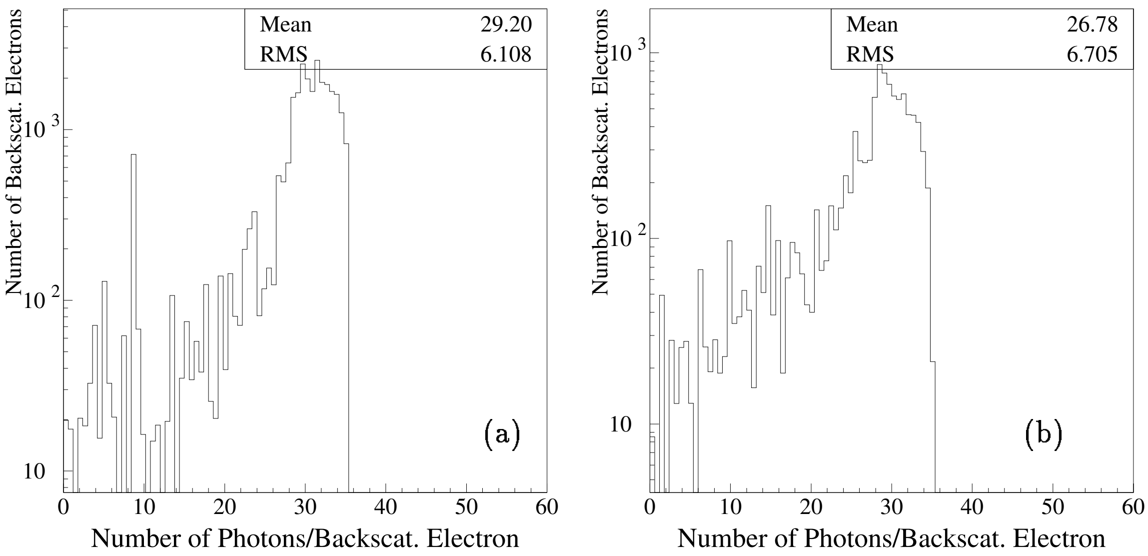

Figure 4.8: The Čerenkov spectrum of an electron elastically scattered from a proton at an angle of 140 degrees using the simulation. a.) the spectrum without the 2mm lead shielding. b.) the spectrum with 2mm of Lead around the scattering chamber. Note that the lead results in a photon loss of about 8%.

4.5 The Pion Contribution to the Elastic Energy Spectrum

The simulation used the energy spectra to determine the contribution of pion production to the observed light yield. The simulation is not representative of the data in Figure 4.7b between 20 and 60 MeV. A simulation which accounts for pion production may be the answer to the discrepancy. Pions can be either directly electro-produced or, as a result of electron bremsstrahlung, photo-produced in the SAMPLE target. Measurements of charged pion photoproduction[47], neutral pion photoproduction[48], and charged pion electroproduction[49] show that π^+ photoproduction has the highest cross-section of 10μb/sr. Figure 4.9 is a GEANT simulation of the positron energy distribution created by muons generated when charged pions are stopped in the SAMPLE target. This simulation was used, with lead shielding on the scattering chamber, in the analysis of Reference[50] to calculate the charged and neutral pion contribution to the integrated yield of 4.2 ± 2.5 %. The asymmetry in the pion yield is expected to be much smaller than 1 PPM[51].

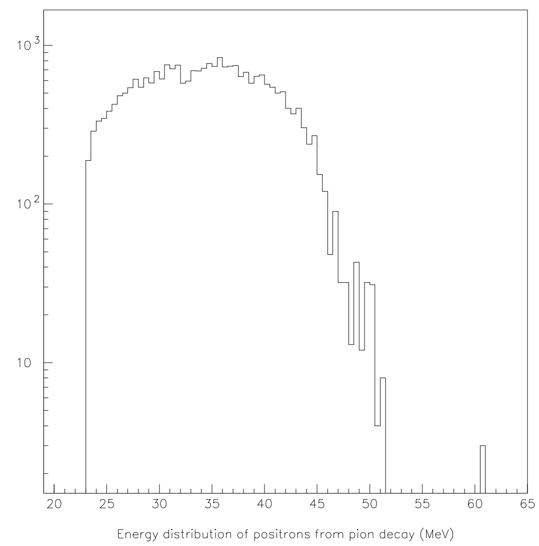

Figure 4.9: The energy distribution of positron from charge pion production in the SAMPLE target.

4.6 Contributions to the Integration Signal

The contribution of elastically scattered electrons to the signal measured by the phototubes with the lead shielding around the scattering chamber is determined by measuring the photon spectra in pulse counting mode. In addition to taking pulse counting data at the scattering angle of 138° corresponding to detectors #4 and #7 (where the NaI calorimeter was used), data was also taken at all other scattering angles corresponding to the remaining detectors using the second pulse counting operation mode (see section 4.1.1). Unfortunately, the geometry of the supporting structure prevented using the NaI energy calorimeter with the remaining detectors. The complete analysis of the integration signal is presented in Section 4.7.

4.6.1 Scintillation

Scintillation light is produced, primarily in air, by both charged particles and photons in the detector. Unlike Čerenkov light, scintillation light is emitted isotropically. A given particle will yield only a single scintillation photon due to the low density of air in the detector.

Scintillation light can reach the phototubes directly (without being reflected from the detector mirror) due to the isotropic emission of the light. In order to measure this component of the scintillation light, the mirrors, which normally reflect the Čerenkov light to the photomultiplier detector, were covered with black felt paper. The ratio of the signal from an individual covered mirror to the signal from the same mirror when it is uncovered, all other mirrors are covered for both measurements, is shown in Table 4.3. These measurements were made in both pulse counting and normal integration mode. The pulse counting measurements required only the detection of photons (Čerenkov singles) using data flagged as coincidence type SC (see Section 4.1.1) in order to be comparable with the integration mode data. The results are consistent. The ratio includes, in the denominator, the Čerenkov light (S_c), scintillation light from direct, non-reflected sources (S_o), the scintillation light reflected by the mirror (S_s) and the light generated by positrons from pion decay (S_π). The yield measurements are calculated by subtracting shutter closed measurements from shutter open measurements and then taking the ratio of the background subtracted yield seen when the mirrors are covered to the yield seen with the mirrors uncovered.

			S_o
Detector	Integration (Open)	Pulse Counting (Open)	Int Yield (Open-closed)
1,3,8,10	28.9 ± 0.6 %	20 ± 5%	11.23 ± 0.15%
2,9	35.9 ± 0.3 %	26 ± 7%	13.94 ± 0.01%
4,7	25.4 ± 0.2 %	19 ± 4%	9.38 ± 0.07%
5,6	44.6 ± 0.2%	38 ± 10%	12.61 ± 0.17%

Table 4.3: Direct scintillation ratio (S_o) measured for the integration and pulse counting data acquisition (SC event types as defined in Section 4.1.1) modes with lead around the scattering chamber. The shutter closed measurements were unable to observe any scintillation from the Čerenkov radiator. Scintillation was observed in detectors 5 and 6 which is the result of interactions with the aluminum shutter in the closed position. Uncertainties are statistical. The pulse counting measurements are from the work in Reference [50] shown in Table B.1.

Because the scintillation light is isotropic, there is some light reflected from the other nine mirrors into a given phototube. The signal contribution from other detector mirrors was measured using several permutations of individual mirror covers on and off measurements involving all the detector mirrors [2]. Table 4.4 quantifies the analogous ratios for this "cross talk" contribution to each detector type. The denominator of the ratios in Table 4.4 is identical to the denominator of the ratios in Table 4.3.

4.6.2 The elastic signal

Extracting the elastic scattering component of the measured signal requires the use of coincidence techniques. As the backscattered electron travels toward the mirror array, Čerenkov radiation will be emitted in a conical pattern which on the surface of the

[2]This "cross talk" was only measured after a 1mm lead sheet was installed in front of the target loop vacuum chamber.

	S_i
Detector	Integration Yield (Open-Closed)
1,3,8,10	6.6 ± 0.3%
2,9	8.7± 0.7%
4,7	15.3 ± 0.6%
5,6	3.7± 0.2%

Table 4.4: Contribution to the signal measured by each detector type from detector mirrors associated with the other detector types (S_i) using the data in Table 6.1 of Reference [50].

mirror looks like a 2" diameter disk. Electrons that pass close to the edge of the mirror will only have half of this circle reflected to the detector. For an isotropic electron distribution, the missing half circle will, under integration mode, be compensated for by an electron which just missed the mirror array thus there will not be a reduction in the net photon flux on the mirror. In pulse counting mode, however, individual electron events on the edge of the mirror will have a smaller fraction of the Čerenkov signal enter the detector acceptance than electron events located more than 1" from the mirror edge. A rise in the Čerenkov spectrum in the region with low PE events can be seen in data taken with the scintillator at the corner of the mirror (Figure 4.10a) as compared to data taken with the scintillator centered on the mirror (Figure 4.10b). Edge effects are one possible explanation of this feature. Edge effects will not influence pulse counting measurements taken using the scintillator paddle placed at least 1" from all mirror edges.

The scintillation light reflected from the mirror (S_s) is measured using coincidence techniques and mirror covers in pulse counting mode. The singles events shown in Figure 4.11 are measured using the entire mirror surface and suffer from edge effects. The coincidence events shown in Figure 4.11 do not suffer from edge effects and have been scaled by the ratio of the mirror area to the scintillator area. The scintillation light reflected by the detector mirror may be measured by subtracting the difference between the mirror cover on and off coincidence yield from the difference between the

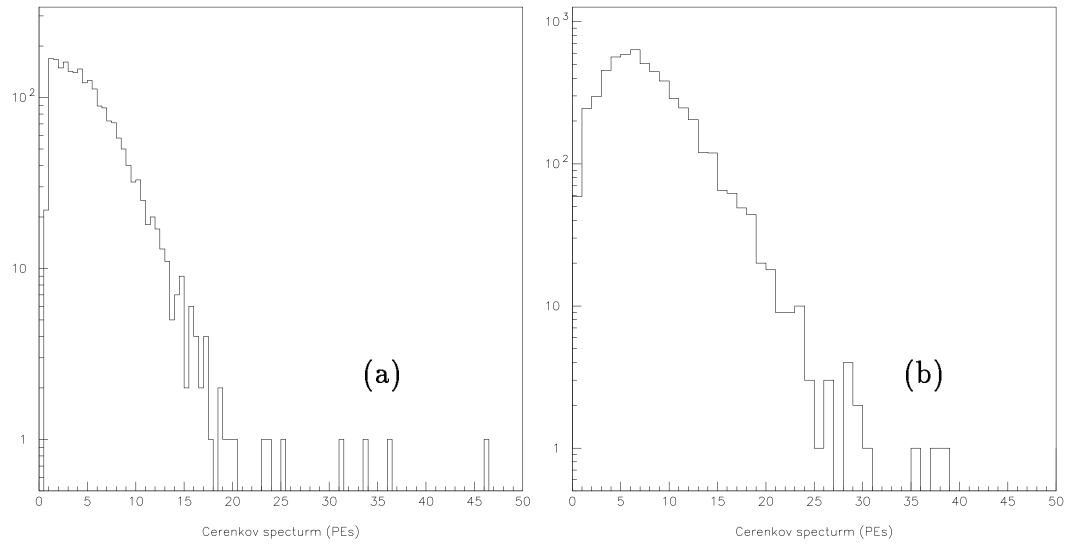

Figure 4.10: a.) Čerenkov spectrum from pulse counting data taken with the scintillator at the corner of a mirror. b.) Data taken with the scintillator mounted behind the center of the mirror.

singles yield with covers on and off (see Equation 4.6). Edge effects influence this measurement due to subtracting the singles yield from the coincidence. The detailed analysis in reference[50] places upper and lower limits on the value in Table 4.5. Since the edge effect only influences events located in a 1" perimeter around the mirror, a geometrical argument based on the ratio of the mirror area with and without this 1" perimeter would place the maximal edge effect to be at the 8% level. Accounting for the edge effect produced results that are consistent with Table 4.5.

Figure 4.12 is the signal component attributed to elastic electron scattering using coincidence requirements between the Čerenkov detector, the scintillator, and the energy calorimeter. The yield measured is 3.5 PEs/nC and is comparable to the expected yield of 3.16 PEs/nC. With the scintillator centered behind the mirror, the measured yield is 13.4 PEs/nC comparable to the expected value of 13.9 PEs/nC. The increase is brought about by the increase in solid angle. The measured yield of 13.4

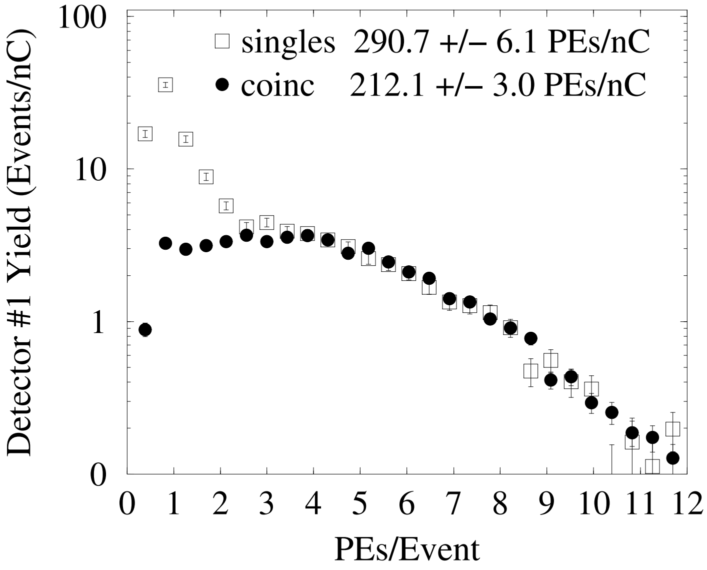

Figure 4.11: Singles and coincidence measurements using detector #1

	S_s
Detector	Pulse Counting Yield (Open-Closed)
1,3,8,10	8.4 $\pm$ 0.6%
2,9	8.0$\pm$ 0.5%
4,7	6.4 $\pm$ 0.4%
5,6	9.1$\pm$ 0.3%

Table 4.5: Contribution to the measured signal in each detector type from scintillation reflected by the detector mirror (S_s) using the data in Table B.2 of Reference [50].

PEs/nC is consistent with the coincidence yield of 212 PEs/nC in Figure 4.11 once the solid angle increase is accounted for (the 4" $\times$ 6" scintillator paddle compared with the 62 cm square mirror).

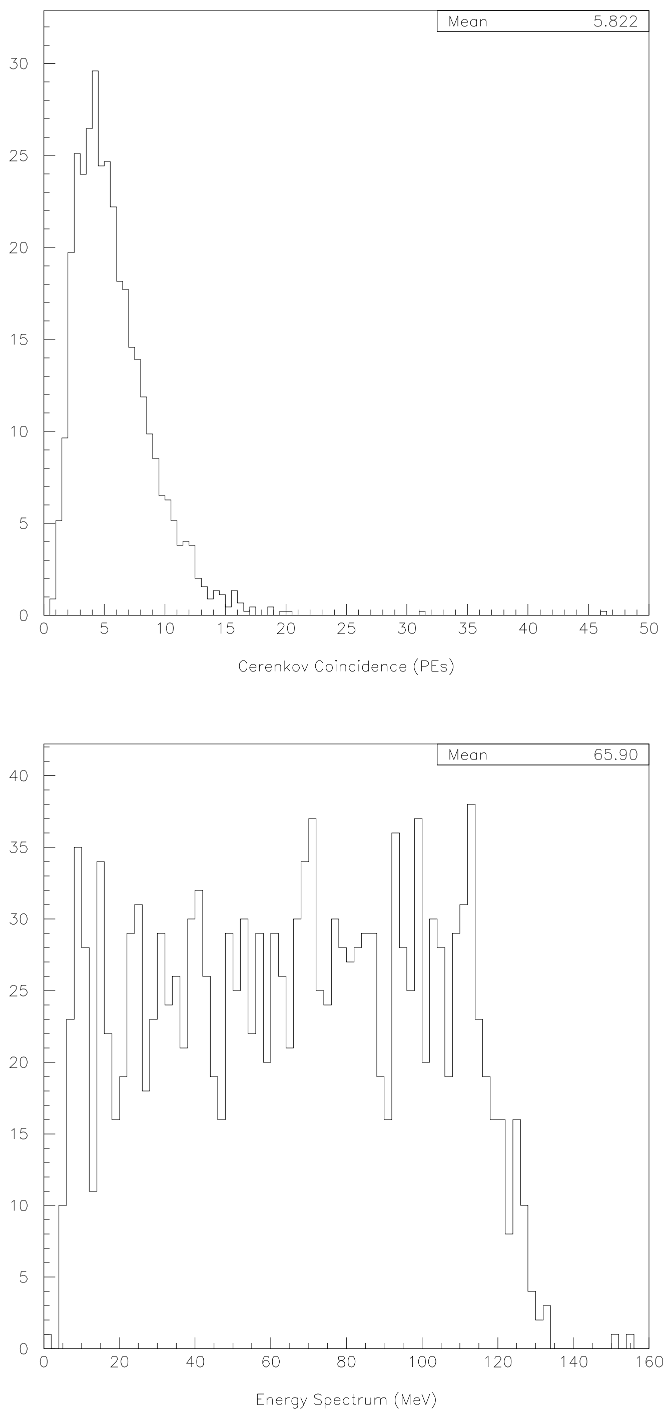

Figure 4.12: Measured yield and energy spectrum using the pulse counting apparatus with coincidence requirements on the Čerenkov detector, the scintillator, and the energy calorimeter with 2mm of lead around the scattering chamber.

4.7 Analysis of the Integration Signal

The integrated detector yield (shutter open - shutter closed) may be written as a sum of five components using the description in Section 4.6. The scintillation light that enters the photomultiplier tube but is not reflected by the intended detector mirror can be associated with either a direct non-reflected source (S_o) or with the remaining nine detector mirrors (S_i). As described in Section 4.6.1, the detector mirrors are covered and uncovered in various permutations to facilitate measuring S_o and S_i. The amount of scintillation which occurs between the mirror cover and the mirror, in the mirror itself plus that which is reflected from the mirror (S_s), is measured using pulse counting techniques (see Section 4.6.2). A simulation that reproduces the observed pulse counting spectrum is used to predict the contribution of pion production (S_π) to the signal. The detector signal (S_{tot}) is written as a sum of the above sources and the Čerenkov signal resulting from elastically backscattered electrons (S_c) as

$$S_{tot} = S_o + S_i + S_s + S_\pi + S_c. \tag{4.1}$$

The scintillation components S_o and S_i are measured during both high ($\sim$ 4 mA) and low ($\sim$ 1 μA) incident electron peak current conditions. The ratio (R_1) is defined as

$$\begin{aligned} R_1 &= R_1(S_o) + R_1(S_i) && (4.2)\\ &= \frac{S_o}{S_o + S_i + S_s + S_\pi + S_c} + \frac{S_i}{S_o + S_i + S_s + S_\pi + S_c}. && (4.3)\end{aligned}$$

The total detector signal may be written in terms of the ratio R_1 as

$$\begin{aligned} S_{tot} &= (1 + \frac{R_1}{1 - R_1})(S_s + S_\pi + S_c) && (4.4)\\ &= \frac{1}{1 - R_1}(S_s + S_\pi + S_c). && (4.5)\end{aligned}$$

Ratios are used to minimize systematic effects like detector efficiency.

The scintillation between the mirror and mirror cover as well as the scintillation from the passage of charged particles through the mirror is measured using mirror covers and coincidence techniques on the pulse counting data. The difference in yield between mirror cover on and off will measure the sum of S_s, S_π and S_c. A coincidence requirement on this difference will isolate the component S_s.

$$S_s = (Y_{off} - Y_{on}) - (Y_{off} - Y_{on})|_{coinc.}. \tag{4.6}$$

The ratio R_2 is then defined as

$$R_2 = \frac{S_s}{S_\pi + S_c} \tag{4.7}$$

allowing S_{tot} to be written as

$$S_{tot} = (\frac{1}{1 - R_1})(1 + R_2)(S_\pi + S_c) \tag{4.8}$$

The simulation described in section 4.2 is used to estimate the contribution of pion production (S_π) to the coincidence spectrum. The ratio R_3 is defined as

$$R_3 = \frac{S_\pi}{S_c} \tag{4.9}$$

and completes the description of the detector signal in terms of the Čerenkov signal as

$$S_{tot} = \frac{(1 + R_2)(1 + R_3)}{1 - R_1} S_c. \tag{4.10}$$

Table 4.6 lists the values of the above ratios as well as the contribution of Čerenkov radiation from elastically backscattered electrons to the measured detector signal.

Components of the integration signal are listed in Table 4.6. The Čerenkov detectors closest to the incident electrons and target (#5 and #6) observe a higher fraction of scintillation light than the detectors farthest away (#4 and #7). Scintillation light from the aluminum shutters was observed only in detectors #5 and #6.

Coeff	Detectors 1,3,8,10	Detectors 2,9	Detectors 4,7	Detectors 5,6
R_1 (S_o)	11.2 ± 0.15 %	13.9 ± 0.1 %	9.4 ± 0.1 %	12.6 ± 0.2%
R_1 (S_i)	6.6 ± 0.3%	8.7± 0.7%	15.3 ± 0.6%	3.7± 0.2%
R_2	8.4 ±0.6%	8.0±0.5%	6.4 ±0.4%	9.1 ±0.3%
R_3	4.2 ±2.5%	4.2 ±2.5%	4.2 ±2.5%	4.2 ±2.5%
$\frac{S_c}{S_{tot\ noc}}$	72.7±5.0%	68.7±6.9%	67.9±5.5%	73.6±4.8%
$\frac{S_c}{S_{tot\ wc}}$ [50]	78.3±4.0%	75.0±5.0%	74.6±4.2%	77.6±2.9%

Table 4.6: Components of the integration signal measured by the SAMPLE detector. The closed shutter contribution for detectors 5 and 6 has been corrected to account for the scintillation light generated when the shutter is closed. The ratio $\frac{S_c}{S_{tot\ noc}}$ represents the Čerenkov signal fraction before a lead curtain was installed (ie.: before run #3200) and the $\frac{S_c}{S_{tot\ wc}}$ is after the lead curtain.

4.8 Measured Differential Cross Section

Using the gain measurements from Table A.4 and the scintillation measurements in Table 4.6, the elastic cross-section may be calculated. The current output by each of the ten Čerenkov detectors is converted to a Voltage by an amplifier located within the PMT base (see Figure A.3) which was calibrated as yielding 10^4 Volts/amp. The current from each Čerenkov detector is measured by and ADC (one for each detector) that is calibrated using a charge pulser, the results of which are shown in Table 4.7. The number of backscattered electrons (BE) is determined using the Čerenkov radiation length ("L_{rad}" in Table 3.3) along with the radiator efficiency coefficient (C_γ=0.273 photons/electron/cm) and the PMT detector efficiency (ϵ_{PMT}=0.197) in the equation

$$\begin{aligned}
\#BE &= ADC(Chan) \times \frac{1}{C_{ADC}} \left(\frac{15 \times 10^{-6} Volts \bullet sec}{Chan}\right) \times \frac{1}{C_{preamp}} \left(\frac{coul}{Volt \bullet sec}\right) \\
\times \epsilon_{PMT} &\times \frac{1Ce}{1.6 \times 10^{-19} coul} \times \frac{1}{Gain} \left(\frac{1PE}{Ce}\right) \times C_\gamma \left(\frac{photons}{PE \bullet cm}\right) \times L_{rad}(cm). \quad (4.11)
\end{aligned}$$

The number of backscattered electrons resulting from elastic scattering is determined by multiplying BE using the appropriate scintillation value (S_c) from Table 4.6. The number of incident electrons is measured using an average of the toroid monitors TTG1 and TTG2. The ADC conversion coefficients for these devices is 4463.0 ± 15.1

Chan/15nC for TTG1 and 4671.3 ± 17.2 Chan/15nC for TTG2. The differential cross-section is then calculated by dividing the ratio of the backscattered electrons to incident electrons using the target density (1.69×10^{24} protons/cm^2) and the solid angle shown in Table 3.3 for each respective detector. The measured cross-section is shown in Figure 4.13 along with two curves which calculate the cross-section using the Rosenbluth formula (see Equation 2.8) for the incident beam energy of 200 MeV and the effective beam energy which accounts for energy loss due to bremsstrahlung production (see Section 4.2).

Det.	-V	C_{ADC}	Gain (10^5)	Y(PEs/nC)	$\left(\frac{d\sigma}{d\Omega}\right)_{\text{lab}}$ (nb/sr)
1	1328	4198.88 ± 18.56	7.39 ± 5.17	353.06	36.24 ± 19.21
2	1278	4296.56 ± 19.13	2.83 ± 0.92	584.86	39.90 ± 12.98
3	1303	4238.74 ± 19.20	6.99 ± 3.89	437.84	32.80 ± 18.26
4	1227	4277.69 ± 20.75	4.30 ± 1.90	787.74	56.94 ± 25.16
5	1258	4173.62 ± 18.73	6.33 ± 4.69	295.72	22.32 ± 14.03
6	1248	4201.12 ± 19.03	6.90 ± 3.42	272.67	20.58 ± 10.20
7	1218	4176.53 ± 19.42	5.93 ± 2.54	614.86	44.44 ± 19.03
8	1285	4221.89 ± 19.54	5.97 ± 4.50	551.45	41.32 ± 31.14
9	1242	4220.66 ± 29.64	6.21 ± 1.84	401.54	27.39 ± 8.26
10	1249	4168.90 ± 29.51	6.38 ± 0.77	556.25	41.68 ± 5.03

Table 4.7: Differential cross section and related calibration coefficients. The symbol "-V" represents the voltage applied to the PMT detector dynode chain. "Y" represents the shutter open minus shutter closed Čerenkov detector signal yield. The cross-section is found by scaling "Y" using the scintillation measurements, target density and detector solid angle.

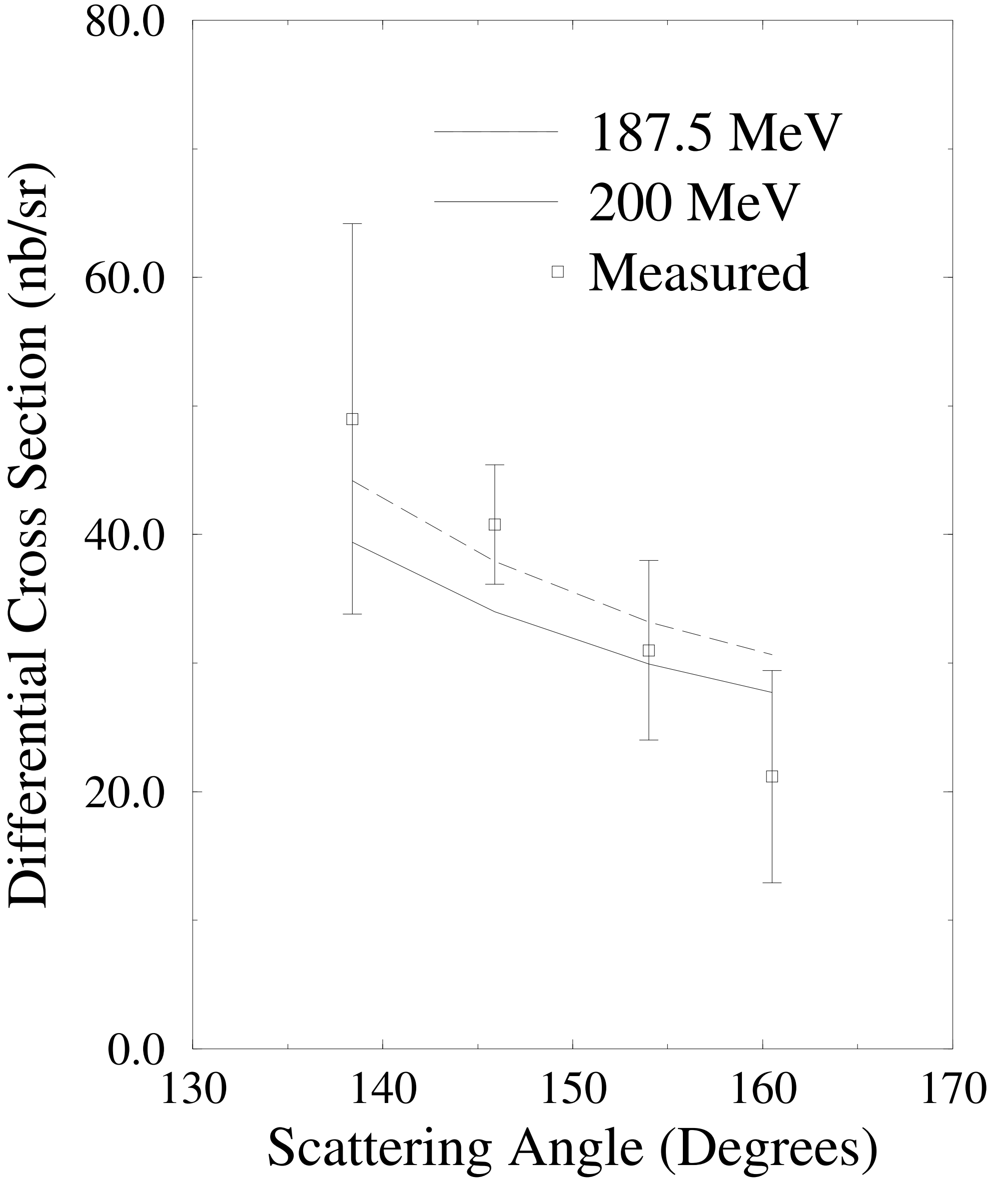

Figure 4.13: Measured cross section

Chapter 5

Experimental Uncertainties

This chapter discusses calculations made to determine the influence of several sources of statistical and systematic uncertainty in the experiment. Chapter 6 quantifies additional statistical and systematic uncertainties which have a larger impact on the measurement. One of the most important systematic uncertainties in parity-violation experiments is the contribution of false asymmetries to the measured asymmetry. Every effort is made to remove false asymmetries. The ^{12}C parity-violation experiment [44] was instrumental in providing an infrastructure for minimizing systematics which was used and extended during the SAMPLE experiment. In general, a false asymmetry is defined as an asymmetry (helicity-correlated effect on the yield) which is not related to parity-violation. One of the most important systematic uncertainty in these parity-violating experiments is the contribution from false asymmetries. One helicity-correlated feedback loop was used to minimize helicity-correlated intensity changes in the experiment. The analysis below quantifies or places limits on the false asymmetries that were investigated.

5.1 Polarized Electron Source

The polarized source is inherently the source of most helicity correlated effects because the electronic helicity signals are confined to the laser system. Helicity generation may contribute to the measured asymmetry in a direct manner. Other contributions due to couplings between the source and the accelerator, the target, and/or the detector are described in separate sections below. The contribution to the asymmetry uncertainty from pedestal generation and the labeling of helicity states at the polarized source is investigated in this section.

A μVAX III computer[52] located at the polarized source sets the electron helicity randomly for ten electron pulses ("timeslots"; see Figure 3.14) and then sets the next ten pulses to the complement helicity of the initial ten. This is done using a fast solid state switch to apply the voltage from two identical but opposite polarity Pockel's cell power supplies. Pedestals are generated at 20 Hz by failing to apply voltage to the shutter Pockel's cell. In the case that the intended pedestal pulse corresponds to a helicity compliment, the computer will wait to blank the next pulse in that timeslot.

False asymmetries related to the generation of pedestal events at the source are possible. Due to the limited number of pedestal events to data events (1/30), a pedestal asymmetry is more difficult to measure statistically during regular data acquisition. With the beam off however, statistically significant measurements may be made. This and previous experiments have reported[50, 44] that such measurements result in asymmetries consistent with zero. The detector pedestal asymmetry ($\equiv \frac{P^+-P^-}{P^++P^-}$) averaged to 0.151 ± 0.132 PPM. The toroid pedestal asymmetry ($\equiv \frac{W^+-W^-}{W^++W^-}$) measured simultaneously with the detector pedestal asymmetry above averaged to -.913 $\pm$ 0.966 PPM.

When analyzing data, however, this experiment and the C^{12} parity experiment [44] used helicity averaged pedestal events to calculate asymmetries. An asymmetry calculated using helicity averaged pedestals may be written as:

$$\begin{aligned}
A_{\overline{P^\pm}} &= \frac{\frac{S^+-(P^++P^-)/2}{T^+-(W^++W^-)/2} - \frac{S^--(P^++P^-)/2}{T^--(W^++W^-)/2}}{\frac{S^+-(P^++P^-)/2}{T^+-(W^++W^-)/2} + \frac{S^--(P^++P^-)/2}{T^--(W^++W^-)/2}} \\
&= \frac{\frac{S^+-P^+}{T^+-W^+} - \frac{S^--P^-}{T^--W^-}}{\frac{S^+-P^+}{T^+-W^+} + \frac{S^--P^-}{T^--W^-}} \times \left[\frac{2 + \frac{(P^+-P^-)(T^-+T^+-W^--W^+)-(W^+-W^-)(S^++S^--P^+-P^-)}{(S^+-P^+)(T^--W^-)-(S^--P^-)(T^+-W^+)}}{2 + \frac{(W^+-W^-)(S^+-S^--P^++P^-)+(P^+-P^-)(T^-+T^+)}{(S^+-P^+)(T^--W^-)+(S^--P^-)(T^+-W^+)}}\right] \\
&= A \times \left[\frac{2 + \frac{(P^+-P^-)(T^-+T^+-W^--W^+)-(W^+-W^-)(S^++S^--P^+-P^-)}{(S^+-P^+)(T^--W^-)-(S^--P^-)(T^+-W^+)}}{2 + \frac{(W^+-W^-)(S^+-S^--P^++P^-)+(P^+-P^-)(T^-+T^+)}{(S^+-P^+)(T^--W^-)+(S^--P^-)(T^+-W^+)}}\right]
\end{aligned}$$

The symbols S ($\sim$ 25000 channels) and T ($\sim$ 40000 channels) represent the ADC value of the integrated Čerenkov detector signal and incident electron current measured by a toroid, respectively. The symbols P ($\sim$ 8000 channels) and W ($\sim$ 6000 channels) represents a running average of the last ten pedestal events for the integrated Čerenkov signal and the incident electron current, respectively, when the incident electron current was essentially zero (i.e.: the electrical DC offset). The helicity of the incident electrons is denoted using superscripts $\pm$. The term in brackets above averaged to $[1 + (0.086 \pm 0.119)]$ using the same pedestal events used to calculate the asymmetry in the current data set. Therefore, in addition to the above checks, there is no evidence of pedestal asymmetries in the present data set.

Because the electron helicity is chosen before the electron is produced, false asymmetries may be introduced when labeling helicity or pedestal states during data acquisition by electronic crosstalk. Two steps were taken to avoid the transference of helicity information from the polarized electron source to the data recording medium. First, helicity information is sent to the data acquisition computer after signals from the previous event have been digitized in the ADC array and before signals for the next data event (corresponding to the helicity labels being sent) are generated. Secondly, helicity information for each event is sent along two TTL input lines to cancel possible electronics effects. Each event has two input lines which are either low and high or high and low respectively depending on the actual helicity state. Since the helicity labels are assigned randomly relative to the 60 Hz line frequency (see Figure 3.14), the two input lines will average out possible helicity correlations. The helicity-correlated differences due to crosstalk were found to contribute at the 10^{-8} level by the C^{12} parity-violation experiment[44].

One method to experimentally detect possible helicity-correlated problems involves defining an asymmetry in terms of the event position relative to the 60 Hz line frequency. The NEWWORD and COMPLEMENT labels (see Table 3.5) theoretically occur at the same place on the 60 Hz power line. Ideally positive and negative helicity states should both be distributed binomially between the NEWWORD and

COMPLEMENT labels. Defining an asymmetry A_{NC} (NC asymmetry) as the difference of the detector yield measured during a NEWWORD flag and the yield measured during the COMPLEMENT flag divided by their sum should essentially be similar to the asymmetry from unpolarized electrons and average to zero. Table 5.1 shows the two asymmetry calculation types using the events depicted in Figure 3.14.

Event #	Timeslot	Helicity	A	A_{NC}
1	1	+		
2	2	-		
3	3	+		
4	4	-		
5	5	-		
6	6	+		
7	7	+		
8	8	-		
9	9	+		
10	10	-		
11	1	-	$\frac{S_1^+-S_{11}^-}{S_1^++S_{11}^-}$	$\frac{S_1^+-S_{11}^-}{S_1^++S_{11}^-}$
12	2	+	$\frac{S_{12}^+-S_2^-}{S_2^-+S_{12}^+}$	$\frac{S_2^--S_{12}^+}{S_2^-+S_{12}^+}$
13	3	-	$\frac{S_3^+-S_{13}^-}{S_3^++S_{13}^-}$	$\frac{S_3^+-S_{13}^-}{S_3^++S_{13}^-}$
14	4	+	$\frac{S_{14}^+-S_4^-}{S_4^-+S_{14}^+}$	$\frac{S_4^--S_{14}^+}{S_4^-+S_{14}^+}$
15	5	+	$\frac{S_{15}^+-S_5^-}{S_5^-+S_{15}^+}$	$\frac{S_5^--S_{15}^+}{S_5^-+S_{15}^+}$
16	6	-	$\frac{S_6^+-S_{16}^-}{S_6^++S_{16}^-}$	$\frac{S_6^+-S_{16}^-}{S_6^++S_{16}^-}$
17	7	-	$\frac{S_7^+-S_{17}^-}{S_7^++S_{17}^-}$	$\frac{S_7^+-S_{17}^-}{S_7^++S_{17}^-}$
18	8	+	$\frac{S_{18}^+-S_8^-}{S_1^-+S_{18}^+}$	$\frac{S_8^--S_{18}^+}{S_8^-+S_{18}^+}$
19	9	-	$\frac{S_9^+-S_{19}^-}{S_9^++S_{19}^-}$	$\frac{S_9^+-S_{19}^-}{S_9^++S_{19}^-}$
20	10	+	$\frac{S_{20}^+-S_{10}^-}{S_{10}^++S_{20}^-}$	$\frac{S_{10}^--S_{20}^+}{S_{10}^-+S_{20}^+}$

Table 5.1: The standard (A) and NEWWORD/COMPLEMENT (A_{NC}) asymmetry calculation for the 20 arbitrary data events shown in Figure 3.14. The symbol S_E^h represents the detector signal (shutter open) measured at the arbitrary event # E for the incident electron helicity h.

The photodiode used to measure the output intensity of the Ti:Sapphire Laser during data acquisition has an asymmetry of A=.692 $\pm$ .469 PPM for the entire data set. An asymmetry calculation of the photodiode output using the above described NEWWORD/COMPLEMENT had an average value of A_{NC}=76.04 $\pm$ 0.44 PPM. Although such a large "NC asymmetry" is disturbing, a look at the photodiode asymmetry as a function of run number (time) (see Fig. 5.1) shows the data set taken in 1996 to be the dominant source of the large NC asymmetry. The average photodiode asymmetry for all runs taken in 1995 was 0.75 $\pm$ 0.65 PPM and the average NC asymmetry was A_{NC}=-2.72 $\pm$ 0.63 PPM. In 1996 the average asymmetry was 0.46 $\pm$ 0.34 PPM while A_{NC}=112.06 $\pm$ 0.31 PPM. Whereas the asymmetries from both years are one sigma from zero the NC asymmetries are quite different from zero. A 30 Hz chopper motor is the main reason for the large false asymmetries observed in 1996. During the first half of the 1996 data set a 30 Hz chopper motor was placed on the laser table at the polarized source. The large decrease in the asymmetry run to run variation around run number 3000 is the result of removing the chopper motor from the laser table. Because the helicities are chosen randomly, a non-zero value of A_{NC} does not directly impact the data - see Section 5.6.

5.2 Accelerator

False asymmetries may also appear due to couplings between the polarized source and the linear accelerator itself. In this case the coupling is due to beam loading (see Section 3.3) wherein helicity-correlated beam intensity variations are converted into helicity-correlated beam energy variations. [1]

The PITA (polarization induced transport asymmetry) feedback system[44] has been shown to control beam intensity fluctuations correlated with electron helicity to within several parts in 10^6 on a time scale of 30 minutes. This false asymmetry is an artifact of the coupling between the transmission of laser light to the crystal

[1]Using the thermionic electron source with the polarized source electronics running, the asymmetry was found to be consistent with zero indicating the absence of direct coupling between the polarized source electronics and the beam.

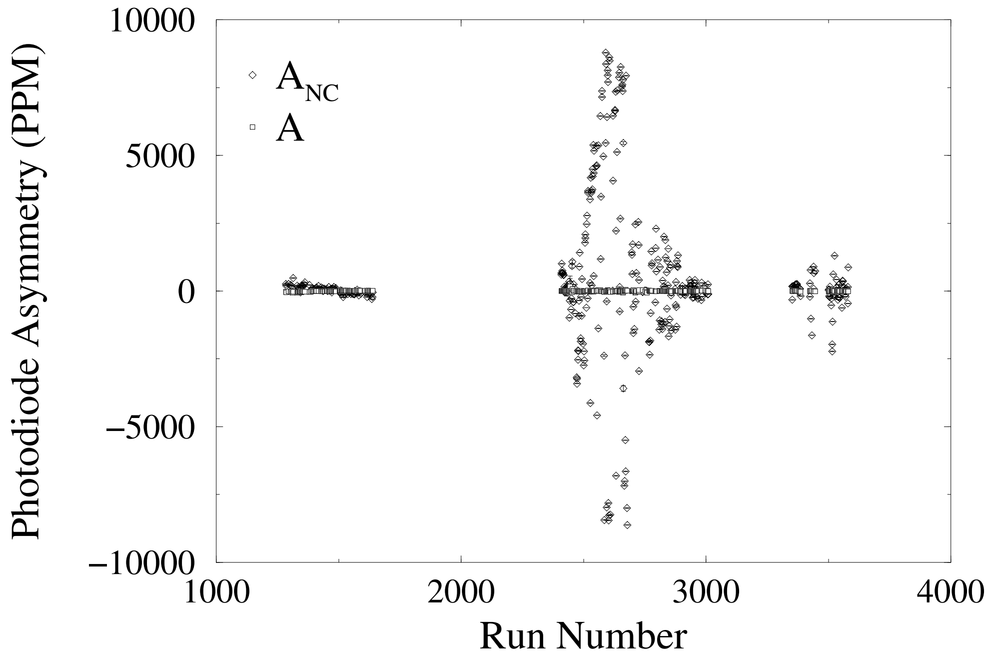

Figure 5.1: The asymmetry of a photodiode measuring the output of the Ti:Sapphire laser. Both the defined asymmetry and a "False Asymmetry" are superimposed.

for different handedness of imperfect circular polarization. Although referred to as circularly polarized light, the incident laser light polarization is actually elliptical. The transmission efficiency of this light through the optics line differs depending on the orientation of the linear components of the elliptically polarized light. These small linear components change when the helicity of the light is reversed by the Pockel's cell. As discussed in reference [44] the feedback system looks at the electron beam current at the final accelerator stage (AT5: "accelerator toroid 5") and slightly adjusts the polarization at the helicity Pockel's cell via a small d.c. offset to the high voltage. The d.c. amplitude is adjusted every 3 minutes according to the asymmetry measured at the beam current monitor AT5. Table 5.2 lists the average beam current asymmetry measured just before the LH_2 target as 0.84 ± 0.29 PPM using all the data analyzed in this thesis.

It was observed at the polarized source that changing the laser light polarization with the electric field applied across a Pockel's cell can alter the angle and/or exit point of the light passing through the Pockel's cell on its way to the GaAs crystal. This helicity-correlated laser beam motion is the cause of helicity-correlated electron beam motion ($\sim$ hundreds of nm) measured at four monitors located just before the LH_2 target in the North Hall (see Table 5.2). These position differences generated false asymmetries in the experiment because the background levels were correlated with the incident electron beam position. The impact of the position asymmetries on the measurement is removed by correcting the detector signal on a pulse-by-pulse basis (see Section 6.3.1).

Device	Property	Measured Asymmetries/Pulse Pair difference
AT5	Current	-1.40 $\pm$ 0.46 PPM
TTG1	Current	0.76 $\pm$ 0.28 PPM
TTG2	Current	0.84 $\pm$ 0.29 PPM
ECSX	Energy	-4.00 $\pm$ 7.31 eV
NH1X	Horiz. Position	-5.93 $\pm$ 0.63 $\times 10^{-5}$ mm
NH2X	Horiz. Position	-7.89 $\pm$ 0.71 $\times 10^{-5}$ mm
NH1Y	Vert. Position	-1.86 $\pm$ 0.31 $\times 10^{-5}$ mm
NH2Y	Vert. Position	-2.56 $\pm$ 0.37 $\times 10^{-5}$ mm

Table 5.2: Properties of the incident electrons as measured with the present data set.

The incident beam energy contributes a false asymmetry which may be calculated using the energy dependence of the cross-section shown in Equation 2.9. The derivative of Equation 2.9 with respect to energy is given by

$$\frac{\partial \frac{d\sigma}{d\Omega}}{\partial E} = -\frac{d\sigma}{d\Omega}\left(\frac{2}{E} + \frac{2\sin^2(\theta/2)}{M + 2E\sin^2(\theta/2)}\right) \tag{5.1}$$

The false asymmetry induced by energy difference shown in Table 5.2, consistent with zero, is

$$A_{false} = \frac{\Delta \frac{d\sigma}{d\Omega}}{2\frac{d\sigma}{d\Omega}} = -\frac{\Delta E}{2}\left(\frac{2}{E} + \frac{2\sin^2(\theta/2)}{M + 2E\sin^2(\theta/2)}\right) = (4.59 \pm 8.38) \times 10^{-8} \tag{5.2}$$

and does not contribute significantly to the asymmetry measured in the experiment.

5.3 Liquid Hydrogen Target

The target cell window thickness and mismatch between the entrance and exit window are other possible sources of a false asymmetry. This false asymmetry is a result of helicity-correlated changes in the position of the incident electrons on the face of the target. One key ingredient to the target design is to maintain a constant target length (distance the electron travels through the target) while allowing for position fluctuations. The aluminum containment vessel for the target is constructed using entrance and exit windows with equal radii of curvature (see Figure 3.10. The length of the target cell would change if the window radii were different by the amount

$$\delta L = \left(\frac{1}{R_1} - \frac{1}{R_2}\right) x\delta x \tag{5.3}$$

where R_1 and R_2 are the window radii of curvature and x is the amount the beam is offset from the center. For an offset of 0.1 cm and a 10% mismatch in the 8 cm exit windows radius, the relative target length would change by $\delta L = -8.97 \times 10^{-7}$ mm using the largest measured position difference of -7.89 $\times 10^{-5}$ mm from Table 5.2. Since the detector signal is directly proportional to the target length, the induced false asymmetry is

$$A_{false} = \frac{\delta L}{2L} = \frac{-8.97 \times 10^{-7}\ mm}{2 * 400\ mm} = -1.12 \times 10^{-9} \tag{5.4}$$

A similar calculation to determine the effects of non-uniformities in the aluminum window thickness (t_W) gives a window length change of $\delta t_W = x\delta x / R = 9.86 \times 10^{-7}$ mm using the 0.1 cm offset for x above and the value of -7.89 $\times 10^{-5}$ mm.

$$A_{false} = \frac{\delta t_W}{2L} = \frac{-9.86 \times 10^{-7}\ mm}{2 * 400\ mm} = -1.23 \times 10^{-9} \tag{5.5}$$

These false asymmetries are not significant compared to the expected asymmetry of 10^{-6}.

Data was taken during commissioning of the target and detector at several different beam current levels to check for changes in the target length of a random nature that would result from target boiling. increased in 4μA intervals by turning timeslots on uniformly with respect to the 60 Hz line frequency (see Figure 3.14). Under the assumption that any systematic increase in the width of the asymmetry distribution Σ measured with the detector is due to a fluctuation in the target length $\frac{\Delta L}{L}$, the change in Σ for the data taken in 1994 would correspond to a $\sim 0.1\%$ contribution for a single beam pulse from target length fluctuations at beam currents of 40 μA. Since the statistical precision of the detector signal is about 0.5%, fluctuations in target length at this level are not significant.

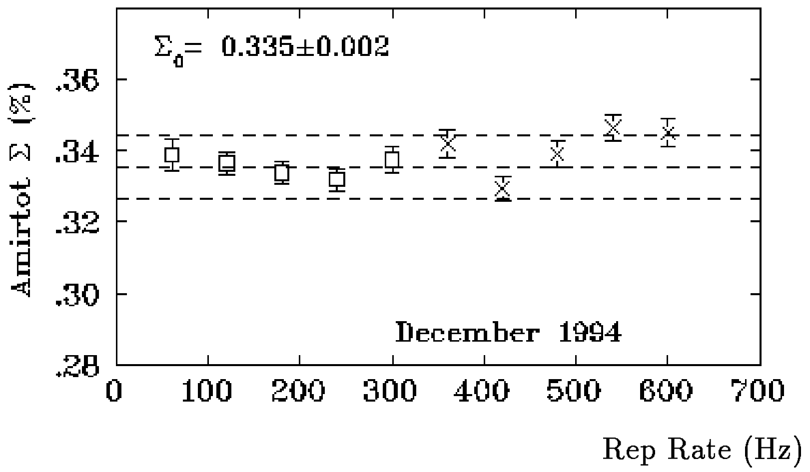

Figure 5.2: Asymmetry distribution width as a function of beam current (4μA/60Hz)

5.4 Transverse Polarization

The amount of transverse polarization will systematically influence the asymmetry measured by each of the ten individual Čerenkov detectors. A system of ten detectors with reflection symmetry and an incident electron spin that is not purely longitudinal will have a measured Mott asymmetry (A_{Mott}) in each detector that may be removed by averaging the asymmetry from all 10 detectors. Under the assumption that the detector is not reflection symmetric, it would be desirable to measure a Mott asymmetry and see the asymmetry change sign between two "left-right" symmetric detectors to test this principle. Measurements were taken with the spin aligned transversely that averaged to a Mott asymmetry of -2.4 $\pm$ 1.3 PPM, however the measured raw asymmetry failed to change sign when the "slow helicity reversal" half wave plate was rotated making the measurement suspect.

The Mott asymmetry ($A^{1/2}_{Mott}$) for a spin 1/2 target has not been theoretically calculated at this time. The Mott asymmetry (A_{Mott}) [53] for a spin zero target may be written as

$$A_{Mott} = -\frac{\alpha^3 m_e c^4 \hbar^2}{E^3 \sigma_{Mott}} csc(\theta) ln(csc(\theta/2)) \text{ [53]} \tag{5.6}$$

where θ is the backscattering electron angle, E is the incident electron energy, and $\hbar$, c, and m_e are the usual constants from Reference [22]. The impact of the spin 1/2 Mott asymmetry ($A^{1/2}_{Mott}$) is estimated by replacing the Mott cross-section (σ_{Mott}) with the proton cross-section (σ_p) in Equation 5.6.

$$A^{1/2}_{Mott} = -\frac{\alpha^3 m_e c^4 \hbar^2}{E^3 \sigma_p} csc(\theta) ln(csc(\theta/2)) \tag{5.7}$$

Equation 5.7 predicts an asymmetry of $\sim$-22 PPM at the mean scattering angle of the detector. This asymmetry becomes -4.2 PPM after being diluted with the measured polarization and signal-to-background and is comparable to the measured value of -2.4 $\pm$ 1.3 PPM.

The contribution of the transverse polarization to the asymmetry measured using all 10 detectors may be estimated once limits are placed on the magnitude of the transverse spin components and the detector symmetry which if less than unity would allow contributions from the Mott asymmetry. The Mott Asymmetry of -2.4 assumes complete transverse polarization. The measured components of the incident electron polarization for the parity-violation data set used in this thesis are shown in Table 5.3. Using the maximum observed component of 0.13 and assuming the detector is symmetric to the 95% level, the contribution of a Mott asymmetry from transverse polarization to the measured asymmetry can be restricted to

$$A_{false} \leq (-2.4 \pm 1.3 PPM) \times 0.13 \times 0.05 \tag{5.8}$$

$$\leq -0.02 \pm 0.01 PPM \tag{5.9}$$

$$(5.10)$$

Component	1280-1360(1995)	2000-3200(1996)	3200-3600(1996)
$\lvert\mathbf{P_X}\rvert/\lvert\mathbf{P_B}\rvert$	0.05 ± 0.12	0.02 ± 0.03	0.00 ± 0.03
$\lvert\mathbf{P_Y}\rvert/\lvert\mathbf{P_B}\rvert$	0.00 ± 0.17	0.13 ± 0.03	0.00 ± 0.03
$\lvert\mathbf{P_Z}\rvert/\lvert\mathbf{P_B}\rvert$	0.99 ± 0.01	0.99 ± 0.01	0.99 ± 0.01

Table 5.3: Components of the incident electron polarization [50].

5.5 Detector

As an example of false asymmetries associated with the detector, consider a PMT which responds to light in a non-linear fashion. If there are helicity-correlated changes in the beam current, the normalized yield in the detector would also change in a helicity-correlated manner (because of its non-linear response) producing the false asymmetry. The PITA feedback has been able to control helicity-correlated changes in the incident beam to the 10^{-6} (see Table 5.2) level. Even if the incident current changes in a helicity-correlated manner by 10^{-5}, then the detector signal S would change by 10^{-5} as well if the detector were linear and the normalized detector yield ($N = \frac{S}{T}$) would be unchanged. If the detector is nonlinear by 1% such that the expected change in the detector signal S is 1% less than expected, then the induced false asymmetry would be

$$A_{false} = \frac{\frac{N^+}{T^+} - \frac{N^-}{T^-}}{\frac{N^+}{T^+} + \frac{N^-}{T^-}} \tag{5.11}$$

$$= \frac{\frac{N}{T}(1 - \frac{1-10^{-5}-10^{-7}}{1-10^{-5}})}{\frac{N}{T}(1 + \frac{1-10^{-5}-10^{-7}}{1-10^{-5}})} \tag{5.12}$$

$$= \frac{10^{-7}}{2} \tag{5.13}$$

The tube manufacturer specifies that for PMT anode currents three orders of magnitude higher than that expected in this experiment the non-linearity will be about

5%. This places false asymmetries due to a non-linear PMT well below the level being measured.

Another area in which a false asymmetry may arise involves the scattering angle of the electron. If there are helicity correlated changes in the scattering angle (θ) due to helicity-correlated changes in the incident beam direction, the measured cross section would also change resulting in a false asymmetry. Using the Rosenbluth formula (Equation 2.8), the derivative of the differential cross-section ($\frac{d\sigma}{d\Omega}$) with respect to the backscattering angle θ is shown in Figure 5.3. The largest rate of change in $\frac{d\sigma}{d\Omega}$ (-1.32 nb/sr/degree) occurs at the smallest detector backscattering angle of 138.4^o. Table 6.2 reports an average helicity correlated monitor difference of -35 nm for the entire data set. Since the distance between these two position monitors was 4 m, the angular difference becomes -8.75 $\times$ 10^{-9} radians. The false asymmetry from this helicity-correlated angular difference is

$$A_{false} = \frac{\Delta\sigma}{2\sigma} \tag{5.14}$$

$$= \frac{-1.32(-8.75 \times 10^{-9})}{2 \times 40} \tag{5.15}$$

$$= 1.44 \times 10^{-10}. \tag{5.16}$$

and does not contribute significantly to the measured asymmetry.

5.6 Electronics/Data Acquisition

The final area considered involves the process of recording the data taken. This encompasses everything from the cables used to carry the relevant signals, the electronics used to digitize the signals, and the data analysis used to calculate the physics result. The interplay between the above processes is by no means trivial. There were however several attributes of these processes which were examined to estimate the contribution to the overall systematic uncertainty.

The 16 bit ADCs used to digitize the photo-multiplier output have a maximum input of 5 Volts and are known to be differentially non-linear and thus can generate

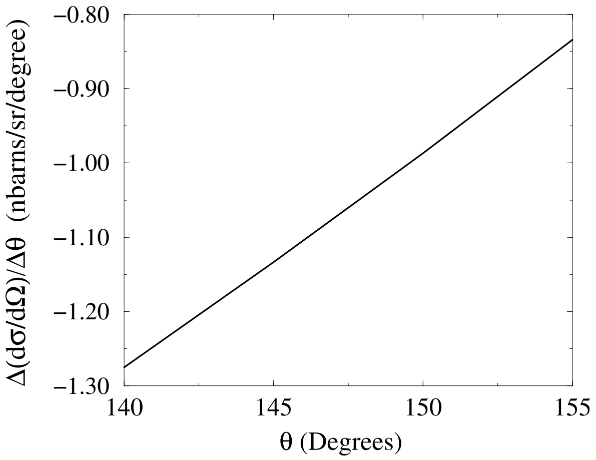

Figure 5.3: Angular dependence of differential cross-section $\frac{d\sigma}{d\Omega}$ as of function of the detector angle.

a false asymmetry. Looking at the ADC as a simple voltage divider network made from resistors, it can be seen that if one of the resistors goes to zero resistance then two digitized voltage values which would normally be resolved by the voltage divider network will be read as the same voltage. This can be experimentally observed by injecting the ADCs using a voltage source. If by chance the centroid of the detector output ($N^{\pm}$) were to straddle the point of non-linearity in the ADC, then a false asymmetry would change the ideal asymmetry ($A_o \equiv \frac{N^+-N^-}{N^++N^-}$). If the ADC deviates from a linear response by S channels while measuring a signal of width σ, the contribution of differential nonlinearity to the asymmetry uncertainty is less than

$$A_{measured} = \frac{(N^+ - S) - (N^- + S)}{(N^+ - S) + (N^- + S)} \tag{5.17}$$

$$= \frac{N^+ - N^-}{N^+ + N^-} - \frac{2S}{N^+ + N^-} \tag{5.18}$$

$$= A_o - \frac{2S}{N^+ + N^-} \tag{5.19}$$

$$\frac{\Delta A}{A} = \frac{A_{measured} - A_o}{A_o} \tag{5.20}$$

$$= \frac{-2S}{N^+ - N^-} \tag{5.21}$$

$$= \frac{-2S}{\sqrt{2\pi}\sigma}\ [54]. \tag{5.22}$$

By constraining the non-linearity of the ADC response to 10 channels (S=10) and with a typical width of σ=300 channels, ADC differential non-linearity would contribute 2.7% to the systematic uncertainty of the measured asymmetry. This contribution is reduced ten fold by injecting a d.c. offset (set randomly for each pulse) into the ADC and then removed the d.c. offset in software using the calibrated ADC response to the d.c. input.

The contribution of noise to the integrated signal and hence the statistical precision of the asymmetry has been analyzed. Consider a signal level (S) which contains noise of frequency (ν) and amplitude (a) (depicted in Figure 5.4a). Under ideal conditions with no parity-violation the asymmetry would be written as

$$A_{noise} = \frac{(S - a\sin[2\pi\nu t]) - (S - a\sin[2\pi\nu(t+\Delta)])}{(S - a\sin[2\pi\nu t]) + (S - a\sin[2\pi\nu(t+\Delta)])} \tag{5.23}$$

$$= \frac{\frac{a}{S}(\sin[2\pi\nu(t+\Delta)] - \sin[2\pi\nu t])}{(2 - \frac{a}{S}(\sin[2\pi\nu t]) + \sin[2\pi\nu(t+\Delta)])} \tag{5.24}$$

The symbol Δ represents the time shift to the compliment pulse (1/60 sec). The uncertainty in A_{noise} when the noise amplitude (a) is constant can be expressed as

$$\delta A^2_{noise} = \left(\frac{\partial A_{noise}}{\partial S}\right)^2 (\delta S)^2 \tag{5.25}$$

$$= 4\left(\frac{a}{S}\right)^2 \left(\frac{\delta S}{S}\right)^2 \frac{(\sin[2\pi\nu(t+\Delta)] - \sin[2\pi\nu t])^2}{(2 - \frac{a}{S}(\sin[2\pi\nu t]) + \sin[2\pi\nu(t+\Delta)])^2} \tag{5.26}$$

Consider an ideal example of this noise for the case of only one timeslot and a noise of frequency (ν =30 Hz) that is in phase with the data sampling rate. The asymmetry measured by a single set of pulse-pairs taken at time (t+ Δ =3/120 sec) and at time (t=1/120 sec) would result in $A_{noise} = \frac{a}{S}$. Repeating this measurement using the random helicity labeling scheme outlined in Figure 3.14 would result in measurements of the same magnitude that change with respect to the helicity state. In the case that there were the same number of positive helicity states as negative helicity states the measured asymmetry would be zero, otherwise one would expect to measure an asymmetry with the magnitude and uncertainty

$$|A| = \frac{a}{S} \pm \left(\frac{a\delta S}{S^2}\right). \tag{5.27}$$

A direct measurement of the noise asymmetry A_{noise} can be done using the NEWWORD/COMPLIMENT asymmetry (A_{NC}) as outlined in Table 5.1 since the NEWWORD and COMPLIMENT flags would be in phase with the 30 HZ noise.

$$A_{NC} = \frac{a}{S} \pm \left(\frac{a\delta S}{S^2}\right). \tag{5.28}$$

The asymmetry A_{NC} can be used to measure the noise level $\frac{a}{S}$ in the experiment and place limits on the contribution of that noise to the measured helicity-correlated asymmetry A. Using the measured detector signal relative error $\frac{\delta S}{S} = \frac{1}{200}$ and the largest observed A_{NC}=200 PPM, the noise contribution to the uncertainty in the asymmetry would be 1 PPM, under the extreme assumptions of this simple example.

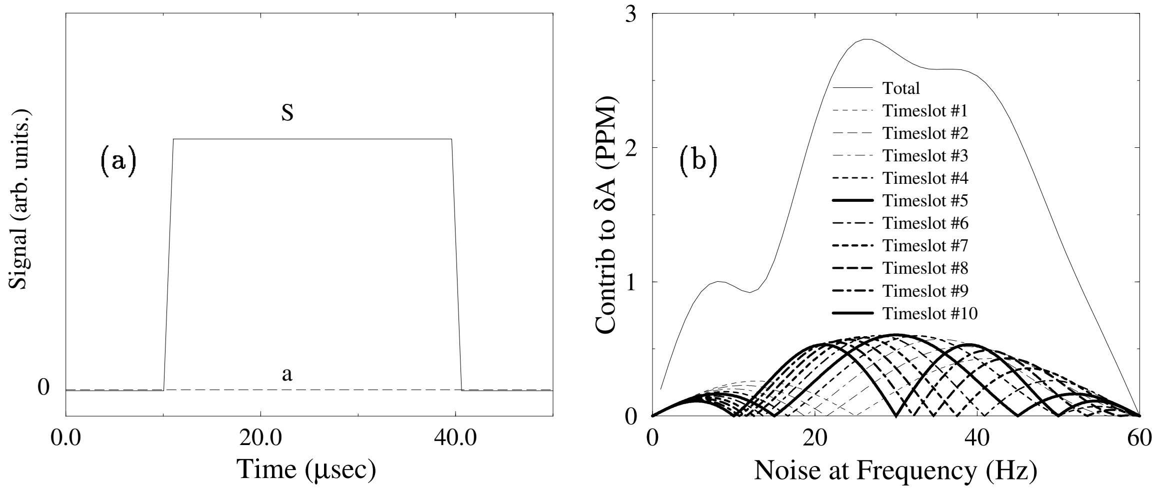

Figure 5.4: a.) The timing spectrum of the measured signal and the arbitrary noise in arbitrary units. b.)contribution of noise to the uncertainty for the first 10 events

The above model was further refined to account for the ten timeslots and the averaging of the asymmetry measured in each of those timeslots. Figure 5.4b contains a graph of the contribution to the asymmetry uncertainty from each timeslot and resulting total contribution for frequencies below 60 Hz using a single event from each timeslot and assuming $\frac{a}{S}$=200$\times$10^{-6} which corresponds to the largest false asymmetry (A_{NC}) measured in the experiment. A simplistic picture would expect the maximum contribution of noise to the asymmetry uncertainty at 30 Hz and in phase with the helicity generation. In practice, however, averaging over 10 timeslots shifts the maximum away from 30 Hz towards 27 Hz for the arbitrary phase chosen in this simulation. Propagating this effect through 10^5 measurements of the asymmetry (corresponding to a typical mini-run) yields an increase in the asymmetry uncertainty (δA) as depicted in Figure 5.5 for of an asymmetry centered at zero and having a variance of 100 PPM (A =0.03 PPM without noise). As expected several harmonics of the fundamental frequency are visible. Under ideal conditions, fortunately, noise doesn't have a dominant frequency and this model is an extreme case. Using the present data set, A_{NC} of the Čerenkov detector was measured to be -0.95 $\pm$ 0.24 PPM which at the frequency of 29 Hz (corresponding to the largest contribution) would increase the asymmetry uncertainty by 1% (Figure 5.5 assumed an asymmetry A_{NC} of 200 PPM and found a contribution of 200% at 29 Hz).

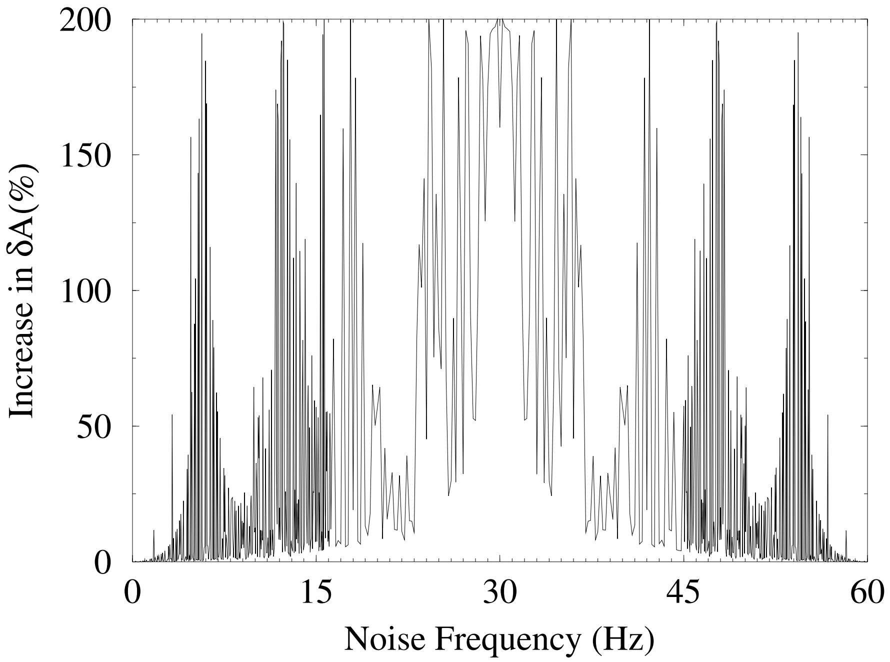

Figure 5.5: Increase in the Asymmetry uncertainty bar due to various noise frequencies when propagated over a data sample of 10^6 events

This model may be used to explain one unsolved mystery which involves the appearance of symmetric satellite peaks in the pulse difference histograms of some beam current monitors. The satellite peaks in those histograms are reproduced by assuming the existence of either 29 or 31 Hz dominant noise (see Fig. 5.6). Histograms with this structure were seen intermittently during the experiment.

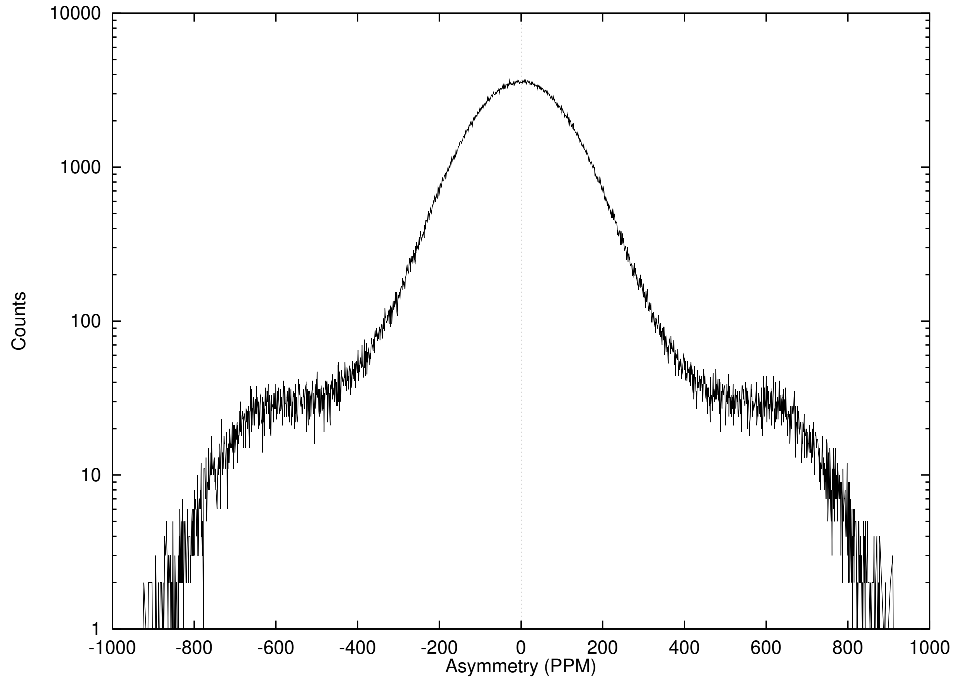

Figure 5.6: Spurious anomalous satellite peaks on beam current monitors reproduced using the noise simulation described within section 5.6

A final test of the entire DAQ system was done by inserting light emitting diodes (LEDs) into the detector to simulate the Čerenkov radiation emitted by a backscattered electron. The presence of other experimental halls at MIT-Bates made it possible to simulate running conditions by taking data with LEDs while the accelerator was running for other experiments. A charge pulser was used to inject a charge into the north hall toroids in order to generate a "fake" beam current. The LED output was adjusted to match the expected Čerenkov signal. Figure 5.7 shows the asymmetry measured using the LEDs as $A_{LED} = 0.53 \pm 0.39 \times 10^{-6}$. [2] The measurements of zero using LEDs and thermionic beam are solid checks of many parts of the overall system for systematic effects that would influence the parity-violation measurements.

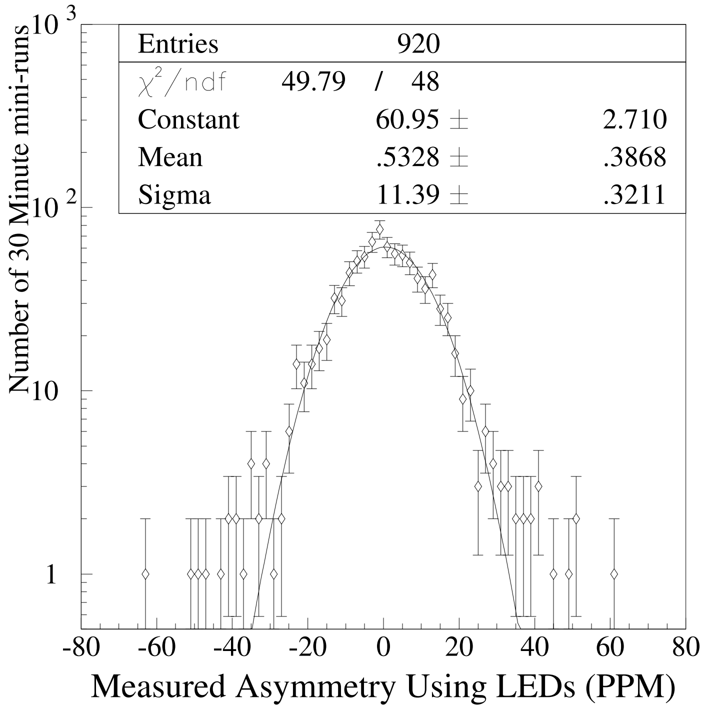

Figure 5.7: The measured Asymmetry using LED's in the SAMPLE detector.

[2] Appendix B describes the correlations induced in the asymmetry calculation due to the fact that all ten detectors share the same incident beam current and that at least 30 events share the same pedestal. This correlation correction increases the asymmetry uncertainty by a factor of 1.62 making the LED asymmetry consistent with zero. This large correlation, due mostly to the large toroid pedestal width, was reduced to ≈ 1.16 before taking asymmetry data with LH_2.

Chapter 6

Data Analysis

The analysis of the SAMPLE data set includes investigating not only the physics asymmetry but also calculating possible false asymmetries involving pedestal events and helicity labeling as well as correcting the asymmetry for helicity-correlated beam properties. The sources of "false asymmetries" in the experiment are investigated in Chapter 5. In this chapter the corrected asymmetries are determined.

6.1 Data Integrity Tests

In order to reach the asymmetry calculation stage of the analysis, data events must pass two levels of scrutiny. The first level involves several checks on the raw data for event type consistency with event identification. The next level tests several properties of the incident electrons to insure low background and high quality signal. The latter tests were checked to determine if the removed events changed the value of the measured asymmetry.

The first level of testing eliminates the end results of intermittent hardware errors or limitations. Computer dead time, ADC conversion failures and other unsolved intermittent problems cause disruptions in the data stream and result in either missing or mislabeled events. Event scalers are used to chronologically label each data event making it possible to detect this interruption in the data stream. One scaler labels each event with a unique 24 bit integer and another scaler labels each event with a timeslot value (1-10) representing the event's position in time along the 60 Hz line cycle (see Figure 3.14). Events with timeslots labeled other than 1 through 10 inclusive are discarded as are pulse pair candidates (identified in the event stream in Table 3.5 with the NEWWORD/COMPLIMENT flag) not separated by exactly 10 events. This problem of "skipped" events occurs about .03% of the time and requires removing the event which immediately follows in order to ensure all event labels were set properly. Even with this constraint, about 0.1% of the events failed to be labeled correctly as pedestal (signal) events when the ADC amplitude was consistent with a pedestal (signal) event. These events were removed by requiring toroid and mirror pedestal events to have ADC values less than 10,000 channels while signal events are required to have values larger than 10,000 channels. The final first level cut required the PITA feedback DAC level be in a range indicating it was functioning properly.

The second level of data integrity tests places requirements on the incident electron energy, a background detector signal, the accelerator current transmission, and the incident electron position just before the LH_2 target. The energy position monitor (ECSX) and the halo monitor (SHALO) located near the detector entrance were used to remove measurements with high background levels. Beam loss measured as the ratio of two electron current monitors also helped to minimize background levels. The electron current lost between the accelerator and just before the LH_2 target (AT5/TTG2) is restricted to less than 1% of the mean electron current. A ratio of the last two beam current monitors (TTG1/TTG2) was also constrained to the 1% level. Beam position monitors (NNH1X, NNH2X, NNH1Y, and NNH2Y) were also used to test data integrity but the nominal requirements typically did not remove any events.

The data tests above are independent of the incident electron helicity and are not expected to influence the final result. The data was analyzed using 243 (3^5) different permutations based on three possible values for five cuts (two transmission currents, two extrema of the ECSX monitor, and the SHALO tail) to determine if helicity information was indirectly influencing monitors used for data integrity tests. Although the uncertainty increases due to the statistical effect of removing data with

Level	Problem	% discarded
1	skipped events	0.3
1	mislabeled	0.1
2	NTTG1/AT5<0.9	0.2
2	NTTG1/NTTG2>1.05	1.4
2	PITA LOW	4.0
2	PITA HIGH	1.9
2	ECSX High	3.4
2	ECSX Low	0.2
	# of Raw Events	370,332,524
	# of Accepted Events	300,598,382

Table 6.1: Discarded events.

more conservative cuts, a pronounced change in the value of the asymmetry based on one of the above cuts would be difficult to argue (see Figure 6.1).

The three noticeable shifts in Figure 6.1 were found to coincide with tests on the high energy side of the ECSX monitor. During data taking, slits in the ECS system were set to remove electrons having an energy 0.3% below 200 MeV and 0.5% above 200 MeV. The data analyzed in this thesis placed software cuts on the ECSX monitor which removed electrons having an energy above 0.45% of 200 MeV since a beam position beyond that point would have a profile that would begin scraping on the 0.5% collimator slit. The dependence of this software cut on the asymmetry was investigated by measuring the uncorrected asymmetry that results when the 0.45% cut is changed to more constraining value of 0.35% and 0.25%. Permutation #81 in Figure 6.1 corresponds to constraining the beam energy at the ECSX to 0.35% while permutation # 163 reflects the asymmetry measured using a 0.25% ECSX cut. The shift occurring at permutation # 30 is due to a low energy ECSX cut of -0.15% compared to the typical value of -0.25% used. A shift in the spectrum was not seen when the low energy ECSX cut was set to -0.1%.

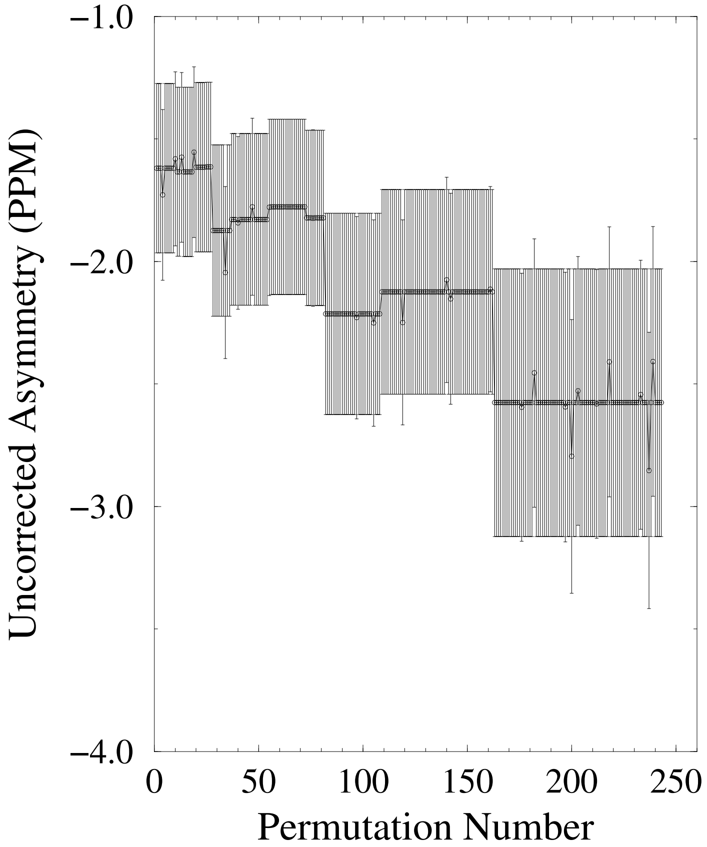

Figure 6.1: The uncorrected asymmetry as a function of cut permutation.

6.2 Differences with previous analyses

Presently three analysis programs exist to process the SAMPLE data set. The first package is based on the ^{12}C parity-violation experiment [44] and processes data online using the "Q" data analysis package [57]. The "Q" package was not available for the computer platforms used to analyze data at Caltech or Illinois. This spawned the creation of two independent analysis packages at the different institutions. The Caltech package in its standard form is more closely related to the "Q" package except that it outputs an asymmetry based on the linear sum of all ten detectors and timeslots while the "Q" analysis outputs asymmetries for each of the 10 detectors and 10 timeslots.

The analysis package developed at Illinois approached the calculation using a parallel "pulse-pair" structure and not the serial method of the previous two analyzers. Instead of keeping a matrix of only the NEWWORD data elements, an array of 200 elements containing 10 timeslots, 10 detectors, and both helicity states was filled and then calculations performed. This allowed evaluating all events within the 30 Hz time frame instead of just the most recent event. Similar to the "Q" package, summary files were written containing information for each timeslot and detector. Other packages were then used to parse the summary files and perform weighted averages over timeslots and detectors when desired.

The Illinois analysis package was meticulously compared with the "Q" package until exact agreement was achieved by correcting mistakes in both packages. The most notable mistake in the "Q" analysis package was the unnecessary removal of events in timeslot 1 due to the failure of resetting a counter when timeslot 9 events were missing from the data stream. If a timeslot was missing from the data stream the next event would be flagged as bad. If events in timeslot 10 were flagged bad because timeslot 9 was missing, an event counter would not be reset resulting in the unnecessary removal of the next event in timeslot 1. The Illinois and the "Q" analysis package had identical results when the above mistake was removed from the "Q" package.

A comparison was also made between the Illinois and Caltech analysis packages. The Caltech analysis throws away more initial events than either the "Q" or Illinois package because it waits for all 10 timeslots to have a full pedestal ring [1] before it begins to analyze data (only .01% of the data is thrown away). The DAC slope fit, in the Caltech analysis, will have the first event initialized to zero and bias one of the fits for a single timeslot. Fortunately the 1,000 other events keep this from becoming a serious problem. The Caltech analysis suffers from roundoff errors when normalized data, the result of dividing two 16 bit integers, is saved as a single precision real then equated to a double precision real. The randomness of the process doesn't change the

[1] A pedestal ring contains the average of the 10 most recent pedestal events. The detector signal is decreased by this average.

final centroid but in more than one data set it was observed to increase the uncertainty by 3%. While the above problems should be corrected, their effects on the present data set do not prevent comparisons.

The Caltech and Illinois analysis make corrections to the detector signal using the same method described in Section 6.3.1. The Caltech analysis package performs linear corrections on both the equally weighted sum of all 10 detectors and individual detectors while the Illinois analysis makes corrections up to a fourth order Legendre polynomial to each individual detector in each of the 10 timeslots . Figure 6.2d shows a non-linear detector response (using an equally weighted sum of all 10 detectors) to fluctuations in the horizontal beam position parameter (XTARG) for typical 30 minute mini-run. In this example, the Caltech analysis would fit the timeslot average response (solid circles) and make corrections to the detector signal using a line which has a different slope than a linear fit to the response from the same detector measured in each individual timeslot due to the different incident electron position in each timeslot which results in a different detector response. One analysis [50] reported, using the Caltech package, to have found no difference between an asymmetry calculated performing a weighted average of the asymmetry from individually corrected mirrors as compared to an asymmetry calculated using the corrected linear sum of all ten mirrors. However, a shallower slope calculated in this analysis translates into a smaller contribution of the correction to the uncertainty in the measured asymmetry. Figure 6.3 shows individual detector response to several monitors as observed in an individual timeslot using the same data set used for Figure 6.2d. The response after applying corrections is also shown using the Illinois analysis. Beam corrections applied to individual detectors in separate timeslots can decrease the contribution of the correction to the uncertainty in the measured asymmetry.

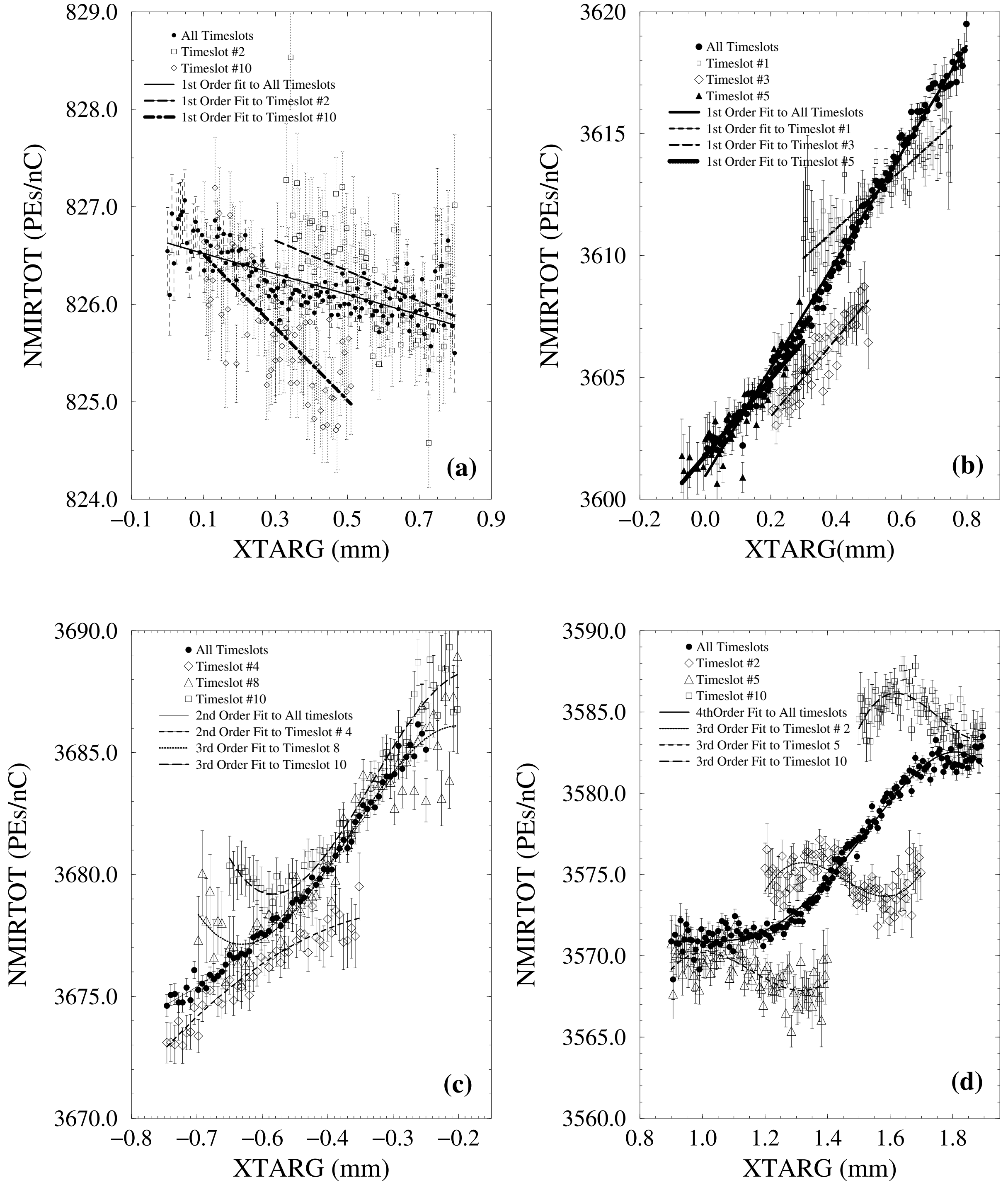

Figure 6.2: The SAMPLE detector response from an equal weighted sum over all ten detectors (NMIRTOT) as a function of the same incident horizontal beam parameter (XTARG) observed in four different data sets (Runs 2649, 1468, 2494, and 1544 respectively) accumulated under different running conditions. With the exception of a.) all graphs are shutter open runs.

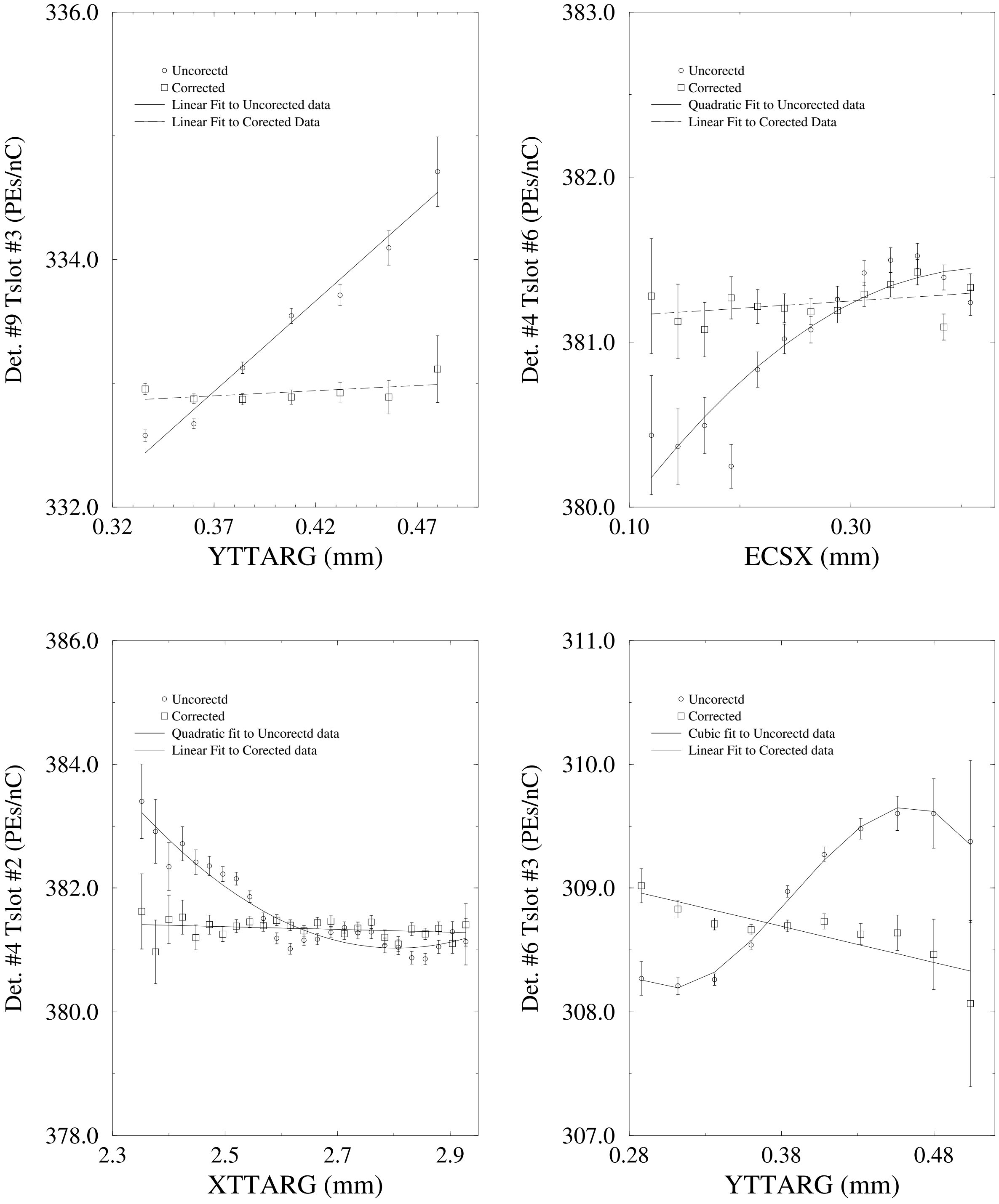

Figure 6.3: The corrected SAMPLE detector response of individual detectors, using the data set used for Figure 6.2 (d), as seen in individual timeslots as a function of an incident beam parameter which is defined in Table 6.2.

6.3 Detector Signal Corrections

The detector signal was corrected for changes in the incident electron position, angle, and energy between the pulse-pairs used in an asymmetry calculation to remove the influence of helicity-correlated changes on the measured asymmetry. The observed helicity-correlated changes in the incident electron properties are shown in Table 6.2. The multiple regression techniques [55] are used to determine the correlation between the detector signal and each of the beam properties: energy, position, and angle at the target. Once the correlations are determined, the detector response (R_d) may be written as a sum of the signal from electron backscattering ($Signal$) plus contributions (dominated by background) correlated with the position, angle, and energy fluctuations of the incident electrons

$$R_d = Signal + \sum_{j=1}^{5}\sum_{l=1}^{4}\beta_j^l P_l(X_j). \tag{6.1}$$

The symbol $P_l(X_j)$ denotes the incident electron parameter X_j expanded to the l^{th} order Legendre polynomial and β_j^l represents the expansion coefficient. This technique requires that the data be analyzed twice, first to calculate the correlation matrix to the desired expansion order using the natural fluctuations in the incident electrons and then to perform the actual correction. These corrections contribute to both the statistical uncertainty (uncertainty in the fit) and the systematic uncertainty (truncating the expansion to 4th order or less) of the measured asymmetry.

6.3.1 Fitting the Detector Response

Multiple regression techniques [55] are used to determine the coefficient β_j^l which to first order (l=1) represents the slopes $\frac{\partial R_d}{\partial P_0(X_j)}$ in Equation 6.1. Correlation coefficients r_{jk}^{lm} and r_{jy}^{l} are defined in terms of the ratio of covariances $\frac{(s_{jk}^{lm})^2}{s_j^l s_k^m}$ and $\frac{(s_{jy}^{l})^2}{s_j^l s_y^l}$ respectively. The covariances are defined as

$$(s_{jk}^{lm})^2 = \frac{1}{N-1}\sum^{N}[(P_l(X_j) - \overline{P_l(X_j)})(P_m(X_k) - \overline{P_m(X_k)})] \tag{6.2}$$

$$
\begin{aligned}
(s^l_{jy})^2 &= \frac{1}{N-1}\sum^N[(P_l(X_j) - \overline{P_l(X_j)})(R_d - \overline{R_d})] && (6.3)\\
(s^l_j)^2 &= \frac{1}{N-1}\sum^N(P_l(X_j) - \overline{P_l(X_j)})^2 && (6.4)\\
(s_y)^2 &= \frac{1}{N-1}\sum^N(R_d - \overline{R_d})^2 && (6.5)
\end{aligned}
$$

The method of least squares is adopted to generate a system of equations that minimize the χ^2 of the fit by setting derivatives of χ^2 with respect to each parameter to zero.

$$
\begin{pmatrix} r^1_{1y} \\ r^2_{1y} \\ r^3_{1y} \\ r^4_{1y} \\ r^1_{2y} \\ r^2_{2y} \\ r^3_{2y} \\ r^4_{2y} \\ r^1_{3y} \\ \vdots \\ r^4_{5y} \end{pmatrix}
=
\begin{pmatrix}
r^{11}_{11} & r^{12}_{11} & \cdots & r^{14}_{15} \\
r^{21}_{11} & r^{22}_{11} & \cdots & r^{24}_{15} \\
r^{31}_{11} & r^{32}_{11} & \cdots & r^{34}_{15} \\
r^{41}_{11} & r^{42}_{11} & \cdots & r^{44}_{15} \\
r^{11}_{21} & r^{12}_{21} & \cdots & r^{14}_{25} \\
r^{11}_{21} & r^{22}_{21} & \cdots & r^{24}_{25} \\
r^{11}_{21} & r^{32}_{21} & \cdots & r^{34}_{25} \\
r^{11}_{21} & r^{42}_{21} & \cdots & r^{44}_{25} \\
r^{11}_{31} & r^{12}_{31} & \cdots & r^{14}_{35} \\
\vdots & \vdots & \ddots & \vdots \\
r^{41}_{51} & r^{42}_{51} & \cdots & r^{44}_{55}
\end{pmatrix}
\begin{pmatrix} b^1_1 \\ b^2_1 \\ b^3_1 \\ b^4_1 \\ b^1_2 \\ b^2_2 \\ b^3_2 \\ b^4_2 \\ b^1_3 \\ \vdots \\ b^4_5 \end{pmatrix}. \qquad (6.6)
$$

The vector b^l_j in Equation 6.6 may be determined by inverting the matrix r^{lm}_{ij} [2]. In this form the vector b^l_j is related to the desired parameters β^l_j by a ratio of standard deviations : $\beta^l_j = \frac{s_y}{s^l_j} b^l_j$. The uncertainty in the above parameters may be estimated [55] by summing the uncertainties in quadrature.

$$
\begin{aligned}
\sigma^2_{b^l_j} &= \sum_{i=1}^N (\sigma^l_j)^2 \left(\frac{\partial b^l_j}{\partial R_{d,i}}\right)^2 \\
&= \frac{1}{N-1}\left(\frac{r^{-1}_{jj}}{(s^l_j)^2}\right)^2 \sigma^2
\end{aligned}
$$

[2]The Numerical Recipes[56] routines "ludcmp" and " lubksb" are used to solve the matrix problem

$$\approx \frac{1}{N-1}\left(\frac{r_{jj}^{-1}}{(s_j^l)^2}\right)\frac{1}{N-n-1}\sum\left[(R_{d,i}-\overline{R_d})-\sum b_j^l(P_l(X_j)-\overline{P_l(X_j)})\right]^2 \quad (6.7)$$

where n is the order of the expansion ($\leq$4), the σ^2's are the "true" distribution variances, s^2's are the measured distribution variances (see Equations 6.5) which use the distribution average at the cost of one degree of freedom (N-1).

In practice the expansion order of the fits are constrained to give a positive definite error matrix. This is accomplished by reducing the Legendre polynomial expansion from 4th order until the error matrix becomes positive definite for each of the 5 incident electron parameters separately. Then the order from each individual fit is used to simultaneously fit all 5 incident electron parameters such that correlations are considered and the possibility of over correcting the detector signal is minimized.

6.3.2 An Example Fitting the Detector Response

Consider a first order description of the detector response R_d to only two beam parameter monitors XTARG and YTARG. The prescription outlined above requires that six terms $(r_{1y}^1, r_{2y}, r_{11}^{11}, r_{11}^{12}, r_{21}^{11}, r_{21}^{12})$ be calculated in order to determine the slopes (b_1^1 and b_2^1) by inverting the matrix equation below.

$$\begin{pmatrix} r_{1y}^1 \\ r_{2y}^1 \end{pmatrix} = \begin{pmatrix} r_{11}^{11} & r_{11}^{12} \\ r_{21}^{11} & r_{21}^{12} \end{pmatrix} \begin{pmatrix} b_1^1 \\ b_2^1 \end{pmatrix}. \quad (6.8)$$

The first two terms (r_{1y}^1 and r_{2y}^1) represent the ratio of the covariance between the monitor (XTARG and YTARG respectively) and the detector response R_d to the standard deviations (the square root of the variance) of both the monitor and the detector response.

$$r_{1y}^1 = \frac{\sum(XTARG-\overline{XTARG})(R_d-\overline{R_d})}{(\sum(XTARG-\overline{XTARG})^2\times\sum(R_d-\overline{R_d})^2)^{1/2}} \quad (6.9)$$

The diagonal terms (r_{11}^{11} and r_{21}^{12}) in the above matrix are the usual standard deviations of the monitors XTARG and YTARG respectively. The off diagonal terms (r_{11}^{12} and r_{21}^{11}) are the same ratio of the covariance between XTARG and YTARG to the standard deviations of both XTARG and YTARG.

$$r_{11}^{12} = r_{11}^{11} \quad = \quad \frac{\sum(XTARG - \overline{XTARG})(YTARG - \overline{YTARG})}{(\sum(XTARG - \overline{XTARG})^2 \times \sum(YTARG - \overline{YTARG})^2)^{1/2}} \tag{6.10}$$

The detector response is modeled by the above system of equations as a linear function of the beam parameters XTARG and YTARG the slope of which is given by the coefficients b_1^1 and b_2^1.

6.3.3 Results of Correction Procedure

Table 6.2 reports the average "pulse-pair" difference shown in Figure 6.4 for the five incident electron parameters used to correct the detector signal. Although the position differences are not zero, they are an order of magnitude less than what would theoretically contribute to the systematics outlined in Chapter 5. The measured statistics, however, are much larger than those calculated (presumable due to background) therefore the corrections are significant.

Beam Parameter	Pulse Pair difference	Description
XTARG $\equiv$ (NNH1X+NNH2X)/2	-71.72 $\pm$ 6.24 nm	Horiz. Pos. diff.
YTARG $\equiv$ (NNH1Y+NNH2Y)/2	-34.99 $\pm$ 2.6 nm	Vert. Pos. diff.
XTTARG $\equiv$(NNH1X-NNH2X)/2	30.80 $\pm$ 1.63 nm	Horiz. Angular diff.
YTTARG $\equiv$ (NNH1Y-NNH2Y)/2	34.31 $\pm$ 1.75 nm	Vert. Angular diff.
ECSX	-4.00 $\pm$ 7.31 eV	Electron energy diff.

Table 6.2: Average pulse pair differences of beam parameters used to correct the detector signal. The ECSX monitor is used for correcting the signal due the monitors sensitivity to the background generated when the electron beam interacts with a collimator located near the monitor. Equation 5.2 shows that the influence of energy on the measured asymmetry is two orders of magnitude less than the measured asymmetry.

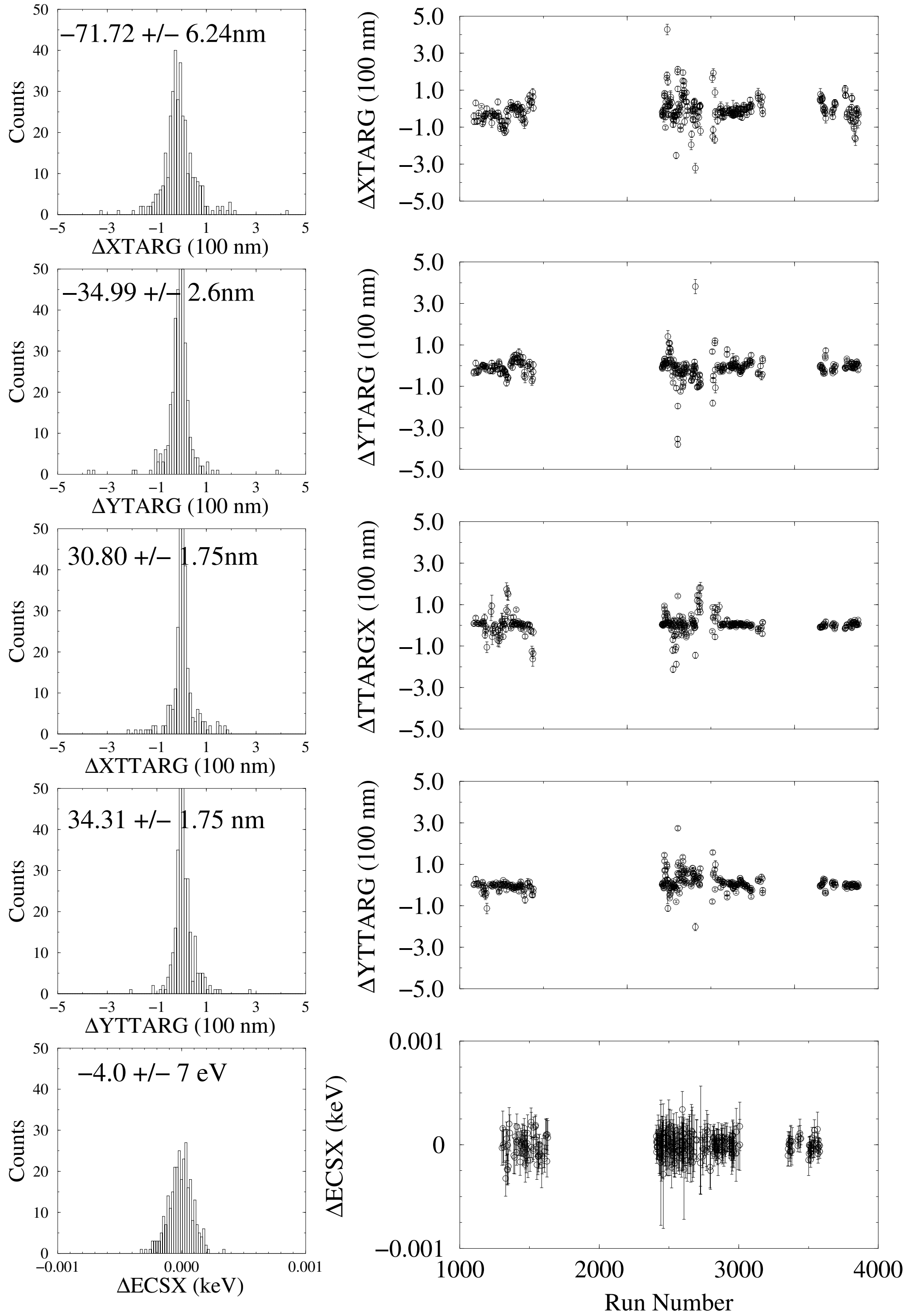

Figure 6.4: The distribution of pulse pair differences for the 5 incident electron parameters.

A comparison of Figures 6.2 and 6.3 shows that the total detector response (denoted by the solid circles in Figure 6.2) depends on both the absolute beam position with respect to each timeslot as well as the position fluctuations within each timeslot. The contribution of the four position sensitive monitors to the measured asymmetry that is corrected using the total detector signal for ten representative runs is shown in Table 6.3 and Table 6.4. The contribution of the energy sensitive position monitor (ECSX) is shown in Table 6.5 along with the calculated χ^2/ν[55] values for the fit.[3] Table 6.3 is consistent with the four graphs shown in Figure 6.2. Under the conditions of Figures 6.2a-c, a modest difference between a linear fit and a higher order fit can be expected with χ^2/ν values larger than unity. There are also situations like Figure 6.2d, where a higher order description of the nonlinear response will be more representative and reduce the χ^2/ν value. The statistical uncertainty in the fit is usually dominated by the statistical uncertainty in the yield and as a result the statistical fit uncertainty doesn't appreciably change with fit order unless there is a clear problem with the fit as indicated by a large χ^2/ν value.

Table 6.5 shows a consistent reduction in the contribution of the ECSX monitor correction to the raw asymmetry for higher order fits. The ECSX monitor is positioned near a collimator that is known to generate high background levels in the detector in the event that the beam scrapes the collimator. During the experiment, attempts were made to constrain the beam position so that a minimum background level was observed in the detector. As a result of centering the beam position within the ECSX monitor, the detector response with respect to this monitor has more pronounced parabolic features (see Figure 6.5) than the position monitors which may not be centered at a location corresponding to the minimum background level (see response denoted using open triangles and open squares in Figure 6.2c). A linear fit to the parabolic response would tend to over correct the detector signal in the event that one side of the parabola were missing. There are three primary benefits accrued

[3]Only one χ^2/ν value is applicable since all five monitors are simultaneously fit to account for correlations.

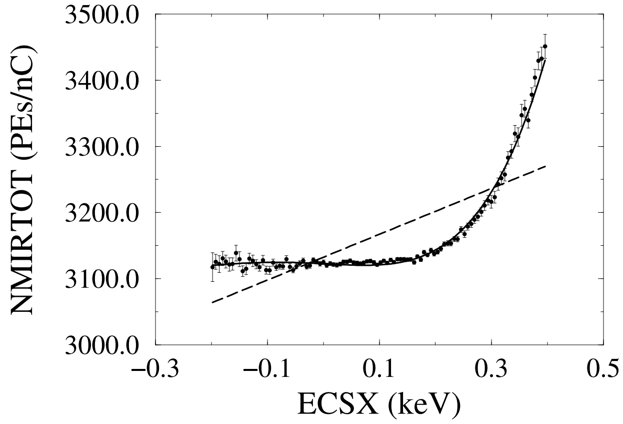

Figure 6.5: The detector response to beam position fluctuations at the ECSX monitor with a first order fit (dashed lines) and a 4th order fit (solid line).

when the detector response is corrected for beam fluctuations with respect to each of the ten detectors and ten timeslots separately. First, the goodness of fit improves thereby reducing the model uncertainty in the corrections. Second, the asymmetry measured in the ten detectors can be combined in a manner that will account for the different contributions of the Čerenkov signal to each of the four detector types (see Table 4.6). Third, peculiar dependences of the detector signal on beam position for different timeslots (such as shown in Figure 6.2) can be addressed more directly.

Table 6.6 shows an example of the contribution of the position monitors used to correct the detector signal from one of the ten detectors in one timeslot to the asymmetry in runs 2429, 3534, and 3570. The χ^2/ν values are consistently closer to unity than in Table 6.5. Tables 6.7- 6.9 represent the asymmetry corrections for individual detectors and timeslots from each of the five monitors averaged by weighting each correction using the individual detector asymmetry uncertainty and are the analogs of Tables 6.3- 6.5. By weighting the average, the noise of each detector is accounted for and as a result the raw asymmetries A_{raw} are not expected to be equal. The goodness of fit, as determined by the quantity χ^2/ν[55], improves when corrections are made to individual detectors and timeslot using the model in Section 6.3.1.

			Corrections due to		
Run #	A_{raw} (PPM)	Order	XTARG(PPM)	Order	YTARG(PPM)
2429	-7.33 ± 5.93	1st	-0.04 ± 0.06		-0.13 ± 0.08
		4	-3.03 ±1.21	3	+0.07 ± 0.03
2501	-3.45 ± 4.31	1st	-2.31 ± 3.31		-1.52 ± 1.41
		2	0.80 ± 0.30	2	-1.05 ± 0.19
2514	1.08± 4.49	1st	-0.55 ± 0.48		-0.15 ± 0.09
		2	0.72 ± 0.48	2	0.76 ± 0.08
2528	2.26 ± 4.36	1st	-1.68 ± 0.38		0.02 ± 0.17
		2	-2.05 ± 0.13	4	-0.17 ± 0.08
2555	-0.24 ± 4.57	1st	0.34 ± 0.09		0.08 ± 0.14
		4	-0.75 ± 0.10	4	0.16 ± 0.06
2569	1.86 ± 4.2	1st	-0.49 ± 0.27		-0.01 ± 0.02
		2	-0.46 ± 0.19	2	-0.17 ± 0.92
2913	-3.66 ± 4.42	1st	0.01 ± 0.16		-0.52 ± 0.32
		2	-0.01 ± 0.12	2	-0.61 ± 0.27
3365	2.27 ± 4.64	1st	-3.15 ± 0.97		0.14 ± 0.05
		2	-1.08 ± 0.15	3	0.30 ± 0.06
3534	-2.24 ± 4.55	1st	-0.59 ± 0.14		-0.08 ± 0.29
		2	-1.29 ± 0.15	2	-0.20 ± 0.05
3570	-3.05 ± 4.5	1st	-0.43 ± 0.6		0.04 ± 0.01
		2	0.44 ± 0.15	1	0.13 ± 0.03

Table 6.3: Corrections due to XTARG and YTARG beam parameters. Corrections are made as described in Section 6.3.1 to the *total* detector signal representing a sum of all ten detectors. Note: the higher order fit is the one of highest order (≤ 4) that still yields a positive definite error matrix. The χ^2/ν is given in Table 6.5. Uncertainties in the correction include uncertainties from correlations in the fit parameters as well as the measurement uncertainties for ΔXTARG and ΔYTARG.

			Corrections due to		
Run #	A_{raw} (PPM)	Order	XTTARG	Order	YTTARG
2429	-7.33 ± 5.93	1st	0.51 ± 0.44		0.08 ±0.12
		2	-1.90 ± 0.49	3	-0.21 ±0.09
2501	-3.45 ± 4.31	1st	4.84 ± 3.55		3.31 ±1.41
		2	0.89 ± 0.44	4	2.23 ± 0.72
2514	1.08± 4.49	1st	0.37 ± 0.31		1.4 ± 0.19
		3	0.53 ± 0.07	2	0.05 ± 0.01
2528	2.26 ± 4.36	1st	0.61 ± 0.13		-0.02 ± 0.05
		2	-0.22 ± 0.04	3	-0.15 ± 0.07
2555	-0.24 ± 4.57	1st	0.47 ± 0.29		0.02 ± 0.06
		3	-0.03 ± 0.06	4	0.25 ± 0.06
2569	1.86 ± 4.2	1st	-0.11 ± 0.12		0.37 ± 0.21
		2	-0.11 ± 0.03	3	0.41 ± 0.66
2913	-3.66 ± 4.42	1st	0.09 ± 0.19		-0.01 ± 0.08
		2	-0.06 ± 0.03	3	-0.12 ± 0.02
3365	2.27 ± 4.64	1st	2.27 ± 0.82		0.06 ± 0.03
		2	1.06 ± 0.24	3	-0.03 ± 0.06
3534	-2.24 ± 4.55	1st	-0.71 ± 0.15		-0.23 ± 0.17
		2	-0.38 ± 0.04	2	-0.45 ± 0.05
3570	-3.05 ± 4.5	1st	0.59 ± 0.48		0.05 ± 0.07
		2	0.10 ± 0.02	1	0.06 ± 0.02

Table 6.4: Contributions of the XTTARG and YTTARG beam parameters to the raw asymmetry when corrections are made as described in Section 6.3.1 to the *total* detector signal representing a sum of all ten detectors. Note: the higher order fit is the one of highest order ($\leq$ 4) that still yields a positive definite error matrix. The χ^2/ν is given in Table 6.5. Uncertainties in the correction include uncertainties from correlations in the fit parameters as well as the measurement uncertainties for ΔXTTARG and ΔYTTARG.

			Corrections due to		
Run #	A_{raw} (PPM)	Order	ECSX	χ^2/ν	A^{tot}_{con} (PPM)
2429	-7.33 ± 5.93	1st	-2.83 ± 0.001	15.4	-2.41 ± 0.47
		3	0.12 ± 0.002	5.2	-4.95 ± 1.31
2501	-3.45 ± 4.31	1st	-0.57 ± 0.75	26.1	-3.76 ± 5.30
		2	-0.03 ± 0.0002	9.5	-2.84 ± 0.92
2514	1.08± 4.49	1st	-0.007 ± 0.02	3.2	-1.06 ± 0.61
		2	0.01 ± 0.0001	1.8	2.07 ± 0.49
2528	2.26 ± 4.36	1st	-0.05 ± 0.25	2.6	-1.12 ± 0.51
		2	-0.08 ± 0.0008	1.5	-2.67 ±0.17
2555	-0.24 ± 4.57	1st	-0.11 ± 0.08	5.4	0.82 ± 0.35
		2	-0.01 ± 0.0001	2.1	-0.38 ± 0.14
2569	1.86 ± 4.2	1st	0.10 ± 0.07	2.5	-0.14 ± 0.37
		2	-0.01 0.0002	1.3	-0.34 ± 1.15
2913	-3.66 ± 4.42	1st	0.17 ± 0.21	2.3	-0.26 ± 0.46
		2	-0.09 ± 0.01	1.8	-0.89 ± 0.30
3365	2.27 ± 4.64	1st	0.07 ± 0.10	6.2	-0.61 ± 1.28
		2	-0.001 ± 0.0005	1.4	0.25 ± 0.30
3534	-2.24 ± 4.55	1st	0.21 ± 0.12	1.8	-1.40 ± 0.41
		1	-0.005 ± 0.001	1.5	-2.33 ± 0.17
3570	-3.05 ± 4.5	1st	-0.06 ± 0.09	1.7	0.19 ± 0.78
		1	0.01 ± 0.001	1.4	0.68 ± 0.16

Table 6.5: Contributions of the energy sensitive position monitor (ECSX) to the raw asymmetry when corrections are made as described in Section 6.3.1 to the *total* detector signal representing a sum of all ten detectors. The χ^2/ν value represents the goodness of fit for all five monitors used in the correction. Note: the higher order fit is the one of highest order (≤ 4) that still yields a positive definite error matrix. Uncertainties in the correction include uncertainties from correlations in the fit parameters as well as the measurement uncertainties for ΔECSX. A^{tot}_{con} is the total contribution from all five monitors which will be used to correct the raw asymmetry A_{raw}.

		Corrections due to					
A_{raw} (PPM)	O	XTARG	YTARG	XTTARG	YTTARG	χ^2/ν	A^{tot}_{con} (PPM)
25.18$\pm$ 44.13	1st	-0.85 $\pm$ 0.82	0.03 $\pm$ 0.05	-0.85 $\pm$ 1.56	0.11 $\pm$ 0.16	1.2	0.98 $\pm$ 1.79
	$\leq$4	-1.09 $\pm$ 0.16	0.46 $\pm$ 0.10	-1.96 $\pm$ 0.73	0.67 $\pm$ 0.99	.98	-1.90 $\pm$ 1.24
9.58 $\pm$ 43.36	1st	-1.24 $\pm$ 1.91	-0.98 $\pm$ 1.41	-1.99 $\pm$ 0.02	-0.57 $\pm$ 0.28	1.4	-4.63 $\pm$ 2.41
	$\leq$4	-1.85 $\pm$ 0.87	0.94 $\pm$ 0.56	-0.61 $\pm$ 0.002	-1.06 $\pm$ 0.17	1.1	-2.62 $\pm$ 1.05
-49.21$\pm$ 43.06	1st	1.07 $\pm$ -0.80	-1.55 $\pm$ 1.55	-0.09 $\pm$ 0.06	0.10 $\pm$ 0.05	.98	-0.67 $\pm$ 1.76
	$\leq$4	0.70 $\pm$ .01	-1.23 $\pm$ 1.08	-0.83 $\pm$ 0.77	0.58 $\pm$ 0.27	.98	-0.74 $\pm$ 1.35

Table 6.6: Example of position monitor contributions to the raw asymmetry when corrections are made as described in Section 6.3.1 to one of the ten detectors in an individual timeslot for run # 2429, 3534, and 3570 respectively. The $\leq$ symbol in column two is used to remind the reader that the high order fit is expanded to a fourth order Legendre polynomial and constrained to give a positive definite error matrix. Uncertainties in the correction include uncertainties from correlations in the fit parameters as well as the measurement uncertainties for ΔXTARG,ΔYTARG, ΔXTTARG, ΔYTTARG.

			Corrections due to	
Run #	A_{raw} (PPM)	Order	XTARG(PPM)	YTARG(PPM)
2429	-6.75 ± 4.32	1	0.20 ± 0.25	-0.05 ± 0.02
		HO	0.37 ± 0.27	-0.7 ±0.01
2501	-6.13 ± 5.48	1	-0.05 ± 0.7	-0.25 ±0.01
		HO	-0.10 ± 0.5	-2.9 ± 0.11
2514	0.03 ± 4.49	1	0.20 ± 0.10	0.15 ± 0.05
		HO	0.1 ± 0.05	0.7 ± 0.07
2528	2.10 ± 4.51	1	0.20 ± 1.70	0.05± 0.01
		HO	-0.20 ± 1.70	0.1± 0.01
2555	0.46 ± 4.32	1	-0.40 ± 0.45	-0.07± 0.05
		HO	0.45 ± 0.45	0.1 ± 0.06
2569	1.52 ± 5.19	1	0.15 ± 0.75	-0.05 ± 0.05
		HO	1.50 ± 0.8	0.55 ± 0.07
2913	-3.41 ± 4.30	1	-0.01 ± 0.15	-0.03± 0.10
		HO	-0.15 ± 0.30	-0.05± 0.05
3365	2.73 ± 4.53	1	0.3 ± 0.2	-0.15 ± 0.05
		HO	0.30 ± 0.20	0.30±0.10
3534	-3.2 ± 4.41	1	-0.4 ± 0.45	-0.05 ±0.05
		HO	-0.25 ± 0.4	-0.10± 0.05
3570	-3.26 ± 4.36	1	-0.15 ± 0.4	0.06 ±0.05
		HO	-0.15 ± 0.4	0.10 ± 0.05

Table 6.7: Average contributions of the XTARG and YTARG beam parameters to the raw asymmetry when corrections are made as described in Section 6.3.1 to individual timeslots and detectors. Uncertainties in the correction include uncertainties from correlations in the fit parameters as well as the measurement uncertainties for ΔXTARG and ΔYTARG.

			Corrections due to	
Run #	A_{raw} (PPM)	Order	XTTARG(PPM)	YTTARG(PPM)
2429	-6.75 ± 4.32	1	-0.10 ± 0.15	0.10 ± 0.8
		HO	0.65 ± 0.21	0.25 ± 0.50
2501	-6.13 ± 5.48	1	0.15 ± 0.10	0.15 ± 0.55
		HO	0.46 ± 0.17	0.15 ± 0.55
2514	0.03 ± 4.49	1	-0.05± 0.01	-0.25 ± 0.02
		HO	0.41 ± 0.02	0.65 ± 0.03
2528	2.10 ± 4.51	1	-0.10 ± 0.06	-0.05 ± 0.60
		HO	0.46 ± 0.01	0.05 ± 0.40
2555	0.46 ± 4.32	1	0.10 ± 0.7	-0.01 ± 0.5
		HO	0.05 ± 0.05	0.10 ± 0.31
2569	1.52± 5.19	1	0.10 ± 0.15	-0.01 ± 0.15
		HO	1.05 ± 0.98	0.25 ± 0.16
2913	-3.41 ± 4.3	1	0.03 ± 0.20	-0.01 ± 0.8
		HO	-0.01±0.20	-0.05 ± 0.75
3365	2.73 ± 4.53	1	-0.05 ± 0.35	0.05 ± 0.5
		HO	-0.10 ± 0.27	0.65 ± 0.51
3534	-3.20 ± 4.41	1	0.20 ± 0.25	0.01 ± 0.10
		HO	0.20 ± 0.26	-0.35 ± 0.13
3570	-3.26 ± 4.36	1	0.07 ± 0.4	-0.05 ± 0.05
		HO	0.20 ± 0.45	0.10 ± 0.07

Table 6.8: Average contributions of the XTTARG and YTTARG beam parameters to the raw asymmetry when corrections are made as described in Section 6.3.1 to individual timeslots and detectors. Uncertainties in the correction include uncertainties from correlations in the fit parameters as well as the measurement uncertainties for ΔXYTARG and ΔYTTARG.

			Corrections due to		
Run #	A_{raw} (PPM)	Order	ECSX(PPM)	χ^2/ν	A^{tot}_{cor}(PPM)
2429	-6.75 ± 4.32	1	-0.20 ± 0.14	0.90	-0.05 ± 0.86
		HO	-0.18 ± 0.05	0.90	0.39 ± 0.61
2501	-6.13 ± 5.48	1	0.03 ± 0.02	1.10	0.03 ± 0.90
		HO	0.07 ± 0.01	1.00	-2.33 ± 0.77
2514	0.03 ± 4.49	1	0.10 ± 0.06	1.20	0.15 ± 0.13
		HO	-0.08 ± 0.04	1.01	1.78 ± 0.10
2528	2.10 ± 4.51	1	0.13 ± 0.07	0.98	0.23 ± 1.80
		HO	0.08 ± 0.05	0.99	0.49 ± 1.75
2555	0.46 ± 4.32	1	-0.23 ± 0.09	1.20	0.61 ± 0.98
		HO	0.14 ± 0.07	1.00	0.84 ± 0.56
2569	1.52± 5.19	1	-1.50 ± 0.04	0.93	-1.31 ± 0.78
		HO	-0.10 ± 0.01	0.95	3.25 ± 1.28
2913	-3.41 ± 4.3	1	-0.11 ± 0.03	1.10	-0.13 ± 0.84
		HO	-0.12 ± 0.01	0.98	-0.38 ± 0.83
3365	2.73 ± 4.53	1	0.10 ± 0.04	1.0	0.25 ± 0.65
		HO	0.07 ± 0.02	1.0	1.22 ± 0.62
3534	-3.20 ± 4.41	1	-0.10 ± 0.07	0.90	-0.34 ± 0.53
		HO	-0.12 ± 0.05	0.90	-0.62 ± 0.50
3570	-3.26 ± 4.36	1	-0.10 ± 0.9	1.10	-0.17 ± 1.07
		HO	-0.10 ± 0.02	1.00	0.15 ± 0.61

Table 6.9: Average contributions of the energy sensitive position monitor (ECSX) to the raw asymmetry when corrections are made as described in Section 6.3.1 to individual timeslots and detectors. The average goodness of fit (χ^2/ν) and asymmetry correction from the five BPM monitors A_{cor} is given for each run. Uncertainties in the correction include uncertainties from correlations in the fit parameters as well as the measurement uncertainties for ΔECSX.

6.3.4 Uncertainties in Corrections

The detector signal correction contribution to the measured asymmetry for each of the five beam monitors is shown in Figures 6.6 - 6.7 using a linear and a higher order fit to individual detectors and timeslots. Table 6.10 quantifies the corrections by averaging over the analyzed data set weighting each correction by the respective detector asymmetry uncertainty. The largest discrepancy between a linear and a higher order correction contribution to the asymmetry appears in monitors XTARG, XTTARG, and ECSX. The correction contribution to the measured asymmetry by the monitors YTARG and YTTARG are not sensitive to order (linear or higher) chosen for the fit. Correlations between the five monitors have been included in the uncertainty reported in Table 6.10. A conservative estimate of the uncertainty in the correction is 0.1 PPM based on the differences between the 1st and higher order (HO) asymmetry contributions in Table 6.10.

The contribution to the asymmetry uncertainty that results from correlations induced by correcting the detector response to beam position fluctuations using the model described in Section 6.3.1 is quantified through standard error propagation (see Appendix B.5) in Table 6.11. The model may be used to correct either the total detector signal (a linear sum of the 10 detectors averaged over all timeslots) or corrections may be applied to each of the ten individual Čerenkov detectors in each of the ten timeslots. The goodness of fit, as determined by the quantity χ^2/ν[55], improves when corrections are made to individual detectors and timeslots rather than to a linear sum of all ten detectors averaged over timeslot.

Order	XTARG (PPM)	YTARG (PPM)
1	-0.26 ± 0.08	-0.07 ± 0.02
HO	-0.04 ± 0.06	-0.11 ± 0.02
Order	XTTARG (PPM)	YTTARG (PPM)
1	0.16 ± 0.01	-0.12 ± 0.01
HO	-0.15 ± 0.01	-0.13 ± 0.01
Order	ECSX(PPM)	A_{raw} (PPM)
1	-0.25 ± 0.01	-1.60 ± 0.23
HO	-0.08 ± 0.01	-1.60 ± 0.23
Order	Cor (PPM)	A_{cor}(PPM)
1	-0.54 ±0.08	-1.06 ± 0.24
HO	-0.51 ± 0.07	-1.09 ± 0.24

Table 6.10: Average contributions of the position monitors to the raw asymmetry when corrections are made as described in Section 6.3.1 to individual timeslots and detectors using the entire data set.

Detector	σ_{stat} (PPM)	$\frac{\sigma_1}{\sigma_{stat}}$ (%)	$\frac{\sigma_4}{\sigma_{stat}}$ (%)
1	0.81	0.54	4.93
2	0.94	0.59	6.75
3	0.80	0.56	5.80
4	0.74	0.96	5.53
5	1.05	0.67	8.81
6	0.98	0.65	7.36
7	0.72	0.50	5.71
8	0.75	0.53	6.65
9	0.86	0.60	7.84
10	0.77	0.51	6.45

Table 6.11: Calculated increases in the statistical uncertainty shown in Table 6.10 that results from corelation induced by applying beam corrections (see Appendix B.5) to the asymmetry. Correlations induced by pedestals (see Appendix B.4) increase the uncertainty by ($\frac{\sigma_{pedcor}}{\sigma_{stat}}$) 1.88 %. The columns involving σ_1 and σ_4 represent the contribution of first and fourth order fits to the uncertainty in the asymmetry.

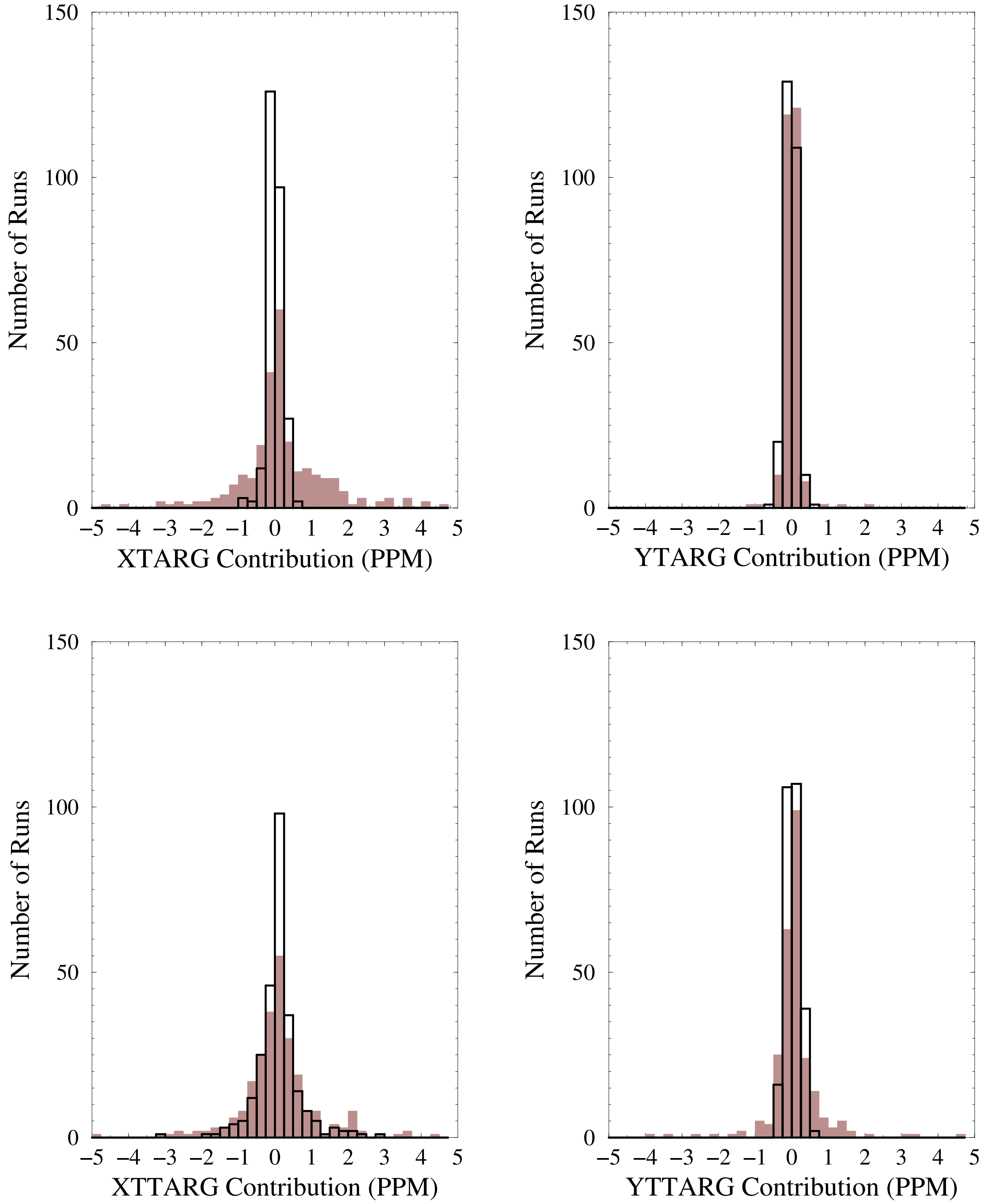

Figure 6.6: Contributions of the four North Hall beam monitors to the measured asymmetry. The shaded region represents contributions when a first order fit is used. The unshaded region is from higher order corrections as described in Section B.5

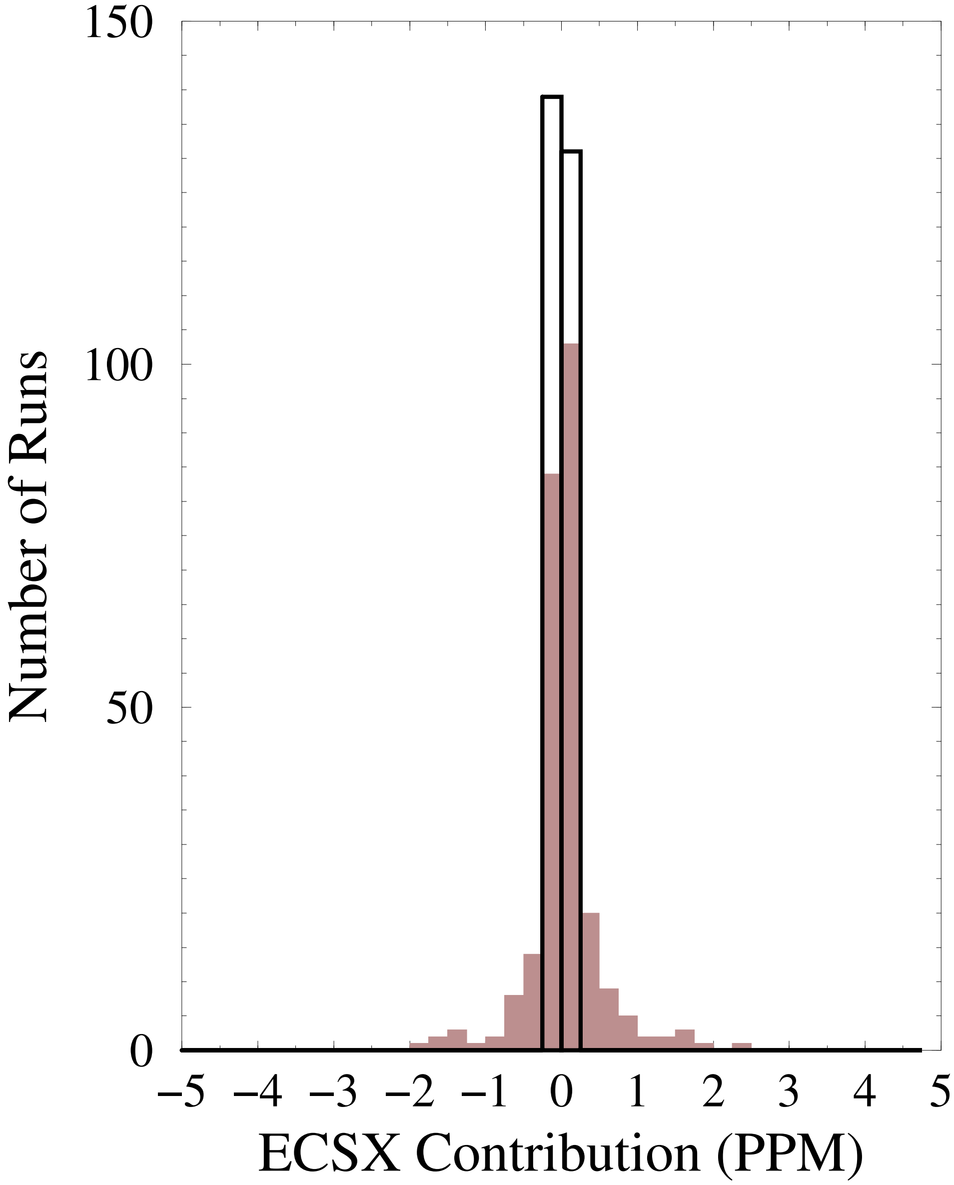

Figure 6.7: Contribution of the energy dependent beam monitor ECSX to the measured asymmetry. The shaded region represents contributions when a first order fit is used. The unshaded region is from higher order corrections as described in Section B.5

6.4 Measured Asymmetries

Asymmetries were measured for a hydrogen and a helium target. Replacing the hydrogen with helium (the helium target is $\sim$ 14 times thinner than the hydrogen target) is important to determine the effects of the aluminum windows and helium backing cell on the asymmetry measured with the hydrogen target. The asymmetry measured using a helium target with the shutters open averaged to 1.56 ± 2.99. Although it would be preferable to measure zero to the .1 PPM level it is time prohibitive. It may be argued that the LED measurements in Section 5.6 supplement the measurements using helium and measurements using unpolarized electrons to provide a solid foundation that the apparatus has yet to display evidence of systematic effects related to the electronics used to label the incident electron helicity.

The most direct systematic check for false asymmetries relies on redefining the electronic labeling of the helicity states in a mechanical manner independent of any electronics. A "Slow Helicity Reversal" half waveplate is located after the last linear polarizer but before the helicity Pockel's cell in the polarized source optics line (see Figure 3.2). The sense of the circular polarization at the polarized source may be flipped by simply rotating the wave plate by 45°. The detected Čerenkov asymmetry was -1.48 ± 0.36 (normal mode) for a waveplate rotated to 45 degrees and 1.69 ± 0.31 (reverse mode sign must be reversed to be comparable to normal mode) for a waveplate oriented at zero degrees. The agreement of these results is a clear indication of parity violation.

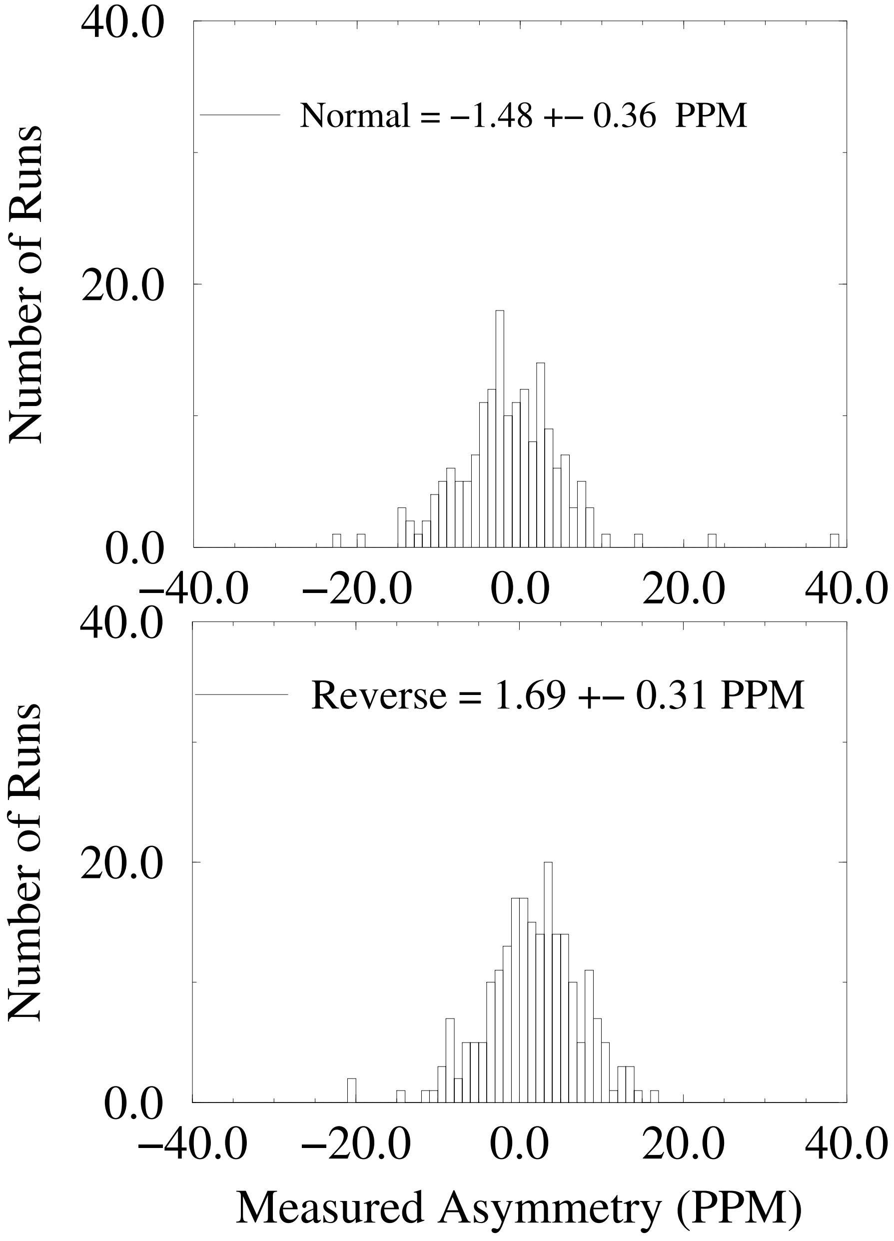

Figure 6.8: Average raw asymmetry for two different orientations (Normal and Reverse) of the slow helicity reversal half wave plate. A change in the sign of the asymmetry when the half waveplate is rotated 45^o indicates parity violation.

The average asymmetry, uncorrected for the incident electron parameters, using an unpolarized hydrogen target and a polarized 200 MeV incident electron beam was -1.60 $\pm$ 0.23 PPM with the shutter open and -1.32 $\pm$ 1.13 PPM with the shutter closed. With the incident electron parameter corrections mentioned in Section 6.3.1, the shutter open asymmetry is reduced to -1.09 $\pm$ 0.24 PPM and the shutter closed asymmetry becomes consistent with zero at -0.63 $\pm$ 1.17 PPM. The average asymmetry measured with the shutters open is comparable to the value of -1.04 $\pm$ 0.24 reported in reference [50]. A histogram of the corrected and uncorrected shutter open asymmetry is shown in Figure 6.9. The increase in the measured uncertainty due to correlations resulting from the pedestal subtraction scheme (see Section B.4 Equation B.13) and the uncertainty in the fit used to correct the data for beam parameter fluctuations (see Section B.5 Equation B.16) is shown in Table 6.11

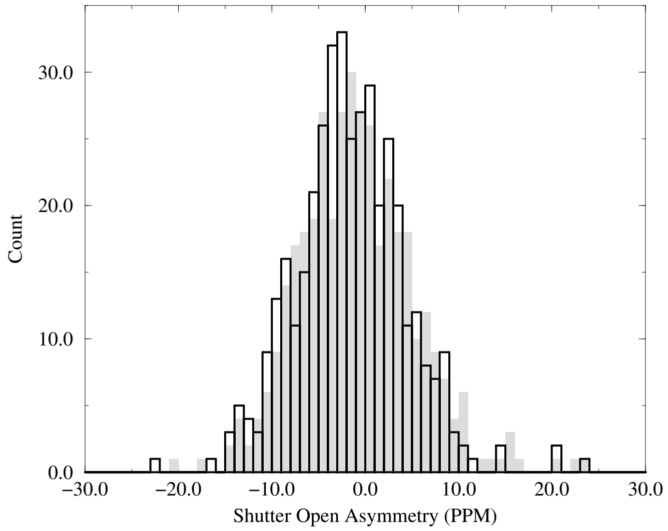

Figure 6.9: The asymmetry measured with the shutters open using an unpolarized liquid hydrogen target and 200 MeV incident polarized electrons. The solid gray histogram represents the uncorrected asymmetry and the dark lined histogram is the asymmetry corrected for incident electron position and energy "pulse-pair" fluctuations.

Source	Asymmetry (PPM)	PedCon (PPM)	FitCon (PPM)
Raw	-1.60 ± 0.23		
[50]	-1.04 ± 0.24		
1st Order	-1.06 ± 0.24	.005	0.001
Higher Order	-1.09 ± 0.24	.005	0.02

Table 6.12: The measured asymmetry without corrections (Raw), from Reference[50], using 1st order corrections, and finally higher order corrections. The column label "PedCon" represents the calculated increase in the asymmetry uncertainty due to pedestal induced correlations as described in Appendix B.4. The column "FitCon" represents the calculated increase in the asymmetry uncertainty that results when applying the corrections (see Appendix B.5)

6.4.1 Beam Polarization Measurement

The incident electron polarization is measured at several points throughout the data set using the apparatus in Figure 3.3 and the methodology described in Section 3.2. As described below, the first step taken in this measurement is to determine the magnet settings (B1 and B2) which maximized the detector sensitivity to the Møller peak. Next, the signal-to-background ratio is determined by measuring the detector yield at several points along the Møller ridge. Finally, the Møller asymmetry is measured and diluted using the fit parameters from the measured detector yield. The measurements below were taking with the longitudinal coils and at a target angle of $(29.8\pm0.4)^o$.

The Møller detector magnets B1 and B2 are set to maximize the detector sensitivity to the Møller peak. The detector yield for several settings of the two detector magnets B1 and B2 is measured. A three dimensional plot (see Figure 6.10) of this data will show a peak along a line in the B1-B2 plane where the two magnetic fields are matched to the same electron scattering energy. The magnet B2 is fixed to correspond to the Møller peak so that B1 may be changed to take measurements along the peak.

The signal-to-background (S/B) is calculated from measurements of the Møller peak at different settings of the magnet B1. Figure 6.11a is a measurement of the

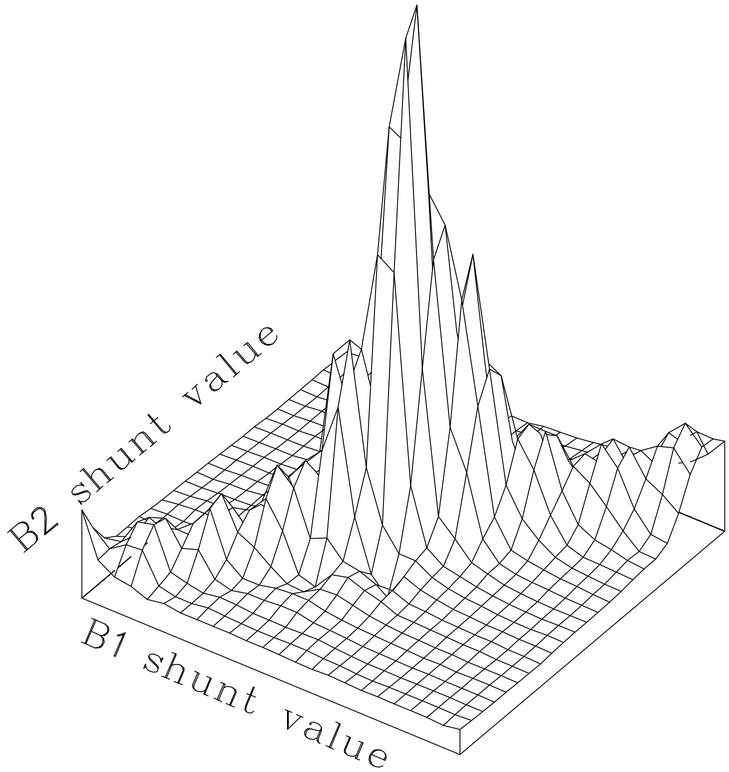

Figure 6.10: Magnet scan around the M oller peak.

detector yield for different setting of the magnet B1. Møller electrons within the acceptance of the detector have an energy close to 100 MeV . Electrons from background processes will slowly vary with energy in a linear fashion. The spectrum in Figure 6.11 is fit to the equation

$$Y = A * e^{-((|S-P|/W)^E)/E} + B0 + B1 * (S - P) \tag{6.11}$$

where Y is the measured yield and S is the shunt value. The Møller amplitude A, the magnet shunt voltage at the Møller peak P, the peak width W, the exponent E, and the linear background parameters $B0$ and $B1$ are all parameters of the fit.

The Møller asymmetry using the same magnet shunt values as the yield measurement above is shown in Figure 6.11b. The measured asymmetry is diluted using the parameters from the yield (see Equation 6.11)

$$\frac{B}{S} = \frac{B0 + B1 * (S - P)}{A * e^{-((|S-P|/W)^E)/E}} \tag{6.12}$$

Run Number	A	P	W	E
2467	0.28 ± 1.08	2797.0 ± 506.15	154.40 ± 1.17	1.77 ± 0.02
2683	0.38 ± 0.01	2791.3 ± 403.78	188.20 ± 1.54	1.73 ± 0.03
2782	0.41 ± 0.003	2830.4 ± 379.04	189.05 ± 1.43	1.72 ± 0.03
2814	0.38 ± 0.004	2799.10 ± 411.16	187.11 ± 2.28	1.77 ± 0.05
	B0	B1($\times 10^6$)		
2467	0.05 ± 0.001	1.43 ± 0.85		
2683	0.07 ± 0.001	$9.80 \pm 0.\ 98$		
2782	0.08 ± 0.001	10.69 ± 1.17		
2814	0.08 ± 0.002	6.30 ± 1.81		

Table 6.13: Typical fit parameters values used.

and compared with the expected Møller asymmetry

$$A_{meas} = \frac{A_{M\o ller}}{1+B/S} \tag{6.13}$$

$$= \frac{-7P_bP_t}{9(1+B/S)}[(7\cos(\theta_t)\sin(\theta_g) - \sin(\theta_t)\cos(\theta_g))\sin(\theta_W)\cos(\phi) - (7\cos(\theta_t)\cos(\theta_g) - \sin(\theta_t)\sin(\theta_g))\cos(\theta_W)]. \tag{6.14}$$

to determine the incident electron polarization (P_t) shown in Table 6.14. The quoted systematic uncertainty is from the measured target polarization (2.0%), setting the target angle (1.0%), determining B/S (3.2%), and the influence of beam heating on the target polarization (1.5%). A systematic asymmetry of 0.5% in the background is assumed. Due to the dependence of the polarization on the quantum efficiency of the GaAs crystal (see Figure 3.4) [4], variations in the measured polarization are expected. The GaAs quantum efficiency varied from 0.5% to 1.5% during the run thus the polarization variations in Table 6.14 are expected.

[4] Higher quantum efficiencies produce electrons originating from deeper within the GaAs crystal which are more likely to suffer from depolarization effects electrons experience when traversing more of the GaAs material en route to being photo-emitted

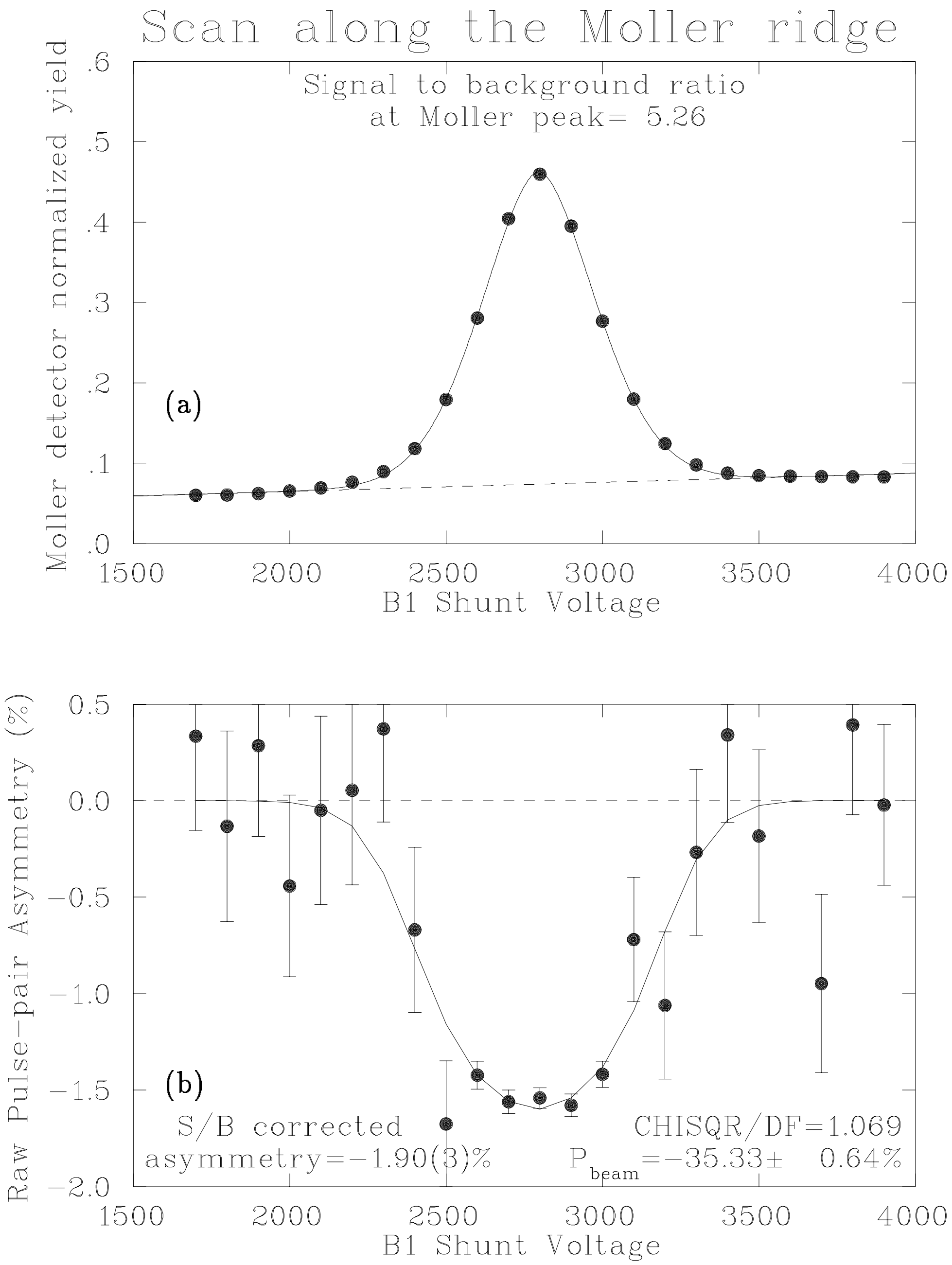

Figure 6.11: a.) Normalized detector yield used to measure the signal-to-background and b.) a typical asymmetry plot for used to extract the beam polarization. The sign of the Møller asymmetry in "Normal" mode is negative. The fit uses Equation 6.13

Run Number Range	Polarization
1280-1600	34.45 $\pm$ .53 $\pm$ 1.6
2400-2682	35.1 $\pm$ 1.7 $\pm$ 1.6
2683-2781	35.6 $\pm$ 0.4 $\pm$ 1.6
2782-2803	37.0 $\pm$ 0.5 $\pm$ 1.6
2804-2813	34.0 $\pm$ 0.4 $\pm$ 1.6
2814-2862	33.9 $\pm$ 0.4 $\pm$ 1.6
2863-2919	35.0 $\pm$ 0.4 $\pm$ 1.6
2920-3010	34.7 $\pm$ 0.4 $\pm$ 1.6
3011-3087	32.3 $\pm$ 0.4 $\pm$ 1.6
3088-3205	34.9 $\pm$ 0.4 $\pm$ 1.6
3444-3448	31.4 $\pm$ 0.7 $\pm$ 1.6
3449-3588	33.9 $\pm$ 0.4 $\pm$ 1.6

Table 6.14: Polarization measurements of the 200 MeV incident electrons used for the different run number ranges. The second uncertainty is systematic.

6.5 The Physics Asymmetry A_{phys}

The physics asymmetry A_{phys} is calculated by diluting the measured asymmetry using the ratio of the shutter closed to shutter open signal, a measurement of the scintillation background, and the incident electron beam polarization. First, the the detector yield asymmetry A_Y is calculated by combining the measured shutter open asymmetry A_o with the shutter closed asymmetry A_c which is diluted using the ratio of the shutter closed signal to the shutter open signal (R). Second, the asymmetry due to elastically backscattered electrons (A_e) is calculated from the asymmetry in the yield (A_Y) using the scintillation measurement from Chapter 4 (s). Lastly, the physics asymmetry A_{phys} is calculated by diluting A_e using the beam polarization measured several times throughout the acquisition of data (see Table 6.14).

The asymmetries measured with the shutters open (A_o) and closed (A_c) are used to determine the light yield asymmetry (A_Y) by diluting the shutter closed asymmetry using the ratio (R) of the shutter closed detector signal (N_c) to the shutter open detector signal (N_o). The light yield asymmetry is given by

$$A_Y = \frac{(N_o^+ - N_c^+) - (N_o^- - N_c^-)}{(N_o^+ - N_c^+) + (N_o^- - N_c^-)} \tag{6.15}$$

$$= \frac{\frac{N_o^+ - N_o^-}{N_o^+ + N_o^-} - \frac{N_c^+ + N_c^-}{N_o^+ + N_o^-}\frac{N_c^+ - N_c^-}{N_c^+ + N_c^-}}{1 - \frac{N_c^+ + N_c^-}{N_o^+ + N_o^-}} \tag{6.16}$$

$$= \frac{A_o - RA_c}{1 - R} \tag{6.17}$$

and is shown in Table 6.15 for each of the ten detectors. The shutter open asymmetry of -1.09 $\pm$ 0.26 PPM (weighted average over the ten timeslots and the ten detectors) is consistent with the value of -1.04 $\pm$ 0.24 PPM appearing in Table 5.3 of Reference [50]

Due to the addition of a lead curtain (which reduces the ratio R in Equation 6.17) near the end of the data sample take in 1996, the series of mini-runs is grouped into two categories representing before the addition of the lead curtain and after. Table 6.16 is the average asymmetry measured in each of the ten detectors before the lead curtain was installed. Table 6.17 is the average asymmetry measured after installation of the lead curtain. The dilution ratio (R), appearing in the fourth column of each table, is reduced by one standard deviation in all the detectors when the lead curtain is added. A weighted average of the diluted asymmetry A_Y in Table 6.16 and Table 6.17 using the row labeled "Mirtot" is -1.19 $\pm$ 0.50 PPM. While this value is consistent with the value of -1.15 $\pm$ 0.54 appearing in Table 6.15 the uncertainty has been reduced by separating the data into the lead curtain on/off categories.

Detector	A_{open}(PPM)	A_{closed}(PPM)	$R = \frac{S_{closed}}{S_{open}}$	A_Y(PPM)
1	-1.33 $\pm$ 0.81	1.20 $\pm$ 3.92	0.22 $\pm$ 0.03	-2.04 $\pm$ 1.68
2	-2.16 $\pm$ 0.94	-6.17 $\pm$ 4.37	0.25 $\pm$ 0.04	-0.82 $\pm$ 2.13
3	-2.69 $\pm$ 0.80	-2.76 $\pm$ 4.16	0.19 $\pm$ 0.03	-2.67 $\pm$ 1.84
4	0.25 $\pm$ 0.74	0.56 $\pm$ 4.37	0.17 $\pm$ 0.02	0.19 $\pm$ 1.38
5	-0.94 $\pm$ 1.05	-3.09 $\pm$ 4.07	0.37 $\pm$ 0.03	0.32 $\pm$ 3.05
6	0.86 $\pm$ 0.98	1.32 $\pm$ 3.81	0.37 $\pm$ 0.04	0.59 $\pm$ 2.90
7	-1.67 $\pm$ 0.72	-4.32 $\pm$ 4.25	0.16 $\pm$ 0.02	-1.17 $\pm$ 1.30
8	-0.49 $\pm$ 0.75	2.25 $\pm$ 3.90	0.18 $\pm$ 0.03	-1.09 $\pm$ 1.41
9	-1.82 $\pm$ 0.86	-0.20 $\pm$ 4.17	0.23 $\pm$ 0.04	-2.30 $\pm$ 1.87
10	-0.78 $\pm$ 0.77	1.27 $\pm$ 3.72	0.19 $\pm$ 0.03	-1.26 $\pm$ 1.44
Mirtot	-1.09 $\pm$ 0.26	-0.79 $\pm$ 1.28	0.21 $\pm$ 0.01	-1.15 $\pm$ 0.54

Table 6.15: Measured asymmetries before and after applying the correction described in Equation 6.17 on the entire data set.

Detector	A_{open}(PPM)	A_{closed}(PPM)	$R = \frac{S_{closed}}{S_{open}}$	A_Y(PPM)
1	-0.66 $\pm$ 0.86	2.67 $\pm$ 4.25	0.23 $\pm$ 0.01	-1.63 $\pm$ 1.71
2	-2.14 $\pm$ 1.01	-4.95 $\pm$ 4.72	0.26 $\pm$ 0.03	-1.17 $\pm$ 2.29
3	-2.64 $\pm$ 0.85	-2.73 $\pm$ 4.49	0.20 $\pm$ 0.04	-2.62 $\pm$ 1.75
4	0.024 $\pm$ 0.79	2.29 $\pm$ 4.74	0.17 $\pm$ 0.01	-0.45 $\pm$ 1.44
5	-1.11 $\pm$ 1.12	-3.15 $\pm$ 4.46	0.38 $\pm$ 0.01	0.13 $\pm$ 3.32
6	1.15 $\pm$ 1.05	4.12 $\pm$ 4.20	0.31 $\pm$ 0.01	-0.22 $\pm$ 2.52
7	-2.01 $\pm$ 0.77	-5.89 $\pm$ 4.58	0.17 $\pm$ 0.01	-1.22 $\pm$ 1.38
8	-0.69 $\pm$ 0.80	0.52 $\pm$ 4.20	0.19 $\pm$ 0.01	-0.98 $\pm$ 1.45
9	-1.54 $\pm$ 0.92	0.30 $\pm$ 4.50	0.24 $\pm$ 0.01	-2.13 $\pm$ 1.93
10	-0.83 $\pm$ 0.82	0.06 $\pm$ 4.03	0.20 $\pm$ 0.01	-1.04 $\pm$ 1.49
Mirtot	-1.08 $\pm$ 0.28	-0.52 $\pm$ 1.39	0.23$\pm$0.07	-1.22 $\pm$ 0.55

Table 6.16: Measured asymmetries before and after applying the correction described in Equation 6.17 on the data set *before* installing the lead curtain.

Detector	A_{open}(PPM)	A_{closed}(PPM)	$R = \frac{S_{closed}}{S_{open}}$	A_Y(PPM)
1	-6.51±2.39	-7.80 ± 10.52	0.18±0.03	-6.23±3.86
2	-2.26±2.74	-13.55±11.58	0.20±0.03	0.57±4.66
3	-3.03±2.34	-2.96±11.16	0.15±0.02	-3.04±3.52
4	1.93± 2.16	-10.09±11.76	0.14±0.02	3.83±3.27
5	0.34±3.09	-2.81±9.93	0.35±0.01	2.06±7.27
6	-1.33±2.87	-11.88±9.12	0.35±0.06	4.36±7.00
7	0.90±2.11	5.56± 11.47	0.14±0.01	0.16±3.08
8	1.21± 2.28	13.33± 10.63	0.16±0.01	-1.11± 3.43
9	-3.91±2.49	-3.14±11.00	0.18±0.03	-4.08±3.99
10	-0.46±2.29	8.50± 9.85	0.17±0.03	-2.24±3.53
Mirtot	-1.17 ± 0.77	-2.45 ± 3.35	0.20±0.08	-1.01 ± 1.23

Table 6.17: Measured asymmetries before and after applying the correction described in Equation 6.17 on the data set *after* the lead curtain was installed.

The asymmetry from elastically backscattered electrons (A_e) is calculated using the scintillation measurements described in Chapter 4. The measured detector yield ($Y_L = N_o - N_c$) may be written as a sum of the yield from elastic scattered electrons (Y_e) and non-elastic scattered electrons (Y_n). The asymmetry from elastically backscattered electron may then be written as

$$\begin{aligned} A_e &= \frac{(Y_L^+ - Y_n^+) - (Y_L^- - Y_n^-)}{(Y_L^+ - Y_n^+) + (Y_L^- - Y_n^-)} \\ &= \frac{\frac{Y_L^+ - Y_L^-}{Y_L^+ + Y_L^-} - \frac{Y_n^+ + Y_n^-}{Y_L^+ + Y_L^-}\frac{Y_n^+ - Y_n^-}{Y_n^+ + Y_n^-}}{1 - \frac{Y_n^+ + Y_n^-}{Y_L^+ + Y_L^-}} \\ &= \frac{A_L - FA_n}{1 - F} \end{aligned} \tag{6.18}$$

The ratio F is related to the scintillation measurements (s) appearing in Table 4.6 such that

$$F = 1 - s \tag{6.19}$$

The asymmetry (A_e) is again calculated by grouping the data set into two groups which correspond to before and after the lead curtain was installed (see Table 6.18). The weighted average of A_e^{bc} and A_e^{ac} in Table 6.18 is -1.64 $\pm$ 0.70 PPM which is comparable to the result in Equation 6.30 of Reference[50]. The uncertainty in this measurement is larger than in Equation 6.30 of Reference[50] due to a propagation of the uncertainty in the measured scintillation ratio (s) and the closed to open shutter ratio (R).

The final step to extracting the physics asymmetry is to account for the beam polarization. The average beam polarization throughout the entire data set using Table 6.14 is (34.4 $\pm$ 0.13 $\pm$ 1.6)%. The physics asymmetry becomes

$$A_{phy} = -4.77 \pm 2.05 \ PPM \tag{6.20}$$

after diluting A_e by the incident electron beam polarization using the systematic absolute uncertainty of 1.6% in the beam polarization measurement.

Det.	s^{bc}(%)	A_Y^{bc}(PPM)	A_e^{bc}(PPM)	s^{ac}(%)	A_Y^{ac}(PPM)	A_e^{ac}(PPM)
1	72.7 $\pm$ 5.0	-1.63 $\pm$ 1.71	-2.24 $\pm$ 2.35	78.3 $\pm$ 4.0	-6.23 $\pm$ 3.86	-7.96 $\pm$ 4.95
2	68.7 $\pm$ 6.9	-1.17 $\pm$ 2.29	-1.70 $\pm$ 3.33	75.0 $\pm$ 5.0	0.57 $\pm$ 4.66	0.76 $\pm$ 6.21
3	72.7 $\pm$ 5.0	-2.62 $\pm$ 1.75	-3.60 $\pm$ 2.42	78.3 $\pm$ 4.0	-3.04 $\pm$ 3.52	-3.88 $\pm$ 4.50
4	67.9 $\pm$ 5.5	-0.45 $\pm$ 1.44	-0.66 $\pm$ 2.11	74.6 $\pm$ 4.2	3.83 $\pm$ 3.27	5.13 $\pm$ 4.39
5	73.6 $\pm$ 4.8	0.13 $\pm$ 3.32	0.18 $\pm$ 4.60	77.6 $\pm$ 2.9	2.06 $\pm$ 7.27	2.65 $\pm$ 9.35
6	73.6 $\pm$ 4.8	-0.22 $\pm$ 2.52	-0.30 $\pm$ 3.44	77.6 $\pm$ 2.9	4.36 $\pm$ 7.00	5.62 $\pm$ 9.03
7	67.9 $\pm$ 5.5	-1.22 $\pm$ 1.38	-1.80 $\pm$ 2.04	74.6 $\pm$ 4.2	0.16 $\pm$ 3.08	0.21 $\pm$ 4.04
8	72.7 $\pm$ 5.0	-0.98 $\pm$ 1.45	-1.34 $\pm$ 1.98	78.3 $\pm$ 4.0	-1.11 $\pm$ 3.43	-1.42 $\pm$ 4.39
9	68.7 $\pm$ 6.9	-2.13 $\pm$ 1.93	-3.10 $\pm$ 2.83	75.0 $\pm$ 5.0	-4.08 $\pm$ 3.99	-5.44 $\pm$ 5.33
10	72.7 $\pm$ 5.0	-1.04 $\pm$ 1.49	-1.43 $\pm$ 2.05	78.3 $\pm$ 4.0	-2.24 $\pm$ 3.53	-2.86 $\pm$ 4.51
Ave.		-1.22 $\pm$ 0.55	-1.71 $\pm$ 0.78		-1.01 $\pm$ 1.23	-1.35 $\pm$ 1.60

Table 6.18: The asymmetry from elastically backscattered electrons under the assumption that the non-elastic asymmetry A_n is zero. The superscript bc (ac) refers to measurements made before (after) the lead curtain was installed.

To account for internal and external bremsstrahlung processes that result in energy loss (see Figure 4.6), the physics asymmetry is increased by 1.094 ± 0.01[50] This value represents the calculated ratio of the asymmetry calculated at tree level (Equation 2.35) to an asymmetry which includes contributions from external and internal radiative tails. The external radiative correction is from the incident electron energy loss caused by bremsstrahlung production by the incident electron as it traverses the target and before it interacts with a proton that will backscatter the electron into the detector acceptance. Additionally, the electron spin may flip as a result of generating bremsstrahlung radiation. The internal radiative correction is estimated by calculating the asymmetry resulting from the coherent emission of a real photon while the electron is backscattered from the proton. The physics asymmetry is [5]

$$A_{phy} = -5.22 \pm 2.24 \ \ (PPM). \tag{6.21}$$

[5]This asymmetry agrees with the value of -7.38 ± 2.12 reported in Reference [58]. The uncertainty reported here is larger due to the inclusion of uncertainties in the shutter closed asymmetry and the scintillation measurements.

Step	Before Curtain	After Curtain
A_{cor}	-1.08 $\pm$ 0.28	-1.17 $\pm$ 0.77
A_Y	-1.22 $\pm$ 0.55	-1.01 $\pm$ 1.23
A_e	-1.71 $\pm$ 0.78	-1.35 $\pm$ 1.60
	Average	
A_e	-1.64 $\pm$ 0.70	
$A^{pol}_{dilution}$	-4.77 $\pm$ 2.05	
A^{rad}_{cor}	-5.22 $\pm$ 2.24	

Table 6.19: Summary of the steps taken to arrive at the physics asymmetry A_{phys}. The asymmetry corrected for position fluctuations is labeled as A_{cor}, the asymmetry in the detector yield is denoted as A_Y, A_e represents the asymmetry is the elastic contribution to the detector yield, accounting for the extent of incident electron polarization is denoted as $A^{pol}_{dilution}$ and A^{rad}_{cor} labels the asymmetry after making radiative corrections.

Source	Contribution (PPM)
Pedestal Asymm	0.20
PITA	0.10
PMT non-linearity	0.24
ADC non-linearity	0.03
Beam corrections	0.47
Radiative correction	0.05
Polarization	0.24
Mott Asymm	0.02

Table 6.20: Contributions to the systematic uncertainty in the measured asymmetry A_{phys} in Equation 6.21.

Chapter 7

Results and Conclusions

7.1 Physical Observables

7.1.1 The Weak Magnetic Form Factor G_M^Z

Equation 2.42 may be used to directly extract the weak magnetic form factor of the proton (G_M^Z) using the measured physics asymmetry A_{phys} in Equation 6.21. Unfortunately, the same weak radiative corrections made when extracting G_M^s must also be considered for $G_M^{Z,p}$. Using Equation 2.50, the radiatively corrected weak magnetic form factor $\tilde{G}_M^Z$ can be cast as a sum of electromagnetic form factors and the physical weak magnetic form factor G_M^Z as

$$\begin{aligned} \tilde{G}_M^{Z,p}(q^2) &= G_M^{Z,p}(q^2) \\ &+\frac{1}{4}\left[(1-4\sin^2\theta_W)R_V^p G_M^{\gamma,p}(q^2) - R_V^n G_M^{\gamma,n}(q^2) - R_V^{(0)} G_M^s(q^2)\right] \end{aligned} \tag{7.1}$$

Using the radiative correction values in Table 2.3 and the magnetic form factors in Table 2.4, the correction term in brackets above becomes to $5.54 \pm 9.38 \times 10^{-3}$. Neglecting the weak radiative corrections to $G_M^{Z,p}$, the measured physics asymmetry in Equation 6.21 yields

$$G_M^{Z,p}(0.1GeV^2/c^2) = 0.298 \pm 0.156 \pm 0.044 \pm 0.024 \ \mu_N. \tag{7.2}$$

This result is consistent with the value of 0.34 ± 0.09 reported in Reference [58] and 0.305 ± 0.095 reported in Reference [50]. The uncertainty is larger in this work due to considerations of the shutter closed asymmetry and the uncertainty in the Čerenkov contribution to the detected signal.

7.1.2 The Strange Quark Contribution to the Proton Magnetic Form Factor G_M^s

Equation 2.54 is used to determine the form factor G_M^s from the measured asymmetry. Using the physics asymmetry in Equation 6.21, the contribution of strange quarks to the proton magnetic form factor at $Q^2 = .1\ GeV^2/c^2$ is

$$G_M^s(Q^2 = 0.1\ GeV^2/c^2) = \frac{A_{ep} - 6.99 \pm 2.01)}{3.59} \tag{7.3}$$

$$= \frac{(-5.22 \pm 2.24) + 6.99 \pm 2.01)}{3.59} \tag{7.4}$$

$$= 0.49 \pm 0.62 \pm 0.17 \pm 0.095\ \mu_N \tag{7.5}$$

This value is consistent with the value of $+0.23 \pm 0.37$ reported in Reference [58]. The uncertainty in this analysis is larger due predominantly to the inclusion of the shutter closed uncertainty. Predictions of this form factor using several theoretical models are shown in Table 7.2. An experiment using a neutrino probe instead of an electron probe reported[24] a determination of this form factor which is consisted with zero but opposite in sign to the value in Equation 7.5. The SAMPLE experiment is expecting to improve the precision in this result by taking more data in the near future.

7.1.3 Quark-antiquark Form Factors

All three magnetic quark-antiquark form factors may be extracted using the the description of nucleon currents which forms the basis of the system of equations in Equation 2.29. The electric quark-antiquark form factors may also be extracted in an analogous fashion. Solving Equation 2.29 for each quark type lead to the set of equations

$$G_M^u = (3 - 4\sin^2(\theta_W))G_M^{\gamma,p} - 4G_M^{Z,p} \tag{7.6}$$

$$G_M^d = (2 - 4\sin^2(\theta_W))G_M^{\gamma,p} + G_M^{\gamma,n} - 4G_M^{Z,p} \tag{7.7}$$

$$G_M^s = (1 - 4\sin^2(\theta_W))G_M^{\gamma,p} - G_M^{\gamma,n} - 4G_M^{Z,p} \tag{7.8}$$

The quark-antiquark form factors in Table 7.1 result when the value of G_M^Z in Section 7.1.1 is used with the above set of equations. Taken individually, if the quark and anti-quarks were described by the same wave function but have their spins aligned with respect to each other, then no net contribution of the quark-anti-quark pairs would be expected. If, however, their spins were anti-parallel a large contribution would be expected.

Form Factor	Measured (μ_N)	SU6 (μ_N)
G_M^u	3.01 $\pm$ 0.66	3.67
G_M^d	-0.62 $\pm$ 0.49	-1.03
G_M^s	0.49 $\pm$ 0.83	0

Table 7.1: Quark-antiquark form factors extracted using the measured value of G_M^Z

7.2 Theoretical Predictions

Table 7.2 shows several predicted values of G_M^s using various models of the nucleon [1]. The "Poles" model[59, 60] , named for the singularities (poles) at timelike q^2 in the Dirac ($F_1(q^2)$) and Pauli ($F_2(q^2)$) form factors shown in Chapter 2 which correspond to the coupling of iso-vector states to the nucleon, find the dominant contribution to the predicted values of G_M^s in Table 7.2 are attributed to the coupling of a ϕ meson to the proton. The "Kaon Loops" model [62, 63, 64, 65] considers fluctuations of the proton into hyperon-kaon states ($\Lambda K, \Sigma K, \Sigma^* K$) as the source of the proton strangeness content. Other calculations using some traditional and some more recent models are also shown in Table 7.2.

Charge symmetry and Pion contributions to G_M^s are two issues that have been addressed to substantiate a comparison of the measurement with theory. The underlying assumption made in Chapter 2 is that the distribution of u and $\bar{u}$ quarks in the proton is identical to the distribution of d and $\bar{d}$ in the neutron. Likewise

[1] The models and the analysis in this thesis use the sign convention of Reference[59] in which the strange quark has positive strangeness. This sign convention is opposite to Reference[22].

Model	G_M^s	Reference
Poles	-0.31 ± 0.009	[59]
Poles	-0.24 ± 0.03	[60]
Kaon Loops	±0.8	[62]
Kaon Loops	-0.026	[63]
Kaon Loops	-0.40→-0.31	[64]
Kaon Loops	+0.035	[65]
Loops &Poles	-0.31 ± 0.009	[61]
SU(3) Skyrme	-0.33 →-0.13	[66]
Chiral Hyperbag	+0.43 ± 0.30	[67]
Chiral Color Dielectric	-0.40→-0.03	[68]
Constituent Quark	-0.13 ± 0.01	[69]
QCD Equalities	-0.73 ± 0.30	[70]

Table 7.2: Predicted values for G_M^s

the distribution of d and $\bar{d}$ quarks in the proton is identical to the distribution of u and $\bar{u}$ quarks in the neutron. Some justification for this assumption can be made by determining the level of charge symmetry in the proton system. There is also one work which suggests that the measurement made should be diluted to account for the pion contribution that is generated by small Charge Symmetry violations.

7.2.1 Charge Symmetry

Under charge symmetry, the wave function used to describe $u(d)$ quarks in the proton will also describe $d(u)$ quarks in the neutron. This symmetry justifies the substitution of $G_M^{d,p}$ for $G_M^{u,n}$ and $G_M^{u,p}$ for$G_M^{d,n}$ in Equation 2.29. If charge symmetry holds

$$\langle p', S'|\bar{u}\gamma^\mu u - \bar{d}\gamma^\mu d|p, S\rangle \quad = \quad J_p^\mu(Q^2) - J_n^\mu(Q^2) + \Delta x^\mu \qquad (7.9)$$

is an exact equality where Δx^μ is zero. In the event of charge symmetry breaking, equation 7.9 requires the correction term Δx^μ to maintain the equality. Using a non-relativistic quark model, the impact of the correction term Δx^μ on the electric and magnetic form factors is at most 1% for G_E and G_M at the highest Q^2 where such models are considered valid while at $Q^2 = 0.1$ GeV^2/c^2 (where the measurements in this thesis are made) the correction term is less than 0.1% of the magnetic form factor[71].

7.2.2 Pion Contribution to G_m^s resulting from Iso-spin Breaking

The theoretical work of Reference[72] suggests that the extracted form factor G_M^s be reduced by 35 to 52%. Under the assumption that the exchanged boson (photon or Z) interacts predominantly with the pion component of a nucleon, the work considers contributions of the $\bar{u}$ and $\bar{d}$ momentum differences to the proton form factors. These differences arise from the fluctuation of a proton into either a neutron and π^+ or a Δ^{++} and a π^- in a manner analogous to the kaon fluctuations considered in the previous section. The resulting charge symmetry violations within this framework result in form factor contributions on the order of 0.2% (comparable to that found in Reference[71]). The work concludes that the size of pion cloud effects are comparable to the kaon cloud effects at the Q^2 measurement in this thesis but the contributions of each at higher Q^2 will be different due to their mass differences.

7.3 Future Directions

Several experimental efforts are underway to both improve the current measurement and to extend the measurement to higher values of Q^2. The SAMPLE experiment at MIT Bates will continue to accumulate data to decrease the measured uncertainty. The collaboration will also use a deuterium target in place of the hydrogen target to reduce the axial radiative correction uncertainty which dominates the model dependent uncertainty. The A4 collaboration at Mainz with measure a linear combination of the strange quark vector form factors (G_E^s and G_M^s) at a Q^2 of 0.225 GeV^2/c^2). Three experiments (E91-004, E91-010, and E91-017) are also planned at the Thomas Jefferson National Accelerator Facility. Experiment E91-004 will measure an asymmetry sensitive to G_E^s at a Q^2 of 0.6 (GeV^2/c^2) using ^4He. Experiment E91-010 will measure a linear combination of the vector strange quark form factors (G_E^s, G_M^s) and the electric form factor of the neutron $G_E^{\gamma,n}$ over the Q^2 range $0.3 \rightarrow 0.7$ (GeV^2/c^2). Experiment E91-017 will undertake measurements of G_E^s and separately G_M^s over a Q^2 range of $0.1 \rightarrow 1.0$ (GeV^2/c^2) using a dedicated toroidal spectrometer.

7.4 Conclusions

The first measurement of the proton weak magnetic form factor G_M^Z has been made using parity-violating, elastic $^1H(e,e)$ scattering at a momentum transfer of $Q^2 = 0.1$ GeV^2/c^2). A measured physics asymmetry of

$$A_{phys} \quad = \quad (-5.22 \pm 2.24 \pm 0.62) \times 10^{-6}$$

corresponds to a measured weak magnetic form factor of

$$G_M^Z(Q^2 = 0.1GeV^2/c^2) \quad = \quad 0.298 \pm 0.156 \pm 0.044 \pm 0.024 \ \ \mu_N.$$

The first uncertainty is statistical, the second is systematic contributions from the measurement and the third uncertainty is the contribution from the uncertainty in theoretical calculations of weak radiative corrections. The strange quark contribution to the proton magnetic form factor (G_M^s) has been determined from the weak magnetic form factor. After applying model dependent radiative corrections, the value determined is

$$G_M^s(Q^2 = 0.1GeV^2/c^2) \quad = \quad 0.49 \pm 0.62 \pm 0.17 \pm 0.10 \ \ \mu_N.$$

The measured value of G_M^s does not differentiate from zero. It is anticipated that the planned supplemental increase in the data set will decrease the uncertainty by a factor of two and improve the experimental precision of G_M^s.

References

[1] J. J. Friedman and H.W. Kendall, Ann. Rev. Nucl. Sci. **22**, 203 (1972).

[2] H. Abramowicz *et al.*, Z. f. Phys. **C15**, 19 (1982).

[3] A.O. Bazarko *et al.*, Z. Phys. **C65**,189 (1995).

[4] J. Ashman et al.,Phys. Lett. **B206**, 364 (1988); *ibid* Nucl. Phys. **328**, 1 (1989); M.J. Alguard et al., Phys. Rev. Lett. **37**, 1261 (1976); *ibid*, **41**, 70 (1978); G. Baum et al., Phys. Rev. Lett. **51**, 1135 (1983); B. Adeva et al, Phys. Lett. **B302**, 533 (1993); D.L. Anthony et al., Phys. Rev. Lett. **71**, 959 (1993). K. Abe et al., Phys. Rev. Lett. **74**,346 (1995)

[5] E. Reya, Rev. Mod. Phys. **46**, 545 (1974).

[6] Francis Halzen and Alan D. Martin, *Quarks & Leptons* John Wiley & Sons, New York (1984).

[7] J. Gasser etal., Phys. Lett. **B253**, 252 (1991).

[8] R. Koch, Z. Phys. **C15**, 161 (1982).

[9] C.A. Dominguez and Paul Langacker, Phys. Rev. **D24**, 1905 (1981).

[10] J. Ellis and R.L. Jaffe, Phys. Rev. **D9**, 1444 (1974).

[11] J. Ashman *et al.*, Nucl. Phys. **B328**, 1 (1989)

[12] F.E. Close and R.G. Roberts, Phys. Rev. Lett. **60**, 1471 (1988).

[13] John Ellis and Marek Karliner, Phys. Lett. **B341**, 397 (1995).

[14] M.N. Rosenbluth, Phys. Rev. **79**, 615 (1950).

[15] G. Hohler, Nucl. Phys. **B114**, 505 (1976).

[16] G.G. Simon *et al.* Nucl. Phys. **A333**, 381 (1980).

[17] R.W. Berard *et al.* , Phys. Lett. **B47**, 355 (1973).

[18] F.A. Bumiller *et al.*, Phys. Rev. Lett. **25**, 1774 (1976).

[19] A.S. Esaulov *et al.*, Sov. J. Nucl. Phys. **45**, 258 (1987).

[20] P. Markowitz *et al.*, Phys. Rev **C**, R5 (1993).

[21] A. Lung *et al.*, Phys. Rev. Lett. **30**, 718 (1993).

[22] Particle Data Group, L. Montanet *et al.*, Phys. Rev. **D50**, 1173 (1994).

[23] D.B. Kaplan and A. Manohar, Nucl. Phys. B310, 527 (1988). D.H. Beck, Phys. Rev. **D39**, 3248 (1989).

[24] G. T. Garvey, W. C. Louis, and D. H. White, Phys. Rev. **C48**, 761 (1993).

[25] E. Reya and K. Schilcher, Phys. Rev. **D3**, 952 (1974);

[26] Robert N. Cahn and Fredrick J. Gilman, Phys. Rev. **D17**, 1313 (1978).

[27] M.J. Musolf and B.R. Holstein, Phys. Lett. **B242**, 461 (1990).

[28] M. J. Musolf *et al.*, Physics Reports **239**, 1 (1994).

[29] M.J. Musolf and T.W. Donnelly, Nucl. Phys **A546**, 509 (1992).

[30] Using a weighted average of -0.194 $\pm$ 0.046[11] and -0.15 $\pm$ 0.09[32]

[31] R.M. Barnett *et al.*,Phys. Rev. **D54**, 1 (1996).

[32] L. A. Ahrens *et al.*,Phys. Rev. **D35**, 785 (1987).

[33] Bates Polarized Injector Review, March 28-30 (1996).

[34] Conoptics, Inc. 19 Eagle Rd. Danbury, CT 06810-4044 Phone: (203) 743-3349, (800)748-3349.

[35] J.D.Jackson,*Classical Electrodynamics*, Second Edition, Wiley, New York, 559 (1975).

[36] J. Arrington *et al.*, Nucl. Inst. and Meth. **A311**, 39 (1992).

[37] A.A. Kresnin and L.N. Rosentsveig, J. Exp. Theor. Phys. (USSR) **32**, 353 (1957).

[38] Supermendur Manufacturer, National-Arnold Magnetics, 17030 Muskrat Avenue, Adelanto, Cal. 92301.

[39] M. Pitt, Internal Collaboration report.

[40] L.G. Levchuck, Nucl. Instr. and Meth. **A345**, 496 (1994).

[41] SLAC Blue Book

[42] Process Systems International, 20 Walkup Dr., Westford, MA (formerly Koch Process Systems, Inc.

[43] E.J. Beise *et al.*, Nucl. Instr. and Meth. **A378**, 383 (1996).

[44] K. Kumar, Syracuse University Ph.D. thesis (1990), unpublished.

[45] CERN Program Library Office , CERN-CN Division , CH-1211 Geneva 23 , Switzerland

[46] J.F. Ziegler, Nucl. Inst. and Meth., **191**, 419 (1981).

[47] R.L. Walker, Phy. Rev. **182 # 5**, 1969, 1729 (1969).

[48] Bergstron *et al.*, Phys. Rev. **C53 #3**, R1052 (1996).

[49] Seonho Choi *et al.*, Phys. Rev. Lett. **71 #24**, 3927 (1993).

[50] B.A. Mueller, Ph.D. Thesis , Caltech, (1997).

[51] S.P. Li, E. M. Henly, and W-Y.P. Hwang, Ann. Phys. **143**, 372 (1982)

[52] Digital, 111 Powdermill Road ,Maynard, MA, 01754-1418, phone (978) 493-5111

[53] N.F. Mott, Proc. Roy. Soc. **A135**, 429 (1932).

[54] Robert W. Michaels, Yale University Ph.D. thesis (1988), unpublished.

[55] P. R. Bevington *Data Reduction and Error Analysis for the Physical Sciences*, McGraw-Hill, New York, 164 (1969).

[56] William H. Press *Numerical Recipes, The Art of Scientific Computing*, Cambridge University Press, New York, (1986)

[57] Clinton P. Anderson Meson Physics Facility(LAMPF), Los Alamos National Laboratory, Los ALamos, New Mexico, 87545

[58] B. Mueller *et al.*, Phys. Rev. Lett. **78**, 3824 (1997).

[59] R. L. Jaffe, Phys. Lett. **B229**, 275 (1989).

[60] H.W. Hammer, U-G Meissner and D. Dreschel, Phys. Lett. **B367**, 323 (1996).

[61] T. Cohen, H. Forkel, M. Nielsen, Phys. Lett. **B316**, 1 (1993).

[62] B. R. Holstein, *Proceedings of the Caltech Workshop on Parity Violation in Electron Scattering*, E. J. Beise and R. D. Mckeown (Ed.) , World Scientific, Singapore, 27 (1990).

[63] W.Koepf, E. M. Henly and S. J. Pollock, Phys. Lett. **B288**, 11 (1992).

[64] M. J. Musolf and M. Burkardt, CEBAF Theory Preprint Nr. TH-93-01.

[65] P. Geiger and N. Isgur, Phys. Rev. **D55**, 299 (1997).

[66] N. W. Park, J. Schechter and H. Weigel, Phys. Rev. **D43**, 869 (1991).

[67] S. Hong and B. Park, Nucl. Phys. **A561**, 525 (1993).

[68] S.C. Phatak and S. Sahu, Phys. Lett. **B321**, 11 (1994).

[69] H. Ito, Phys. Rev. **C52**, R1750 (1995).

[70] D. Leinweber, Phys. Rev. **D53**, 5115 (1996).

[71] Gerald A. Miller, e-print nucl-ph/9711036 at http://xxx.lanl.gov.

[72] Simon Capstick and D. Robson, Florida State University preprint FSU-SCRI-97-96.

[73] Thorn EMI Electron Tubes Inc, 100 Forge Way Unit F, Rockaway, NJ, 07866, USA, Tel: (201) 586-9594 , Fax: (201) 586-9771 , Toll Free (800) 521-8382.

[74] A.G. Wright, IEEE Transactions on Nuclear Science, **Ns-34 No. 1**, 414 (1987).

[75] N.Carleton, *Methods of Experimental Physics* **12**, Part A, 35 (1965).

[76] B. Bencheikh, Nucl. Inst. and Meth. **A315**, 349 (1992).

[77] A.H. Rosenfeld, Ann. Rev. Nucl. Sci. **25**, 555 (1975).

Appendix A

Čerenkov Detector Calibration

The gain of all ten photomultiplier tubes (PMT) used in the SAMPLE detector is measured as a function of the high voltage applied to the dynode chain. Measurements were taken at the University of Illinois Nuclear Physics Lab (NPL) in Champaign Illinois and at the MIT Bates Laboratory in Middleton Massachusetts over several years. The low noise environment at NPL permitted an investigation of the statistical method used to extract the PMT gain. Measurements at MIT Bates are done in a higher noise environment compared to NPL and require a modified statistical method to measure the PMT gain.

A.1 The Photomultiplier Detector

Figure A.1 illustrates the general features of the PMT and the pinout labels of each dynode stage. The phototubes are type #D642 manufactured by Thorn EMI Electro Tubes Ltd[73]. The front detector window is an eight inch diameter hemisphere of Borosilicate glass (Pyrex). A semi-transparent layer of antimony, cesium, and rubidium (biakali) is deposited on the inside surface of the hemisphere to form the photocathode of the detector. The average efficiency of the detectors is 19.7% over wavelengths of 300 to 600 nm.

Figure A.2 is a schematic of the dynode chain along with the components used to define the voltage divider network that establishes potential differences at each stage of the dynode chain. Table A.1 lists the values of each component and Table A.2 lists

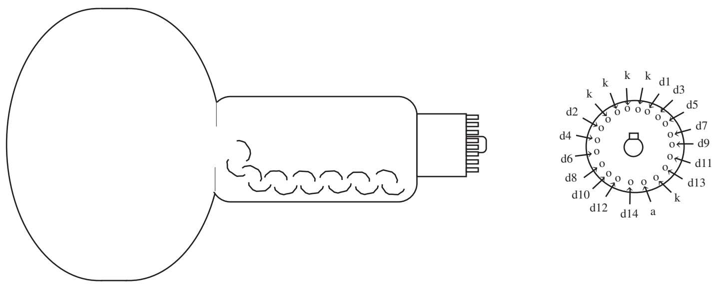

Figure A.1: Photomultiplier tube used in the SAMPLE experiment.

the measured potential at each stage of the base, in the static (unloaded) limit, for each PMT detector. Photoelectrons are lost between dynode stages when the number of photoelectrons reaches a density that prevents the potential difference across a stage from accelerating them to the next stage (space-charge limit). To decrease the impact of this space-charge limit, the zener diodes (components R_{k-1}, R_{13-14}, and R_{14-g} in Figure A.2) prevent the voltage across those stages from being influenced by the load at other stages and improve the transmission of more photoelectrons down the dynode chain.

A loss of photoelectrons is seen as an exponential decrease in the current output at the anode during the light pulse. Strobing the incident light at the SAMPLE operating point (2.4×10^6 photons/sec) has shown base #4 to sustain a current without the loss described above until the tube has a gain greater than 10^7 (or about 1500 volts).

Figure A.3 is a schematic for the preamplifier used to convert the dynode chain output current to a voltage which is impedance matched to the integrator electronics used in data acquisition (see Figure 3.15). The preamplifier saturates after 1mA and has a measured conversion coefficient of 1mA/10Volts. One hour is required for the circuitry to reach thermal equilibrium, once the device is turned on, due the heat produced by the preamplifier.

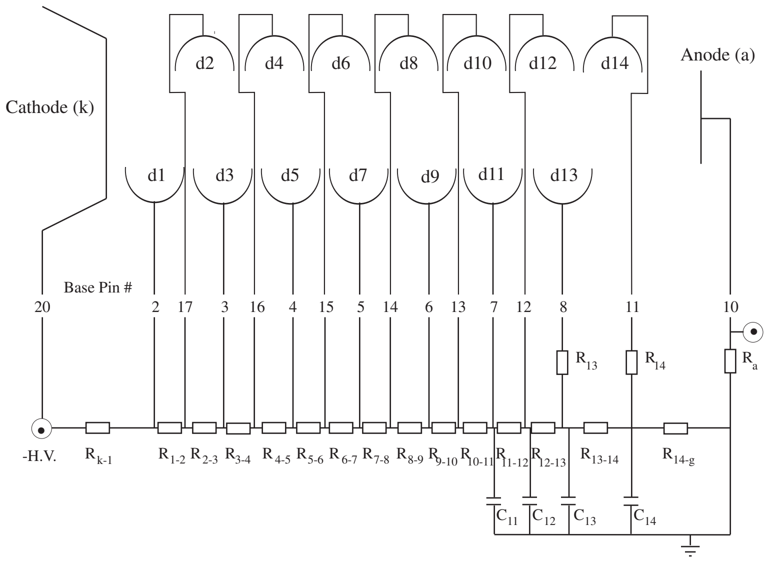

Figure A.2: General Schematic of the PMT base and components.

A.2 Gain Measurements at University of Illinois

A.2.1 Apparatus

A BNC light pulse generator (Model 6010) is used as a photon source to illuminate the photomultiplier detectors with light of wavelength 5600 Å. The PMT current at the anode was measured by a charge sensing ADC (LeCroy 2249 W) with a sensitivity of 0.25 pC/Channel. A determination of the ADC pedestal (the charge on the ADC capacitor when light is absent) was found by reading (gating) the ADC in between intervals of illuminating the PMT. This is done by triggering the BNC pulse generator at half the gate frequency. The pedestals before and after the emission of light are averaged and then subtracted from the signal point by point. By controlling the amount of light incident on the photocathode it is possible to measure signals caused by the emission of multiple photoelectrons and a single photoelectron. Multiple photoelectron measurements are made by shining light directly on the photocathode. Single photoelectron measurements can be made by decreasing the light intensity and reflecting it off a cardboard surface which has been painted black. Single photoelectron

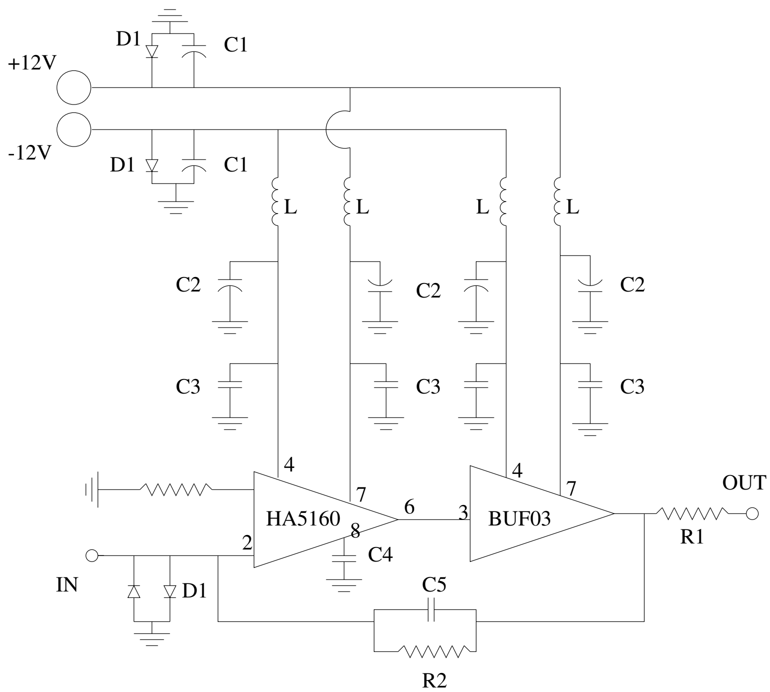

Figure A.3: Schematic of the PMT preamplifier.

measurements illuminated the PMT for a duration of 0.5μsec. Multiple photoelectron measurements were made by illuminating the photocathode for a duration of 5μsec producing a rate of photoelectrons on the order of the rate present in the SAMPLE experiment $(2.4 \times 10^6 \frac{events}{sec})$.

Operating the BNC light pulse generator (Model 6010) in stabilized mode to measure multiple photoelectron events caused fluctuations in the calculated number of photoelectrons which were much larger than 8% for $N_{pe} \leq 2000$. Visual inspection of the signal on an oscilloscope revealed a ringing within the first 2 μsec of the pulse which can be attributed to the process of light stabilization by means of a feedback loop. Stabilized mode was observed to increases the PMT photocurrent by 30% compared to high speed mode. Operating the light pulser in high speed mode eliminates the ringing effect and allows measurements verifying the above equation to the 8% level.

Component #	Base #4
R_{k-1}	6×100 Volt Zener
R_{1-2}	2×33 kΩ
R_{2-3}	33 kΩ
R_{3-4}	33 kΩ
R_{4-5}	33 kΩ
R_{5-6}	33 kΩ
R_{6-7}	33 kΩ
R_{7-8}	33 kΩ
R_{8-9}	33 kΩ
R_{9-10}	33 kΩ
R_{10-11}	33 kΩ
R_{11-12}	33 kΩ
R_{12-13}	2×33 kΩ
R_{13-14}	75 Volt Zener
R_{14-g}	100 Volt Zener
R_{13}	150 Ω
R_{14}	150 Ω
R_a	1 MΩ
C_{11}	.01 μ F
C_{12}	.01 μ F
C_{13}	.1 μ F
C_{14}	.1 μ F

Table A.1: Voltage Divider components for the Base types.

A.2.2 Data Analysis

The ability to change the BNC pulse generator output permits a determination of the phototube gain over a large high voltage range. The voltage region in which both single and multiple photons are measured was used to normalize the multiple photoelectron gain measurements and obtain an absolute gain measurement. This normalization is done using a relationship between the peak width and centroid of the single and multiple photoelectron signal [74]. The standard deviation (σ_{se}) of the single photoelectron centroid (C_{se}) is related to the standard deviation (σ_{me}) of the multiple photoelectron centroid (C_{me}) and the number of photoelectrons N_{pe} such

Dynode Stage Pins	4A	Δ 4G	V_{a-c} 4N	(Volts) 4L	of 4E	Base 4H	# 4I	4M	4K	4F
20-2	597	589	596	592	588	582	596	594	595	601
2-17	98	114	99	100	114	109	100	99	114	113
17-3	49	57	49	49	56	54	49	49	56	56
3-16	49	56	49	49	56	54	49	49	56	56
16-4	49	57	49	49	56	54	49	49	56	56
4-15	49	56	49	49	57	54	49	50	56	56
15-5	49	56	48	49	56	54	49	49	56	56
5-14	48	56	49	49	56	54	49	49	56	56
14-6	49	56	48	48	56	54	49	49	56	56
6-13	48	56	49	49	56	54	49	49	56	56
13-7	49	56	48	48	56	54	49	48	56	55
7-12	73	85	73	73	85	81	74	73	85	83
12-8	98	111	97	97	111	108	97	97	111	110
8-11	73	72	73	73	72	75	72	79	72	72
11-10	98	99	101	101	100	100	96	100	100	99
total	1476	1576	1477	1475	1575	1541	1476	1483	1581	1581

Table A.2: Measured potential differences at each dynode stage for the different type #4 Bases set to give the same detector gain.

that

$$(\frac{\sigma_{me}}{C_{me}})^2 = \frac{1}{N_{pe}}[1 + (\frac{\sigma_{se}}{C_{se}})^2]. \tag{A.1}$$

This equation is entirely based upon the statistics of the single photoelectron measurement Poisson distribution. Assuming Poisson statistics, the standard deviation is related to the number of counts such that

$$\frac{\sigma}{\bar{x}} = \frac{1}{\sqrt{N}}.$$

As the number of photoelectrons increases the Poisson distribution becomes Gaussian. In the case of the multiple photoelectron measurements, there is a width (error) to a single photoelectron event which should be propagated. The standard technique of error propagation is to sum the squares of the multiple photoelectron error and the

Component #	Base #4
R1	50 Ω
R2	10 kΩ 1%
C1	6.8 μ F
C2	3.7 μ F
C3	.1 μ F
C4	20 pF
C5	12 pF
D1	1N914
L	1 μ H

Table A.3: Components for PMT base preamplifier circuit.

scaled single photoelectron error.

$$(\frac{\sigma_{me}}{C_{me}})^2 = \frac{1}{N_{pe}} + \frac{1}{N_{pe}} \times (\frac{\sigma_{se}}{C_{se}})^2$$

There are many sources of error in gain measurements of the PMT simply because the photomultiplier behavior changes as a function of temperature, amount of light, etc. Besides the usual dark current (which is minimized in these measurements), the voltage across each dynode stage varies as a function the number of electrons accelerated within the dynode (dynode loading). Another source of signal variation involves the ejection of the photoelectron. While it is inherently assumed that an ejected photoelectron will be directed towards the next dynode in the chain, a 5% photoelectron loss at each stage of the base is statistically possible (see Reference [75]).

A.2.3 Single Photoelectron Measurements

The PMT gain is directly proportional to the anode current when only one photoelectron is generated by the incident light on the photocathode. Using the apparatus described in section A.2.1, the centroid of the single electron spectrum (C_{se}) is related to the PMT gain by

$$Gain\ (se) = \frac{C_{se} \times 10^8}{64}. \tag{A.2}$$

Two extremes of the PMT single photoelectron photocurrent spectrum are shown in Figure A.4 along with background measurements made by turning the light pulser off. Figure A.4.a shows the photocurrent created by the light pulser along with an overlay of the background occurring when the light pulser is turned off as measured during equal time intervals. Figure A.4.b, on the other hand, shows the appearance of a single photoelectron signal if the background is measured for a very long duration. This signal is probably due to thermal excitations in the photocathode. As a result there is some ambiguity introduced to the measurement of the centroid for these distributions.

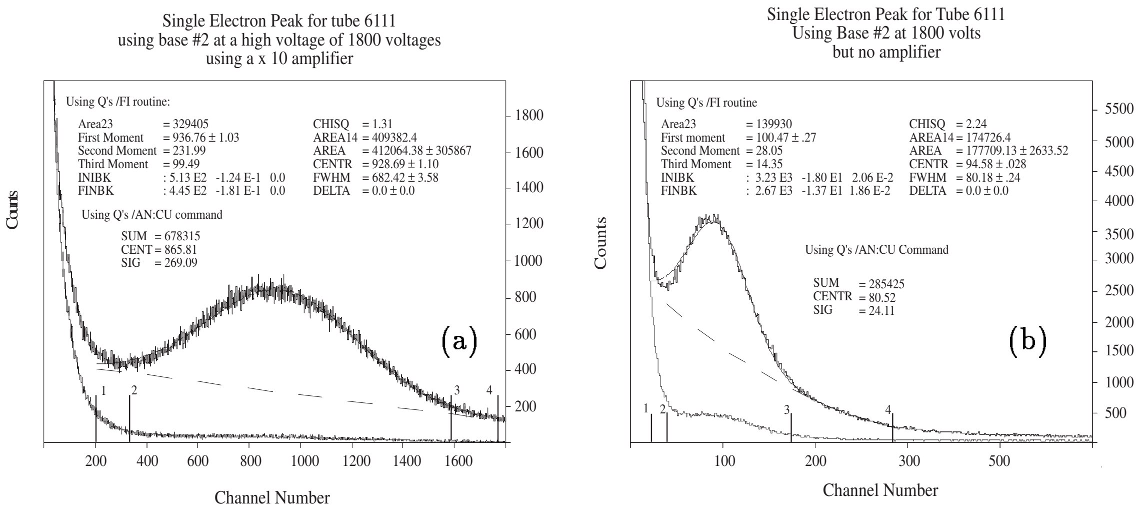

Figure A.4: Single photoelectron events using Thorn EMI (type #D642, ser. #6111) photomultiplier tube and Base #2. and a ten fold current amplifier are used to measure the PMT current at 1800 volts. The background appears in the lower histogram of each figure. The third order polynomial used to approximate the background is shown as a dashed line and the Gaussian resulting from background subtraction is given as a solid line. The only differences between (a) and (b) are the elapsed time data was taken and the presence of a ten fold current amplifier.

A measurement of the single photoelectron centroid using three different methods was done to resolve the ambiguity of measuring a PMT centroid. The simplest way to measure a centroid is to average the counts within a selected region believed to contain the samples relevant to the desired signal (method SIMPLE). A second technique is to account for the noise in the system by subtracting the measured noise from the measured signal and fitting the result to a Gaussian distribution (method PARTICLE). The third technique considered is to assume that the background resulting from the above signal variations scales with the actual signal. A third order polynomial fit to the spectrum outside the peak is used to approximate the background. A Gaussian is then fit to the spectrum after subtracting the third order polynomial (method PHOTO). The above three techniques are used the analyze the current collected by the 8 inch diameter phototube manufactured by Thorn EMI (type #D642, ser. #6111).

Figure A.4a represents a spectrum due to single photoelectron events analyzed using method SIMPLE and method PHOTO. A measurement of the background (light pulser off) taken for the same time interval is overlayed on the actual signal. The subtraction of this background from the spectrum results in a Gaussian distribution (see Figure A.5) with a centroid comparable to using the method SIMPLE within 1%. Method PHOTO however tends to shift the centroid forward by 7%. The complexity of the PMT system suggests that method PARTICLE and SIMPLE are ignoring most of the background while method PHOTO treats the background as a more appreciable contribution to the spectrum.

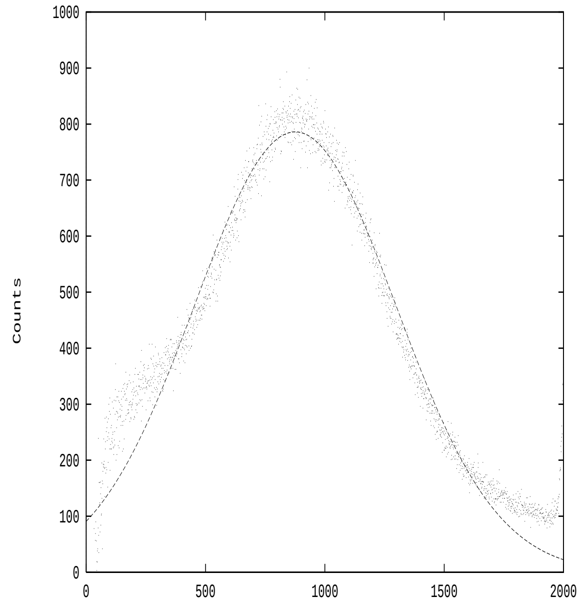

Figure A.5: Photocurrent spectrum of Figure A.4a with background subtracted and fit to a Gaussian (method PARTICLE) having a centroid of 875.89 and a standard deviation 596.24.

As a result of the above analysis, method PHOTO was used to determine the centroid of the single photoelectron signal. The spectrum is broken up into three regions using four gates. The gates appear as vertical lines along the channel number axis of the spectrum. The region within gates #1 and #2 along with the region between gates #3 and #4 are used to fit a third order polynomial representing the background in the system. This function is then used to subtract the counts occurring between gates #2 and #3. Method SIMPLE is also use on the counts within gates #2 and #3. Statistics and the placement of the region in which the third order polynomial is fit to the background are two measurable sources of error. This error is estimated by averaging the two extremes of setting gate #3 symmetrically with respect to gate #2 (short tailed distribution) and setting gate #3 away from the peak giving the distribution a long tail. Typical results of theses measurements are shown in Figure A.7.

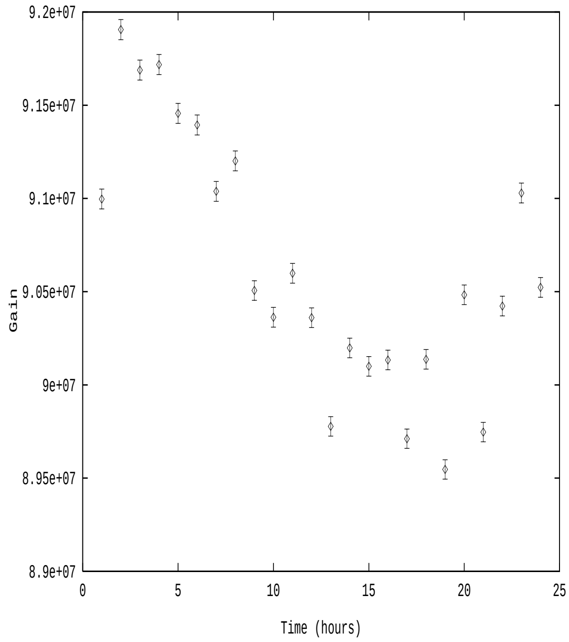

Figure A.6: Multiple photoelectron centroid of PMT # 7312 at a base high voltage of -1500 volts.

A.2.4 Multiple Photoelectron Measurements

Method SIMPLE is used to measure the centroid of the multiple photoelectron spectrum (C_{me}). Using the apparatus described in section A.2.1 and equation A.1, the

PMT gain for multiple photoelectrons ($Gain(me)$) is given by

$$Gain\ (me) = \frac{C_{me} \times (ADC charge\ sensitivity)}{N_{pe} \times (electron\ charge)} = \frac{\sigma_{me}^2 \times 10^8}{64\ C_{me}[1 + (\frac{\sigma_{se}}{C_{se}})^2]}. \tag{A.3}$$

Two problems arose during the gain measurements involving multiple photons. First, the multiple photoelectron signal was found to drift. Figure A.6 is a typical example in which the centroid drifts by 2% when measured for one hour intervals over an extended period of 24 hours. Second, the distribution of a high number of multiple photoelectron events at the cathode has a statistical width which is on the order of the pedestal width until the gain is on the order of 10^6. Therefore, the signal width resulting from the subtraction of the pedestal Gaussian distribution from the signal Gaussian distribution needs to be done using sum of squares error propagation. Although the single electron ratio $\frac{\sigma_{se}}{C_{se}}$ remained constant to within less than 1% over a 300 volt range, a difference of at least 13% was observed between the gain measured during multiple and single photoelectron emission at 1500 Volts (see Figure A.7).

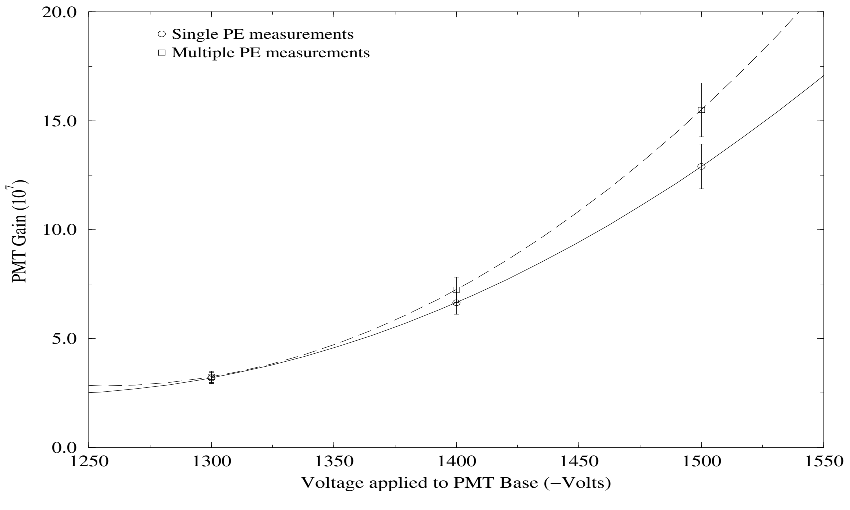

Figure A.7: Gain of PMT #7334 in a region in which the single(circles) and multiple(squares) electron measurements overlap.

The statistical relationship of Equation A.1 was tested experimentally by measuring single and multiple photoelectron signals, solving Equation A.1 for N_{pe} and comparing with the obvious relationship ($N_{pe} = \frac{C_{me}}{C_{se}}$). Limitations on the equation validity and the sensitivity of the PMT to light pulser fluctuations were observed. A deviation of 2% was found in the above relationship when the gain (PMT high Voltage) was changed and the light pulser intensity (N_{pe}) held constant. However, when the gain is constant and the light pulser intensity changed, an 8% deviation was observed between the single an multiple photoelectron signals(see Figure A.8). Measurements were also done at higher light pulser intensities however the high PMT output prevented using the same ADC. The statistical equation A.3 was used to compare the measured gain to the number of photoelectrons (N_{pe}). Figure A.8b shows gain fluctuations of more than 10% when the high voltage on the PMT base is fixed and the light pulser intensity (N_{pe}) is changed.

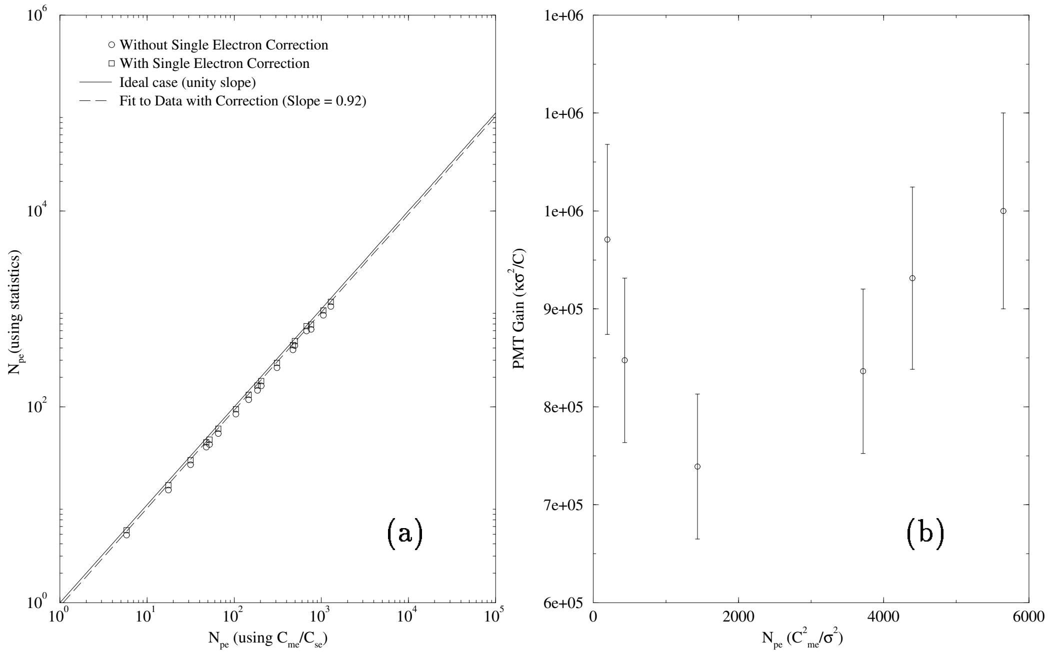

Figure A.8: N_{pe} formula analysis. The solid line is used to represent the ideal case in which the statistical formula is identical with the measured results. The squares denote the use of the entire statistical formula and the circles are used for the statistical formula without the single electron ratio correction term.

A.3 Gain Measurements at MIT Bates

A.3.1 Experimental Setup

The most recent measurements of the PMT gain were performed at MIT Bates with the PMTs mounted in the SAMPLE apparatus (see Figure 3.12). A system of light emitting diodes (LEDs) is mounted symmetrically around the scattering chamber (see Figure 3.12). The LEDs are connected in parallel and oriented to illuminate each PMT at similar light levels. A gate generator triggers the LED such that the PMT face is illuminated for a duration of 15 μsec. The gain of each PMT is then measured using the integration mode electronics and data acquisition (see Figure 3.15).

A.3.2 Analysis

The high noise environment at the MIT Bates accelerator facility needs to be accounted for in a measurement of the PMT gain. Equation A.1 is rewritten in terms of the measured multiple electron error squared (σ_{me}^2).

$$
\begin{aligned}
\sigma_{me}^2 &= \frac{C_{me}^2}{N_{pe}}[1 + (\frac{\sigma_{se}}{C_{se}})^2] \\
&= \frac{G^2 < N_{pe} >^2}{N_{pe}}[1 + (\frac{\sigma_{se}}{C_{se}})^2] \\
&= G^2 C_{me} N_{pe}[1 + (\frac{\sigma_{se}}{C_{se}})^2]
\end{aligned}
$$

The electronic noise in the measurement (σ_{elect}) is added in quadrature with the error from the multiple electron measurement.

$$
\begin{aligned}
\sigma_{tot}^2 &= \sigma_{me}^2 + \sigma_{elect}^2 \\
&= G^2 C_{me} N_{pe}[1 + (\frac{\sigma_{se}}{C_{se}})^2] + \sigma_{elect}^2 [76] \qquad \text{(A.4)}
\end{aligned}
$$

Equation A.4 is linear in σ_{tot}^2 and the PMT gain (G). The LED intensity is changed to map out this linear relationship for each high voltage setting.

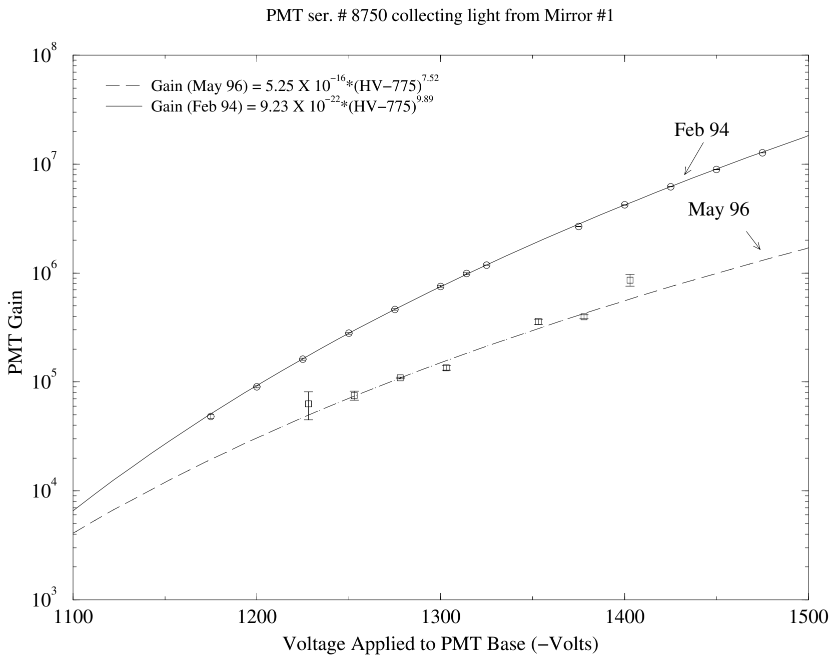

Figure A.9: Gain measurements of Mir1

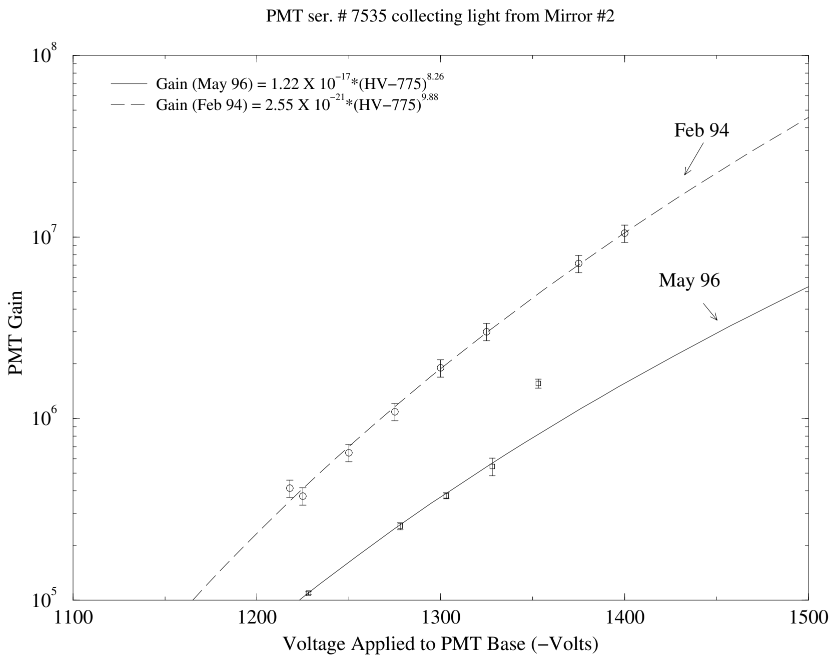

Figure A.10: Gain measurements of Mir2

A.4 Conclusion

The gain of several PMTs for use in the experiment SAMPLE has been measured over a selected voltage range. The phototubes are capable of collecting incident photon rates of 10^6 photons per second until the voltage divider network is driven beyond 1500 volts (corresponding to typical gains of 10^7). Table A.4 is a summary of the high voltage settings used in the SAMPLE experiment and corresponding average gain. Gain measurements taken in February 1994 and May 1996 at MIT Bates are shown for each detector in Figures A.9 - A.18. The statistical method shown in equation A.1 was used for the large data set taken in February 1994 while the statistical method in equation A.4 was used for the limited data set taken in May of 1996. The systematic error from either method is at least 8%. The gain is observed to drift by typically 2% over a 24 hour period.

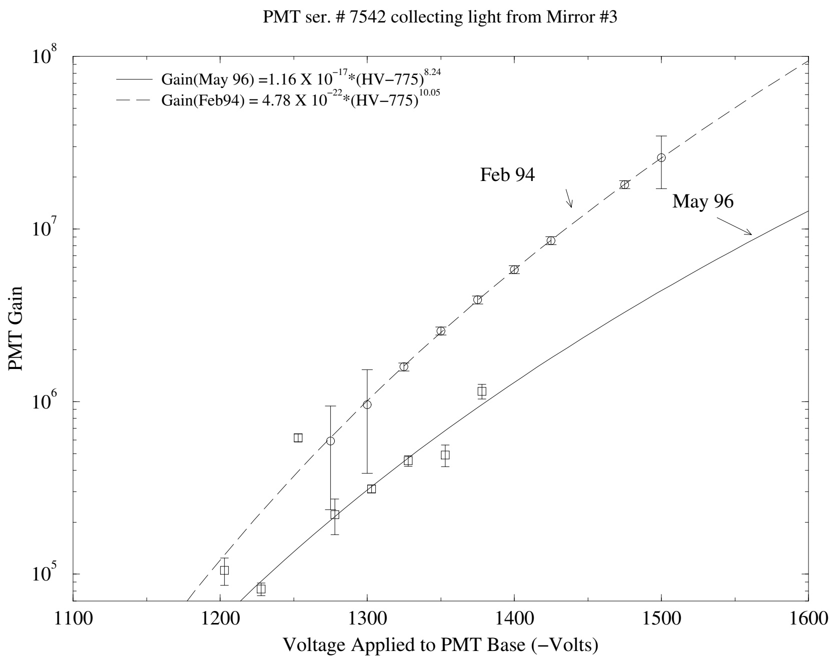

Figure A.11: Gain measurements of Mir3

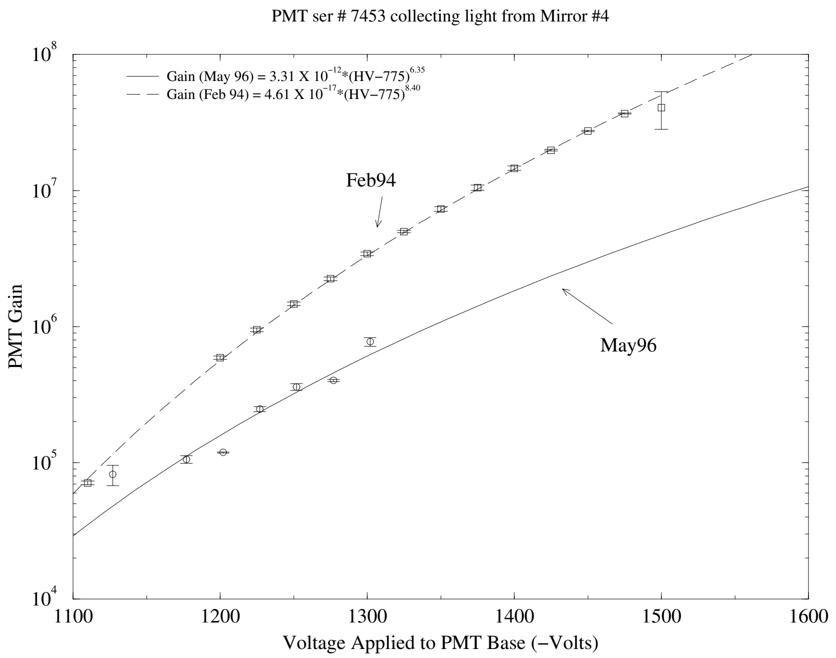

Figure A.12: Gain measurements of Mir4

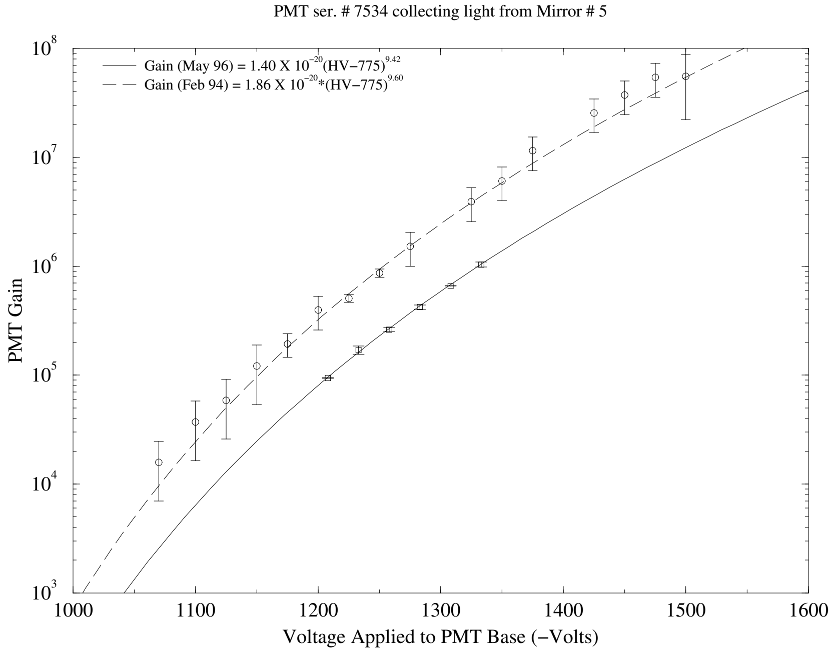

Figure A.13: Gain measurements of Mir5

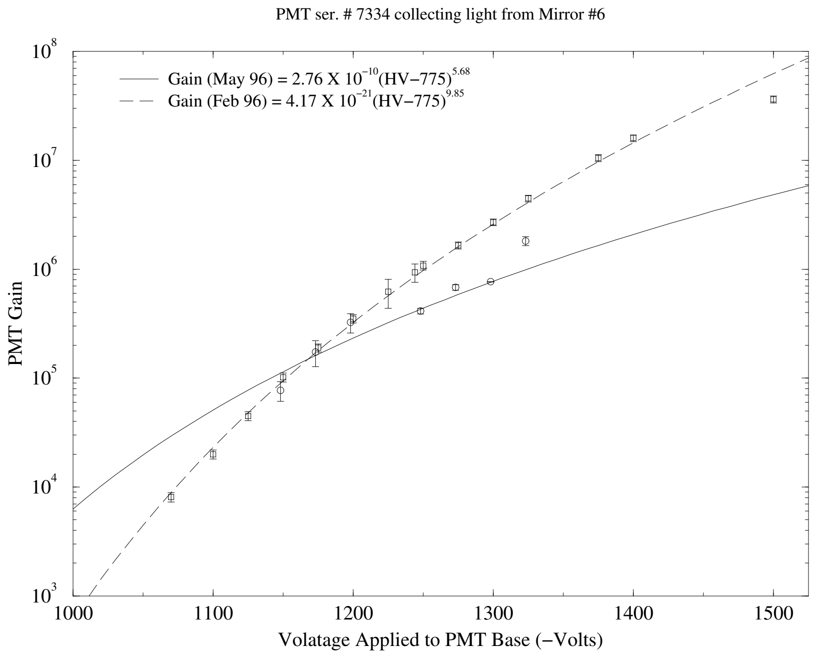

Figure A.14: Gain measurements of Mir6

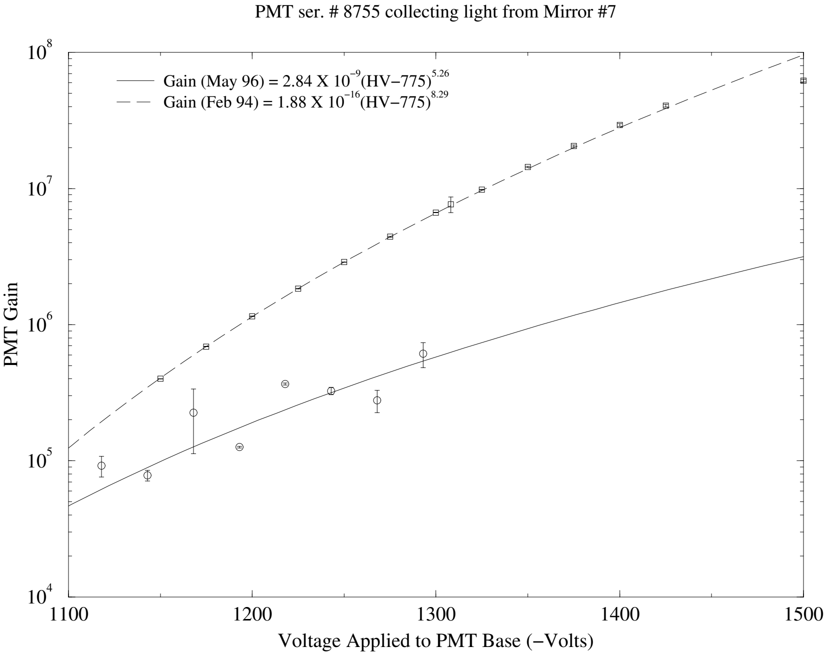

Figure A.15: Gain measurements of Mir7

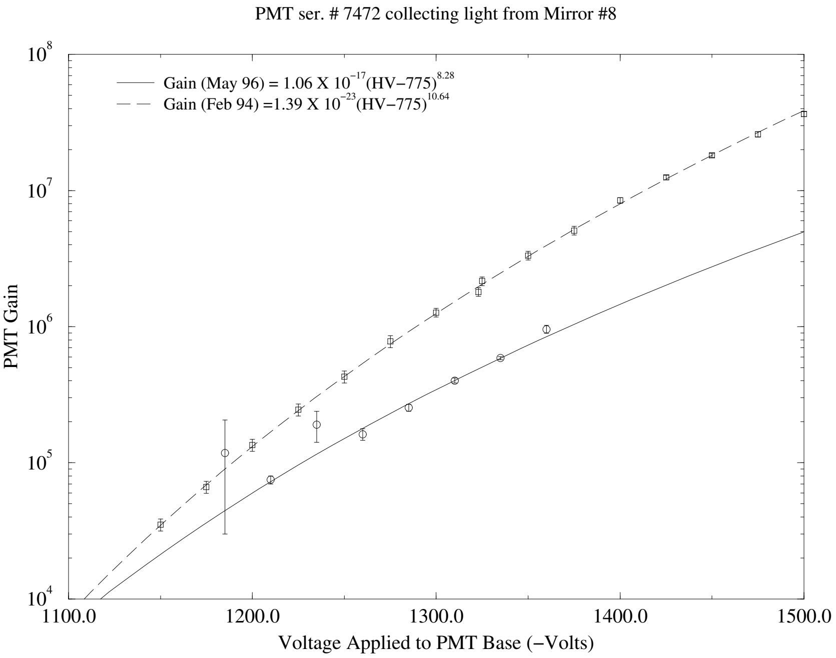

Figure A.16: Gain measurements of Mir8

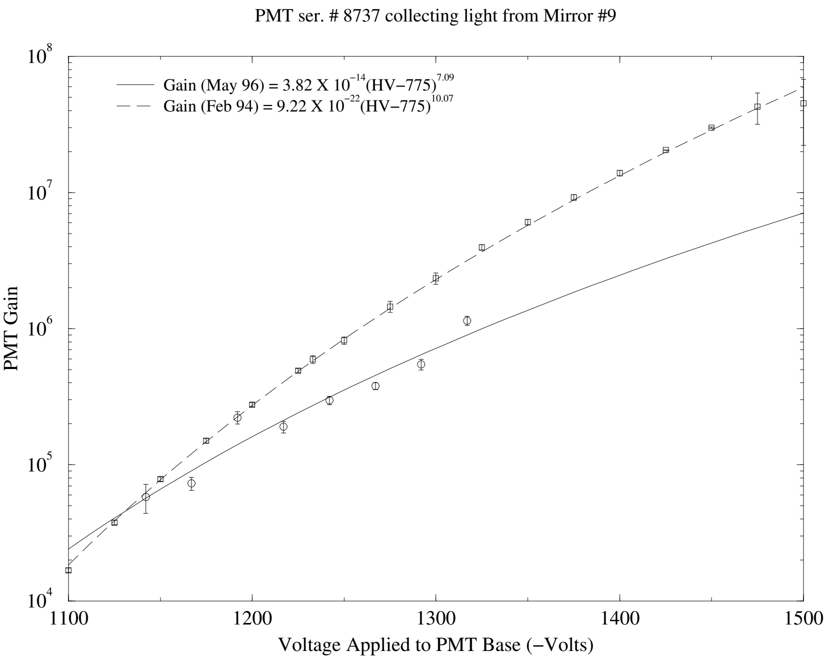

Figure A.17: Gain measurements of Mir9

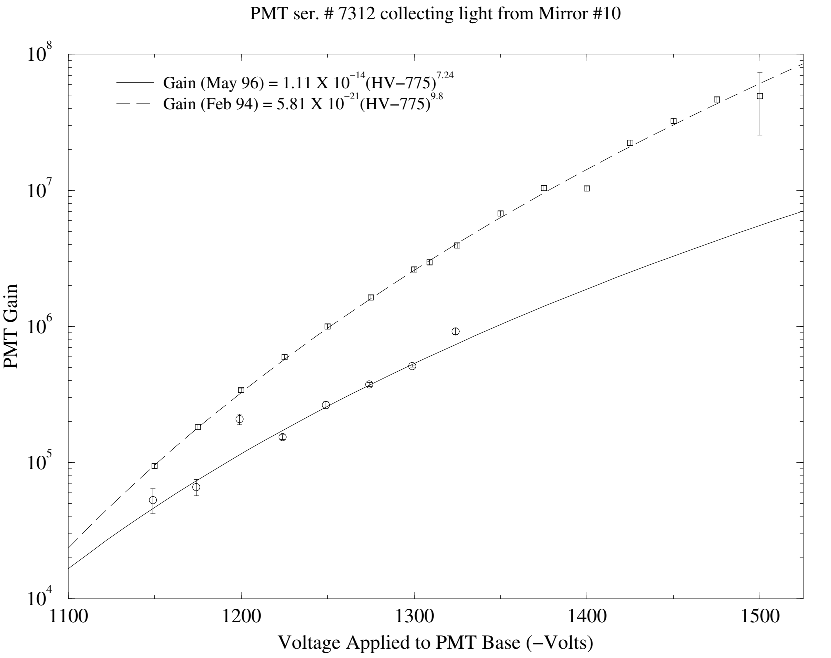

Figure A.18: Gain measurements of Mir10

Detector #	Tube Serial #	Base #	Voltage (-Volts) $\pm$ 10	Gain (10^5)
1	8750	4A	1328	7.39 ± 5.17
2	7535	4I	1278	2.83 ± 0.92
3	7542	4M	1303	6.99 ± 3.89
4	7636	4L	1227	4.30 ± 1.90
5	7534	4H	1258	6.33 ± 4.69
6	7334	4N	1248	6.90 ± 3.42
7	8755	4F	1218	5.93 ± 2.54
8	7472	4E	1285	5.97 ± 4.50
9	8737	4K	1242	6.21 ± 1.84
10	7312	4G	1249	6.38 ± 0.77

Table A.4: Base type #4 voltage settings used during the SAMPLE experiment.

Appendix B

Error Propagation

B.1 The Data Set

The propagation of errors in an asymmetry measurement is done at several levels. The data is accumulated at a rate of 600 events/sec where a pedestal (beam off) event is taken after every 29 data events. The average of 10 pedestal events is subtracted from each of the 29 data events. The data is normalized using the average of the last two toroids in the beam line before the target. The symbol S_i represents the Čerenkov signal measured by the detectors for the ith data event and P represents the pedestal (beam off) measurement. The incident electron current measured by a toroid is denoted by the symbol T_i and the toroid pedestal is denoted as W.

B.2 Error In an Independent Yield Measurement

The following is the error propagation in the calculation of the normalized yield (N_i) for 29 samples using the same pedestal event.

Let

$$N_i \equiv \frac{S_i - P}{T_i - W} = f(S_i, P, T_i, W)$$

Then

$$\bar{N} = \frac{1}{29}\sum_{i}^{29} N_i$$

$$\delta \bar{N}^2 = \sum_{i,j}^{29} < \delta N_i \delta N_j >$$

Using a first order taylor expansion $\delta N_i = \frac{\partial N_i}{\partial S_i}\delta S_i + \frac{\partial N_i}{\partial P}\delta P + \frac{\partial N_i}{\partial T_i}\delta T_i + \frac{\partial N_i}{\partial W}\delta W$ and doing the derivatives: $\frac{\partial N_i}{\partial S_i} = \frac{1}{T_i - W} = \frac{-\partial N_i}{\partial P}$ & $\frac{\partial N_i}{\partial T_i} = \frac{-(S_i - P)}{(T_i - W)^2} = \frac{-\partial N_i}{\partial W}$ results in the following expression:

$$\delta \bar{N}^2 = \sum_i^{29} < \delta N_i^2 > + \sum_{i \neq j}^{29} < \delta N_i \delta N_j >$$

$$\sum_i^{29} < \delta N_i^2 > = \sum_i^{29} \frac{< \delta S_i^2 > + < \delta P^2 >}{(T_i - W)^2} + \frac{(< \delta T_i^2 > + < \delta W^2 >)(S_i - P)^2}{(T_i - W)^2}$$

$$\sum_{i \neq j}^{29} < \delta N_i \delta N_j > = \sum_{i \neq j}^{29} \frac{< \delta P^2 >}{(T_i - W)(T_j - W)} + \frac{(S_i - P)}{(T_i - W)^2} \frac{(S_j - P)}{(T_j - W)^2} < \delta W^2 >$$

The series may be reduced to the naive expression for the error plus a correction term for the covariance. Assume $T_i = T$ and $S_i = S$ then :
$\frac{\delta \bar{N}^2}{N^2} = 29(\frac{<\delta S^2>+<\delta P^2>}{(S-P)^2} + \frac{(<\delta T^2>+<\delta W^2>)}{(T-W)^2}) + (28)(29)(\frac{<\delta P^2>}{(S-P)^2} + \frac{<\delta W^2>}{(T-W)^2})$ or

$$\frac{\delta \bar{N}}{\sqrt{29}\bar{N}} = \frac{\delta N}{N} \sqrt{1 + 28 \left(\frac{< \delta P^2 >}{(S - P)^2} + \frac{< \delta W^2 >}{(T - W)^2} \right) \frac{N^2}{\delta N^2}}$$

where

$$\frac{\delta N^2}{N^2} = \frac{< \delta S^2 > + < \delta P^2 >}{(S - P)^2} + \frac{< \delta T^2 > + < \delta W^2 >}{(T - W)^2}$$

B.3 Error In a Single Independent Asymmetry Measurement

The following determines the error in an asymmetry calculation of a single device based on a data set containing 29 measurements.

Let

$$A_i \equiv \frac{N_i - \mathcal{N}_i}{N_i - \mathcal{N}_i} = f(S_i, P, T_i, W, \mathcal{S}_i, \mathcal{P}, \mathcal{T}_i, \mathcal{W})$$

where the Light yield from the original event is defined as $N_i \equiv \frac{S_i - P}{T_i - W}$ and the compliment event is $\mathcal{N}_i \equiv \frac{\mathcal{S}_i - \mathcal{P}}{\mathcal{T}_i - \mathcal{W}}$.

Then

$$\bar{A} = \frac{1}{29}\sum_{i}^{29} A_i$$

$$\delta\bar{A}^2 = \sum_{i}^{29} < \delta A_i^2 > + \sum_{i \neq j}^{29} < \delta A_i \delta A_j >$$

with the usual first order taylor expansion:

$$\begin{aligned} \delta A_i = \; & \tfrac{\partial A_i}{\partial S_i}\delta S_i + \tfrac{\partial A_i}{\partial P}\delta P + \tfrac{\partial A_i}{\partial T_i}\delta T_i + \tfrac{\partial A_i}{\partial W}\delta W + \\ & \tfrac{\partial A_i}{\partial \mathcal{S}_i}\delta \mathcal{S}_i + \tfrac{\partial A_i}{\partial \mathcal{P}}\delta \mathcal{P} + \tfrac{\partial A_i}{\partial \mathcal{T}_i}\delta \mathcal{T}_i + \tfrac{\partial A_i}{\partial \mathcal{W}}\delta \mathcal{W} \end{aligned}$$

The diagonal terms give:

$$\begin{aligned} < \delta A_i^2 >= \; & (\tfrac{\partial A_i}{\partial S_i})^2 < \delta S_i^2 > + (\tfrac{\partial A_i}{\partial P})^2 < \delta P^2 > + (\tfrac{\partial A_i}{\partial T_i})^2 < \delta T_i^2 > + (\tfrac{\partial A_i}{\partial W})^2 < \delta W^2 > + \\ & (\tfrac{\partial A_i}{\partial \mathcal{S}_i})^2 < \delta \mathcal{S}_i^2 > + (\tfrac{\partial A_i}{\partial \mathcal{P}})^2 < \delta \mathcal{P}^2 > + (\tfrac{\partial A_i}{\partial \mathcal{T}_i})^2 < \delta \mathcal{T}_i^2 > + (\tfrac{\partial A_i}{\partial \mathcal{W}})^2 < \delta \mathcal{W}^2 > \end{aligned}$$

with the non-zero off-diagonal (covariance) terms:

$$\begin{aligned} < \delta A_i^2 \delta A_j^2 >= \; & (\tfrac{\partial A_i}{\partial P})(\tfrac{\partial A_j}{\partial P}) < \delta P^2 > + (\tfrac{\partial A_i}{\partial W})(\tfrac{\partial A_j}{\partial W}) < \delta W^2 > \\ & + (\tfrac{\partial A_i}{\partial \mathcal{P}})(\tfrac{\partial A_j}{\partial \mathcal{P}}) < \delta \mathcal{P}^2 > + (\tfrac{\partial A_i}{\partial \mathcal{W}})(\tfrac{\partial A_j}{\partial \mathcal{W}}) < \delta \mathcal{W}^2 > \end{aligned}$$

Doing the Partial derivatives:

$$\frac{\partial A_i}{\partial S_i} = \frac{2(\mathcal{S}_i - \mathcal{P})}{(T_i - W)(\mathcal{T}_i - \mathcal{W})(\frac{S_i - P}{T_i - W} + \frac{\mathcal{S}_i - \mathcal{P}}{\mathcal{T}_i - \mathcal{W}})^2} = -\frac{\partial A_i}{\partial P} \tag{B.1}$$

$$\frac{\partial A_i}{\partial T_i} = \frac{-2(S_i - P)(\mathcal{S}_i - \mathcal{P})}{(T_i - W)^2(\mathcal{T}_i - \mathcal{W})(\frac{S_i - P}{T_i - W} + \frac{\mathcal{S}_i - \mathcal{P}}{\mathcal{T}_i - \mathcal{W}})^2} = -\frac{\partial A_i}{\partial W} \tag{B.2}$$

$$\frac{\partial A_i}{\partial \mathcal{S}_i} = \frac{2(S_i - P)}{(T_i - W)(\mathcal{T}_i - \mathcal{W})(\frac{S_i - P}{T_i - W} + \frac{\mathcal{S}_i - \mathcal{P}}{\mathcal{T}_i - \mathcal{W}})^2} = -\frac{\partial A_i}{\partial \mathcal{P}} \tag{B.3}$$

$$\frac{\partial A_i}{\partial \mathcal{T}_i} = \frac{2(S_i - P)(\mathcal{S}_i - \mathcal{P})}{(T_i - W)(\mathcal{T}_i - \mathcal{W})^2(\frac{S_i - P}{T_i - W} + \frac{\mathcal{S}_i - \mathcal{P}}{\mathcal{T}_i - \mathcal{W}})^2} = -\frac{\partial A_i}{\partial \mathcal{W}} \tag{B.4}$$

The variance becomes:

$$
\begin{aligned}
<\delta A_i^2> \; = \; & [(\mathcal{S}_i-\mathcal{P})^2\{(\delta S_i^2+\delta P^2)+(\frac{S_i-P}{T_i-W})^2(\delta T_i^2+\delta W^2)\}+ \\
& (S_i-P)^2\{(\delta\mathcal{S}_i^2+\delta\mathcal{P}^2)+(\frac{\mathcal{S}_i-\mathcal{P}}{\mathcal{T}_i-\mathcal{W}})^2(\delta\mathcal{T}_i^2+\delta\mathcal{W}^2)\}] \\
& \frac{4}{(T_i-W)^2(\mathcal{T}_i-\mathcal{W})^2(\frac{S_i-P}{T_i-W}+\frac{\mathcal{S}_i-\mathcal{P}}{\mathcal{T}_i-\mathcal{W}})^4}
\end{aligned}
\tag{B.5}
$$

with the covariance

$$
\begin{aligned}
<\delta A_i\delta A_j> \; = \; & [(\mathcal{S}_i-\mathcal{P})(\mathcal{S}_j-\mathcal{P})(\delta P^2)+(S_i-P)(S_j-P)(\delta\mathcal{P}^2)+ \\
& (\mathcal{S}_i-\mathcal{P})(\mathcal{S}_j-\mathcal{P})(S_i-P)(S_j-P)(\frac{\delta W}{(T_i-W)(T_j-W)}+ \\
& \frac{\delta\mathcal{W}}{(\mathcal{T}_i-\mathcal{W})(\mathcal{T}_j-\mathcal{W})})] \\
& \frac{4}{(T_i-W)(\mathcal{T}_i-\mathcal{W})(T_j-W)(\mathcal{T}_j-\mathcal{W})(\frac{S_i-P}{T_i-W}+\frac{\mathcal{S}_i-\mathcal{P}}{\mathcal{T}_i-\mathcal{W}})^2(\frac{S_j-P}{T_j-W}+\frac{\mathcal{S}_j-\mathcal{P}}{\mathcal{T}_j-\mathcal{W}})^2}
\end{aligned}
\tag{B.6}
$$

Equation B.5 represents the usual variance of the measured asymmetry while equation B.6 is an attribute of the pedestal subtraction scheme.

B.4 Error In an Averaged Independent Asymmetry Measurement

The error propagation in this calculation has two stages. First determine the average and standard deviation in the asymmetry of 10 mirrors for a single event. Then average this result over the 29 events which share the same pedestal to achieve a single independent value of the average asymmetry from 10 mirrors.

Let

$$\bar{A}_{tot}(i) \equiv \frac{1}{10}\sum_{k=1}^{10} A_{mir}(k)$$

Then

$$<\delta\bar{A}_{tot}^2(i)> = \sum_{k,m}^{10} <\delta A_{mir}(k)\delta A_{mir}(m)> \tag{B.7}$$

The taylor expansion and required partial derivatives are similar to the those of the previous section only requiring a minor renaming of variables for the purpose of clarification. Since all 10 mirrors use the same toroid $(T_i, \mathcal{T}_i)$ and toroid pedestal $(W, \mathcal{W})$, the (k) subscript was omitted.

$$\begin{aligned}
\delta A_{mir}(k) = {} & \tfrac{\partial A_{mir}(k)}{\partial S_{ik}} \delta S_{ik} + \tfrac{\partial A_{mir}(k)}{\partial P_k} \delta P_k + \tfrac{\partial A_{mir}(k)}{\partial T_i} \delta T_i + \tfrac{\partial A_{mir}(k)}{\partial W} \delta W + \\
& \tfrac{\partial A_{mir}(k)}{\partial \mathcal{S}_{ik}} \delta \mathcal{S}_{ik} + \tfrac{\partial A_{mir}(k)}{\partial \mathcal{P}_k} \delta \mathcal{P}_k + \tfrac{\partial A_{mir}(k)}{\partial \mathcal{T}_i} \delta \mathcal{T}_i + \tfrac{\partial A_{mir}(k)}{\partial \mathcal{W}} \delta \mathcal{W}
\end{aligned}$$

The variables without the k subscript emphasize the place where covariance enters the error propagation.

The variance of this average is:

$$\begin{aligned}
< \delta A^2_{mir}(k) > \quad = \quad & [(\mathcal{S}_{ik} - \mathcal{P}_k)^2 \{(\delta S^2_{ik} + \delta P^2_k) + (\frac{S_{ik} - P_k}{T_i - W})^2 (\delta T_i^2 + \delta W^2)\} + \\
& (S_{ik} - P_k)^2 \{(\delta \mathcal{S}^2_{ik} + \delta \mathcal{P}^2_k) + (\frac{\mathcal{S}_{ik} - \mathcal{P}_k}{\mathcal{T}_i - \mathcal{W}})^2 (\delta \mathcal{T}_i^2 + \delta \mathcal{W}^2)\}] \quad \text{(B.8)} \\
& \frac{4}{(T_i - W)^2 (\mathcal{T}_i - \mathcal{W})^2 (\frac{S_{ik} - P_k}{T_i - W} + \frac{\mathcal{S}_{ik} - \mathcal{P}_k}{\mathcal{T}_i - \mathcal{W}})^4}
\end{aligned}$$

with a covariance of

$$\begin{aligned}
< \delta A_{mir}(k) \delta A_{mir}(m) >= \quad & (\tfrac{\partial A_{mir}(k)}{\partial T_i})(\tfrac{\partial A_{mir}(m)}{\partial T_i}) < \delta T_i^2 > + (\tfrac{\partial A_{mir}(k)}{\partial W})(\tfrac{\partial A_{mir}(m)}{\partial W}) < \delta W^2 > \\
& + (\tfrac{\partial A_{mir}(k)}{\partial \mathcal{T}_i})(\tfrac{\partial A_{mir}(m)}{\partial \mathcal{T}_i}) < \delta \mathcal{T}_i^2 > + (\tfrac{\partial A_{mir}(k)}{\partial \mathcal{W}})(\tfrac{\partial A_{mir}(m)}{\partial \mathcal{W}}) < \delta \mathcal{W}^2 > \\
= \quad & \tfrac{4}{(T_i - W)^2 (\mathcal{T}_i - \mathcal{W})^2} \tfrac{(\mathcal{S}_{ik} - \mathcal{P}_k)(S_{ik} - P_k)}{\left(\frac{S_{ik} - P_k}{T_i - W} + \frac{\mathcal{S}_{ik} - \mathcal{P}_k}{\mathcal{T}_i - \mathcal{W}}\right)^2} \tfrac{(\mathcal{S}_{im} - \mathcal{P}_m)(S_{im} - P_m)}{\left(\frac{S_{im} - P_m}{T_i - W} + \frac{\mathcal{S}_{im} - \mathcal{P}_m}{\mathcal{T}_i - \mathcal{W}}\right)^2} \\
& (\tfrac{\delta T_i^2 + \delta W^2}{(T_i - W)^2} + \tfrac{\delta \mathcal{T}_i^2 + \delta \mathcal{W}^2}{(\mathcal{T}_i - \mathcal{W})^2})
\end{aligned} \quad \text{(B.9)}$$

To form the average asymmetry for a completely independent measurement with 29 samples of 10 mirrors, define the following average:

Let

$$\bar{A}_{tot} \equiv \frac{1}{29} \sum_{i=1}^{29} \bar{A}_{tot}(i)$$

Then

$$< \delta \bar{A}_{tot}^2 >= \sum_{i=1}^{29} < \delta \bar{A}_{tot}^2 > + \sum_{i \neq j}^{29} < \delta \bar{A}_{tot}(i) \delta \bar{A}_{tot}(j) >$$

with the variance given by equation B.7 and the covariance term

$$\begin{aligned} < \delta \bar{A}_{tot}(i) \delta \bar{A}_{tot}(j) > &= (\frac{\partial \bar{A}_{tot}(i)}{\partial P_k})(\frac{\partial \bar{A}_{tot}(j)}{\partial P_k}) < \delta P_k^2 > \\ &+ (\frac{\partial \bar{A}_{tot}(i)}{\partial W})(\frac{\partial \bar{A}_{tot}(j)}{\partial W}) < \delta W^2 > \\ &+ (\frac{\partial \bar{A}_{tot}(i)}{\partial \mathcal{P}_k})(\frac{\partial \bar{A}_{tot}(j)}{\partial \mathcal{P}_k}) < \delta \mathcal{P}_k^2 > \\ &+ (\frac{\partial \bar{A}_{tot}(i)}{\partial \mathcal{W}})(\frac{\partial \bar{A}_{tot}(j)}{\partial \mathcal{W}}) < \delta \mathcal{W}^2 > \end{aligned} \tag{B.10}$$

Substituting the A_{mir} series in for $\bar{A}_{tot}$ and breaking the equation into a Mirror pedestal sum and a Toroid pedestal sum:

$$\begin{aligned} < \delta \bar{A}_{tot}(i) \delta \bar{A}_{tot}(j) >_p &= \sum_{k=1}^{10} ((\mathcal{S}_{i,k} - \mathcal{P}_k)(\mathcal{S}_{j,k} - \mathcal{P}_k) < \delta P_k^2 > + \\ &\quad (S_{i,k} - P_k)(S_{j,k} - P_k) < \delta \mathcal{P}_k^2 >) \\ &\quad \frac{2}{(T_i - W)(T_j - W)(\frac{S_{j,k} - P_k}{T_j - W} + \frac{\mathcal{S}_{j,k} - \mathcal{P}_k}{\mathcal{T}_j - \mathcal{W}})^2} \\ &\quad \frac{2}{(\mathcal{T}_i - \mathcal{W})(\mathcal{T}_j - \mathcal{W})(\frac{S_{i,k} - P_k}{T_i - W} + \frac{\mathcal{S}_{i,k} - \mathcal{P}_k}{\mathcal{T}_i - \mathcal{W}})^2} \end{aligned} \tag{B.11}$$

$$\begin{aligned} < \delta \bar{A}_{tot}(i) \delta \bar{A}_{tot}(j) >_w &= \sum_{k,m}^{10} (\mathcal{S}_{i,k} - \mathcal{P}_k)(\mathcal{S}_{j,m} - \mathcal{P}_m)(S_{i,k} - P_k)(S_{j,m} - P_m) \\ &\quad \left(\frac{< \delta W^2 >}{(T_i - W)(T_j - W)} + \frac{< \delta \mathcal{W}^2 >}{(\mathcal{T}_i - \mathcal{W})(\mathcal{T}_j - \mathcal{W})} \right) \\ &\quad \frac{2}{(T_i - W)(T_j - W)(\frac{S_{j,m} - P_m}{T_j - W} + \frac{\mathcal{S}_{j,m} - \mathcal{P}_m}{\mathcal{T}_j - \mathcal{W}})^2} \\ &\quad \frac{2}{(\mathcal{T}_i - \mathcal{W})(\mathcal{T}_j - \mathcal{W})(\frac{S_{i,k} - P_k}{T_i - W} + \frac{\mathcal{S}_{i,k} - \mathcal{P}_k}{\mathcal{T}_i - \mathcal{W}})^2} \end{aligned}$$

Explicitly writing everything out :

$$\bar{A}_{tot} \equiv \frac{1}{290}\sum_{i=1}^{29}\sum_{k}^{10}\frac{\frac{S_{ik}-P_k}{T_i-W}-\frac{\mathcal{S}_{ik}-\mathcal{P}_k}{\mathcal{T}_i-\mathcal{W}}}{\frac{S_{ik}-P_k}{T_i-W}+\frac{\mathcal{S}_{ik}-\mathcal{P}_k}{\mathcal{T}_i-\mathcal{W}}}$$

Then

$$\begin{aligned} < \delta\bar{A}_{tot}^2 > &= \sum_{i=1}^{29}\left(\sum_{k=1}^{10} < \delta A_{mir}^2(k) > + \sum_{k\neq m}^{10} < \delta A_{mir}(k)\delta A_{mir}(m) > \right) \\ &+ \sum_{i\neq j}^{29} < \delta\bar{A}_{tot}(i)\delta\bar{A}_{tot}(j) > \end{aligned}$$

Making the same reduction in the series that: S_{ij}=S $\mathcal{S}_{ij}$=$\mathcal{S}$ T_i=T $\mathcal{T}_i$=$\mathcal{T}$ P_k=P $\mathcal{P}_k$=$\mathcal{P}$

$$\begin{aligned} \frac{< \delta\bar{A}_{tot}^2 >}{290} = \frac{4(S-P)^2(\mathcal{S}-\mathcal{P})^2}{(T-W)^2(\mathcal{T}-\mathcal{W})^2\left(\frac{S-P}{T-W}+\frac{\mathcal{S}-\mathcal{P}}{\mathcal{T}-\mathcal{W}}\right)^4} \\ (\frac{< \delta S^2 > + < \delta P^2 >}{(S-P)^2} + \frac{< \delta\mathcal{S}^2 > + < \delta\mathcal{P}^2 >}{(\mathcal{S}-\mathcal{P})^2} + \\ \frac{< \delta T^2 > + < \delta W^2 >}{(T-W)^2} + \frac{< \delta\mathcal{T}^2 > + < \delta\mathcal{W}^2 >}{(\mathcal{T}-\mathcal{W})^2} + \\ \frac{9\delta T^2 + (9+28\times 10)\delta W^2}{(T-W)^2} + \frac{9\delta\mathcal{T}^2 + (9+28\times 10)\delta\mathcal{W}^2}{(\mathcal{T}-\mathcal{W})^2} + \\ \frac{28\delta P^2}{(S-P)^2} + \frac{28\delta\mathcal{P}^2}{(\mathcal{S}-\mathcal{P})^2}) \end{aligned} \tag{B.12}$$

or

$$\begin{aligned} \frac{< \delta\bar{A}_{tot}^2 >}{290} = \frac{4(S-P)^2(\mathcal{S}-\mathcal{P})^2}{(T-W)^2(\mathcal{T}-\mathcal{W})^2\left(\frac{S-P}{T-W}+\frac{\mathcal{S}-\mathcal{P}}{\mathcal{T}-\mathcal{W}}\right)^4} \\ (\frac{< \delta S^2 > +29 < \delta P^2 >}{(S-P)^2} + \frac{< \delta\mathcal{S}^2 > +29 < \delta\mathcal{P}^2 >}{(\mathcal{S}-\mathcal{P})^2} + \\ \frac{10 < \delta T^2 > +290 < \delta W^2 >}{(T-W)^2} + \frac{10 < \delta\mathcal{T}^2 > +290 < \delta\mathcal{W}^2 >}{(\mathcal{T}-\mathcal{W})^2}) \end{aligned} \tag{B.13}$$

In the further limit that $A = P = W = 0$ and $\delta N = \delta\mathcal{N}$:

$$\frac{< \delta\bar{A}_{tot} >}{\sqrt{290}} = \frac{\delta N}{\sqrt{2N}} \tag{B.14}$$

B.5 Contributions to the measured asymmetry from BPM Correction

The detector signal is corrected for changes in the incident electron energy and position. The corrections are done to remove helicity dependence on the incident electron energy and position. The amount of correction is determined by fitting the detector response to the centroid of each of the five beam parameters listed in Table 6.2. This correction introduces a correlation that is analogous to that derived in the previous section.

Let N^h denote the normalized detector signal defined previously as $S^h = \frac{S^h - P^h}{T^h - W^h}$. The corrected asymmetry may be written as

$$A_{cor} = \frac{(N^+ - C^+) - (N^- - C^-)}{(N^+ - C^+) + (N^- - C^-)} \tag{B.15}$$

where C^h is the correction to N^h. The correction C^h represents the term $\sum_{j=1}^{5}\sum_{l=1}^{4}\beta_j^l P_l(X_j)$ in Equation 6.1. The uncertainty squared in C^h is given in Equation 6.7. The uncertainty is increased using the calculated χ^2/ν in the event that the value of χ^2/ν is greater than unity[77].

Using the same error propagation method as in the previous section the uncertainty in A_{cor} would become

$$\begin{aligned}
\delta^2 A_{cor} &= \frac{4(N^+ - C^+)^2(N^- - C^-)^2}{(N^+ + N^- - C^+ - C^-)^4} \\
&\times \frac{\delta^2 N^+ + \delta^2 C^+}{(N^+ - C^+)^2} + \frac{\delta^2 N^- + \delta^2 C^-}{(N^- - C^-)^2} \\
&+ \frac{(N^+ + N^- + C^+ - C^-)(N^+ - C^+ - N^- + C^-)}{(N^+ - C^+)^2(N^- - C^-)^2} \times \\
&\quad (\delta N^+ \delta N^- - \delta N^+ \delta C^- - \delta N^- \delta C^+ + \delta C^+ \delta C^-) \\
&+ \frac{2(N^+ + N^- + C^+ - C^-)}{(N^+ - C^+)(N^- - C^-)} \left[\frac{\delta N^+ \delta C^+}{(N^- - C^-)} + \frac{\delta N^- \delta C^-)}{(N^+ - C^+)}\right]
\end{aligned} \tag{B.16}$$

Vita

Tony Andrew Forest was born in Wembley, England on March 10th 1965 to John and Jean Forest. He received a Bachelor of Science (B.S.) degree in mathematics and physics at the University of Southern Colorado in 1988. He had a brief flirtation with nuclear theory at Western Michigan University which resulted in a physics M.S. degree in 1991. He was a two time recipient of the Jacob P. DeWitt Outstanding Teaching Award 1989 -1991 as well as recieving an Outstanding Scholarship Award in 1989. He then travel to the open skies at the University of Illinois to work in experimental nuclear physics.

Publications:

Measurement of the Proton's Neutral Weak Magnetic Form Factor, SAMPLE collaboration, Phys. Rev. Lett. **78**, 3824 (1997).

A High Power Hydrogen Target for Parity Violation Experiments, E. J. Beise, D. H. Beck, E. Candell, R. Carr, F. Duncan, T. Forest, W. Korsch, J. W. Mark, R. D. McKeown, B. A. Mueller, S. Wells , Nucl. Instrum. Meth. **A378**, 383 (1996).

Threshold Eta Photoproduction, A.S.Rosenthal, T.A. Forest, and M. Gonzales, Phys. Rev. C **44**, 2765 (1991).

The Distribtuion of Supernova Remnants in the Large Magellanic Cloud, T.A. Forest, et. al., Publ. Aston. Soc. Pac. **100**, 683 (1988).

Talks Presented:

The Tensor Force Between Quarks in a Nucleon, American Association of Physics Teachers, MI, April 1990.

Supernova Remanants in the LMC, American Association of Physics Teachers, CO, April 1987.